
Theses and Dissertations

Spring 2012

A multi-scale modeling study of the impacts of transported pollutants and local emissions on summertime western US air quality

Min Huang
University of Iowa

Follow this and additional works at: <https://ir.uiowa.edu/etd>



Part of the [Chemical Engineering Commons](#)

Copyright 2012 Min Huang

This dissertation is available at Iowa Research Online: <https://ir.uiowa.edu/etd/2898>

Recommended Citation

Huang, Min. "A multi-scale modeling study of the impacts of transported pollutants and local emissions on summertime western US air quality." PhD (Doctor of Philosophy) thesis, University of Iowa, 2012.
<https://doi.org/10.17077/etd.9dmpc6ma>

Follow this and additional works at: <https://ir.uiowa.edu/etd>



Part of the [Chemical Engineering Commons](#)

A MULTI-SCALE MODELING STUDY OF THE IMPACTS OF TRANSPORTED
POLLUTANTS AND LOCAL EMISSIONS ON SUMMERTIME WESTERN US AIR
QUALITY

by

Min Huang

An Abstract

Of a thesis submitted in partial fulfillment
of the requirements for the Doctor of Philosophy degree
in Chemical and Biochemical Engineering
in the Graduate College of
The University of Iowa

May 2012

Thesis Supervisor: Professor Gregory R. Carmichael

ABSTRACT

The impacts of transported and locally-produced pollutants on western US air quality during summer 2008 are studied using the multi-scale Sulfur Transport and dEposition Modeling system. Transported background (TBG) is an indicator of the influences from extra-regional emissions or the lower stratosphere. The magnitude of TBG is expected to increase as the emissions from international sources grow. This trend is especially important in the context of US air quality standards, which tend to become more stringent to protect human health and ecosystems. Forward sensitivity simulations in which the model boundary conditions and emissions are perturbed show that TBG strongly and extensively affect western US surface ozone (more than half of the total), compared to other contributors to background ozone (North American, NA, biomass burning, BB and biogenic emissions), and the impacts differ among various geographical regions and land types. The stratospheric ozone impacts are weak. The TBG ozone contributes most to western US ozone among all TBG species, and TBG peroxyacetyl nitrate is the most important species among ozone precursors. Compared to monthly mean 8-hour daily maximum ozone, the secondary standard metric “W126 monthly index” shows larger responses to TBG perturbations and stronger non-linearity to the size of perturbations. Overall the model-estimated TBG impacts negatively correlate to the vertical resolution and positively correlate to the horizontal resolution. The estimated TBG impacts weakly depend on the magnitude of uncertainties in the US anthropogenic emissions. The transport/subsidence processes that link airmasses aloft with the surface pollution level are analyzed by trajectories, time-lag correlation and adjoint sensitivity analyses. Various types of observations are used to identify source regions and transport processes, and to improve model prediction using the four-dimensional variational data assimilation during a long-range transport episode.

The sectoral and geographical contributions to summertime US black carbon (BC) distributions are studied. NA emissions heavily (>70%) affect the BC levels from the surface to 5 km, while non-NA plumes compose more than half of the BC above 5 km. NA and non-NA

BB, NA transportation and non-NA residential emissions are the major contributing sectors. Aircraft measurements during the California phase of the Arctic Research of the Composition of the Troposphere from Aircraft and Satellites (ARCTAS-CARB) field campaign show that BC/(organic matter + nitrate + sulfate) mass ratios fairly well represent BC's warming potential over southern California, which can be approximated by BC/(organic matter + sulfate) and BC/sulfate for plumes affected and unaffected by fires, respectively. The responses of BC/(organic matter + sulfate) and BC/sulfate to removing each emission sector indicate that mitigating NA transportation emissions has the highest potential for regional air quality and climate co-benefits. Contributions from NA BB and extra-regional emissions differ for summer and spring (April 2008).

Abstract Approved: _____
 Thesis Supervisor

 Title and Department

 Date

A MULTI-SCALE MODELING STUDY OF THE IMPACTS OF TRANSPORTED
POLLUTANTS AND LOCAL EMISSIONS ON SUMMERTIME WESTERN US AIR
QUALITY

by
Min Huang

A thesis submitted in partial fulfillment
of the requirements for the Doctor of Philosophy degree
in Chemical and Biochemical Engineering
in the Graduate College of
The University of Iowa

May 2012

Thesis Supervisor: Professor Gregory R. Carmichael

Copyright by
MIN HUANG
2012
All Rights Reserved

Graduate College
The University of Iowa
Iowa City, Iowa

CERTIFICATE OF APPROVAL

PH.D. THESIS

This is to certify that the Ph.D. thesis of

Min Huang

has been approved by the Examining Committee
for the thesis requirement for the Doctor of Philosophy
degree in Chemical and Biochemical Engineering at the
May 2012 graduation.

Thesis Committee: _____
Gregory R. Carmichael, Thesis Supervisor

Vicki H. Grassian

Charles O. Stanier

Thomas M. Peters

Julie L. P. Jessop

To My Family

ACKNOWLEDGEMENTS

I would like to thank my graduate advisor Dr. Gregory Carmichael for introducing me the graduate study on atmospheric modeling at University of Iowa, and for his guidance and support on this research. I thank Dr. Charles Stanier, Dr. Thomas Peters, Dr. Vicki Grassian and Dr. Julie Jessop for teaching interesting and informative classes and being helpful thesis committee members. I thank all the faculty members in the department of Chemical and Biochemical Engineering for offering me the opportunity to be part of the graduate program, and Linda Wheatley, Natalie Potter, Jill McNamara, Jane Frank, Jeremie Moen and the Engineering CSS staff for their administrative and technical support.

I would like to thank Dr. Bhupesh Adhikary, Dr. Scott Spak, Dr. Sarika Kulkarni, Dr. Tianfeng Chai, Dr. Youhua Tang, Dr. Chao Wei, and Dr. Yafang Cheng for helping me with STEM and WRF models, analysis tools and paper writing. I appreciate the valuable inputs from many senior scientists in ARCTAS science team, TF HTAP and NASA ACAST working teams, as well as our paper co-authors, editors, and reviewers. They truly helped me understand how the “scientific community” works. I also thank the funding support from University of Iowa, NASA, and EPA.

I would like to thank my parents Shijian Huang and Jianhua Shen for their encouragement and support on my graduate study through the years. Both as engineers, they show me good examples of hard working and critical thinking.

TABLE OF CONTENTS

LIST OF TABLES	vi
LIST OF FIGURES	viii
LIST OF NOMENCLATURE.....	xiii
CHAPTER 1 INTRODUCTION	1
1.1 Background and significance.....	1
1.1.1 Tropospheric ozone and aerosols	1
1.1.2 Western US air quality	3
1.1.3 Integrated modeling-observation study	3
1.1.4 Overall research goal and method	4
1.2 Model and observations.....	4
1.2.1 STEM model	5
1.2.2 Sensitivity analysis and data assimilation	7
1.2.3 Observational products	7
1.3 Specific objectives and thesis outline	7
1.4 Citations to published or presented work	8
CHAPTER 2 IMPACTS OF TRANSPORTED BACKGROUND POLLUTANTS ON SUMMERTIME WESTERN US O ₃ DISTRIBUTIONS	14
2.1 Introduction.....	14
2.2 Data and methods	17
2.2.1 Study period, meteorological conditions and fire activities	17
2.2.2 Observation data	18
2.2.3 STEM model experiments and input data	20
2.2.4 Observation operator and the forcing term.....	27
2.3 Results and discussions.....	29
2.3.1 Forward sensitivity of surface O ₃ to boundary conditions	29
2.3.2 Connecting air mass aloft with surface O ₃	35
2.3.3 Case study: DA during a LRT episode.....	44
2.4 Conclusions and suggestions on future work	49
CHAPTER 3 SECTORAL AND GEOGRAPHICAL CONTRIBUTIONS TO SUMMERTIME CONTINENTAL UNITED STATES (CONUS) BLACK CARBON SPATIAL DISTRIBUTIONS	87
3.1 Introduction.....	87
3.2 Data and methods	88
3.2.1 Study period and observational data.....	88
3.2.2 Model and input data	89
3.2.3 Forward sensitivity analysis	91
3.3 Results and discussions.....	92
3.3.1 Model base case and its evaluation	92
3.3.2 Sector contributions to CONUS BC distributions.....	94
3.3.3 Using metrics to prioritize climate impacts of sector emissions	97
3.3.4 Seasonal variations of extra-regional pollution and NA fires contributions	100
3.4 Conclusions and suggestions on future work	100

CHAPTER 4 SUMMARY AND FUTURE WORK	118
4.1 Summary	118
4.2 Future work	120
REFERENCES	122

LIST OF TABLES

Table 1.1 Environmental, chemical and climate significance of several species, their lifetimes and current national standards	10
Table 1.2 Observations used in this study and purposes	11
Table 2.1 Wildfire plumes characteristics from the MISR plume height project	52
Table 2.2 Descriptions of observational datasets used in this study	56
Table 2.3 Descriptions of STEM full-chemistry base and forward/adjoint sensitivity simulations.....	57
Table 2.4 Descriptions of 4-d var data assimilation cases in the 12 km model grid	58
Table 2.5 Statistics for observed and modeled surface O ₃ metrics at EPA AQS sites as shown in Figure 2.2 (better performance in bold). Model results were extracted at surface by using linear interpolation method.	59
Table 2.6 Same as Table 2.5 but for CASTENT sites, and model results were extracted at identical site altitudes.	59
Table 2.7 US Geological Survey (USGS) land type numbers and method of grouping ...	60
Table 2.8 The "IP" metric for trajectories starting from three locations, at all local daylight times during 16 June-14 July, 2008	61
Table 2.9 Changes of daytime mean surface O ₃ errors between different cases, where error= modeled-observed O ₃	61
Table 3.1 Anthropogenic emissions and several emission ratios by sector	102
Table 3.2 Total anthropogenic (terrestrial+shipping) emissions and emission ratios by regions	103
Table 3.3 Statistical evaluation of modeled summertime BC at surface sites, summarized by EPA regions	104
Table 3.4 Correlation <i>r</i> between emissions and BC concentrations, summarized by EPA regions.....	105
Table 3.5 Correlations between BC/cooling aerosols and SAE along the 24 June DC-8 flight	105
Table 3.6 Aerosol scaling factors by EPA regions	106
Table 3.7 Base case BC/(SO ₄ +OM) ratios and the responses in ratios to removing emission sectors, by EPA regions.	107

Table 3.8 Base case BC/SO ₄ ratios and the responses in ratios to removing emission sectors, by EPA regions. The NA biomass burning and non-NA biomass burning contributions were subtracted from each case before the calculations.....	108
---	-----

LIST OF FIGURES

Figure 1.1 The US O ₃ nonattainment areas based on projected standards and 2006-2008 O ₃ data for eight-hour average (left) and W126 (right) O ₃ metrics (McCarthy et al., 2010).....	12
Figure 1.2 Map of 24-hour PM _{2.5} nonattainment areas (US EPA, 2011, http://www.epa.gov/pmdesignations/2006standards/regs.htm#4)	12
Figure 1.3 The flow chart of this study and model domains	13
Figure 1.4 Flight tracks during the ARCTAS-CARB deployment (Jacob et al., 2010)	13
Figure 2.1 Observed and modeled (RAQMS and STEM 60 km) vertical profiles along the outbound part of the 22 June DC-8 flight, for (a) PAN; (b) NO _y ; (c) CO; and (d) O ₃ ; Comparison between TES and modeled O ₃ mean (e;g) and variability (f;h) from RAQMS (e-f) and STEM 60 km (g-h) over eastern Pacific. TES observational operator was applied. (i) TES special observation sampling density in the compared domain for STEM. Sampling density=number of samples in each 1°×1°/total number of samples.....	62
Figure 2.2 (a-b) Observed MDA8 and W126 monthly index (MI) at EPA AQS (dots) and CASTNET (triangles) sites; Modeled surface MDA8 and W126 MI in (c-d) 60 km/18 layer and (e-f) 12 km/32 layer grids.....	63
Figure 2.3 Period-mean non-NA tracer CO contributions (a) at surface and (b) at ~2.5 km AGL. The calculations were based on ARCTAS anthropogenic and RAQMS fire emissions	64
Figure 2.4 Surface (a) MDA8 and (b) W126 O ₃ responses to perturbations in boundary conditions in the 60 km/18 layer grid, shown by ten EPA regions; (c) Fraction of the grouped USGS land types (bar) and population density (text below the bar) in ten EPA regions; (d) Ten EPA regions; Surface (e) MDA8 and (f) W126 O ₃ responses to perturbations of various species in boundary conditions in the 60 km/18 layer grid, shown by geographical regions (EPA Regions 9 and 10) and grouped USGS land types, respectively (“prec” in legends: the cases in which CO, NO, NO ₂ , NO ₃ , HNO ₃ , HNO ₄ , PAN, N ₂ O ₅ in BCs were perturbed).....	65
Figure 2.5 (a-b) Slope and (d-e) correlation of O ₃ vs. CO at ~2.5 km AGL from (a;d) 12 km and (b;e) 60 km STEM base case for the study period; (c) Scatterplot of O ₃ vs. CO along all ARCTAS-CARB DC-8 flight paths (at ~2-4 km); (f) WRF-chem tracer predicted secondary CO during the same studied period in Pfister et al. (2011b); (g) Observed and (h) STEM 12km modeled PAN/NO _y along all ARCTAS-CARB DC-8 flights at all altitudes; (i) Period mean 00 UTC surface O ₃ sensitivity to half reduction in TBC O ₃	66
Figure 2.6 Surface (a-c) MDA8 and (b-d) W126 O ₃ contributed from (a;d) transported background; (b;e) NA biomass burning emissions; and (c;f) biogenic emissions. To calculate (a) and (d), O ₃ sensitivities to 75% reduction in O ₃	

and precursor BCs were extrapolated to 100% perturbation and summed up.....67

Figure 2.7 The surface O₃ sensitivity ($S1=base\ case-sensitivity\ case$) of (a) W126, (b) MDA8 and (c) ratio of (a)/(b); The surface O₃ relative sensitivity ($S2=(base\ case-sensitivity\ case)/base\ case$) of (d) W126, (e) MDA8 and (f) ratio of (d)/(e). Results are all from the 60 km/18 layer STEM grid. The sensitivity case here refers to 50% reduction in O₃ BC. For subsequent comparison with results from other model grids, the shared areas in EPA Regions 9 and 10 in both 60 km and 12 km domains are shown with the same smoothing method.....68

Figure 2.8 Differences of $S1$ (defined in Figure 2.7 caption) for W126 (a;c;e) and MDA8 (b;d;f) between the cases of (a-b) using the scaled and original US anthropogenic emissions in 60 km/18 layer grid; (c-d) in 60 km/32 layer and 60 km/18 layer grids; and (e-f) in 12 km/32 layer and 60 km/32 layer grids.....69

Figure 2.9 Scatter plots of modeled and observed daily maximum 8-hour average O₃ at all AQS sites, colored by their sensitivities to 50% reduction in BC O₃, in the (a) 12 km/ 32 layer and (b) 60 km/18 layer grids. Regions A and B marked in both panels refer to “erroneously-predicted non-attainment areas” and “the actual non-attainment areas missed by the model”, respectively.70

Figure 2.10 (a) Observed and STEM modeled O₃ time series at the MBO site from 60 km/18 layer and 12 km/32 layer grids. The model results were extracted from the layer(s) that matched the actual MBO altitude; (b) Observed and STEM modeled O₃ time series at SC surface site from the 60 km/18 layer and 12 km/32 layer grids; (c) THD daily ozone sonde data during the studied period, binned into 32 model layers; (d) STEM 12 km modeled THD O₃ daily vertical profiles at ~sounding times during the same period; (e) STEM 60 km modeled THD O₃ daily vertical profiles at 18 UTC during the same period.....71

Figure 2.11 Time series plots of (a) Tracer calculated NO_x age (hours) time series at three locations; Tracer CO contributions (%) to (b) THD 2.5 km; (c) MBO 2.7 km; and (c) SC 1.5 km ASL from various sources.....72

Figure 2.12 Time series of O₃ reductions at (a) MBO 2.7 km ASL; (b) THD 2.5 km ASL; and (c) SC lowest level, in response to 50% perturbations in BC O₃, reduction in US anthropogenic emissions and zeroing out the US biomass burning emissions. Time series of observations at the corresponding altitude are overlaid in red and their period mean are drawn as horizontal thin red lines..... 73

Figure 2.13 PDT 8am-8pm (daytimes) forward trajectories (calculated mean transported altitudes in km, AGL for every 0.25 degree) during the studied period originating from (a) THD 2.5 km ASL and (b) SC1.5 km ASL; (c) PDT 9pm-7am (nighttimes) forward trajectories during the study period originating from MBO 2.7 km ASL; Correlation of daily mean PDT 8 am-8 pm O₃ at (d) THD 2.5 km ASL; (e) SC 1.5 km ASL with ground O₃ one-day later, and with the same day ground O₃, respectively, during the same period; (f) Correlation of daily mean PDT 9

pm-7 am O ₃ at MBO 2.7 km with ground daytime O ₃ on the same day ground O ₃ , during the same period. The correlations are filtered by trajectories.	74
Figure 2.14 Previous daytime mean λ[O ₃] in (a) NWR case and (b) SCR case, all levels integrated; Areas within the blue lines indicate receptor regions; (c) λ[O ₃] time-height curtain at MBO, NWR case; (d) λ[O ₃] time-height curtain at THD, NWR case; (e) λ[O ₃] time-height curtain at SC, SCR case; (f) λ[O ₃] time-height curtain at THD, SCR case. (c-e) were normalized by receptor grid numbers, note the different color scales. Results from 12 km/32 layer grid.....	75
Figure 2.15 Same as Figure 2.14 but for results from 60 km/18 layer grid.....	76
Figure 2.16 (a) 12 km WRF (Version 3.1)-predicted PBLH at 00 UTC, 20 June, by using the MYJ PBL scheme; Differences of WRF (Version 3.1)-predicted PBLH between MYJ case and the cases using (b) YSU; (c) MYNN3; and (d) QNSE PBL schemes; Differences of WRF-predicted PBLH Version 3.1 and the cases using (e) Version 3.2 and (f) Version 3.3.	77
Figure 2.17 (a) MBO and THD back-trajectories ending at 18 UTC on 6 July, colored by travelling heights (AGL, km), based on the 60 km WRF-simulated wind fields. Negative numbers along the trajectories indicate days back from the ending time. RAQMS fire emissions (log (molec./cm ² /s)) at 00 UTC, 1 July are overlaid with grey color scale; TES Level 3 nadir (b) total CO (on 30 June) and (c-d) tropospheric O ₃ (on 2, 4, 6 July) columns; 12 km WRF-simulated ~2.5 km wind fields overlaid with surface level pressure (SLP, hPa) at 18 UTC on (e) 5 July and (f) 6 July....	78
Figure 2.18 (a) DA domain in 12 km/32 layer grid and the locations where the selected (based on criteria described in Table 2.4) TES and OMI measurements were made; (b) Scatter plot of STEM <i>a priori</i> (with OMI observation operator) vs. OMI retrieval, colored by OMI layer center pressure (hPa); (c) STEM <i>a priori</i> (raw data) along the TES orbit, interpolated into the TES pressure levels; (d) STEM <i>a priori</i> (with TES observation operator) along the TES orbit; (e) TES nadir retrieval; (f) The ratios of (e)/(d).....	79
Figure 2.19 Vertical profiles of adjoint λ[O ₃] at selected (a) TES and (c) OMI sampling locations at 22 UTC on 5 July, shown as boxplots (minimum, 1 st Qu., median, 3 rd Qu. and extreme); and (e) at THD site at 19 UTC on July 5. Receptor/final time is NWR/00 UTC on 7 July. Forward trajectories (colored by travelling altitudes) originating at selected (b) TES (~4 km) and (d) OMI (~2 km) sampling locations at 22 UTC on 5 July; and (e) at THD site (2, 3, 4, 5 km) at 19 UTC on 5 July.	80
Figure 2.20 Daytime mean surface O ₃ from (a) STEM <i>a priori</i> ; and (b) <i>Case AS</i> . The site measurements were overlaid (only those sites that had all daytime measurements were shown in the plots); (c) Differences of (b)-(a); (d) Surface and (e) elevated NO _x emission scaling factors by controlling NO _x emissions and assimilating surface NO ₂ observation in a 24-hour window; (f) Cost function and its reduction as a function of iteration number in <i>Case AS</i>	81

Figure 2.21 Daytime mean surface O ₃ differences: (a) <i>Case AT-STEM a priori</i> ; (b) <i>Case AO-STEM a priori</i> ; (c) <i>Case AD-STEM a priori</i> ; (d) <i>Case AD-Case AO</i> ; (e) <i>Case AD- Case AT</i> ; (d) <i>Case AO- Case AT</i>	82
Figure 2.22 Daytime mean surface O ₃ differences: (a) <i>Case AST-Case AS</i> ; (b) <i>Case ASO-Case AS</i> ; (c) <i>Case ASD-Case AS</i> ; (d) <i>Case AST-Case ASO</i> ; (e) <i>Case ASD-Case AST</i> ; (f) <i>Case ASO-Case AST</i>	83
Figure 2.23 O ₃ changes (assimilated fields-the <i>a priori</i>) at selected TES sampling locations for (a-b) <i>Case AS</i> ; (c-d) <i>Case AO</i> ; (e-f) <i>Case AT</i> ; (g-h) <i>Case AD</i> . (a;c;e;g) compare the raw data in TES pressure grids and (b;d;f;h) compare the results after applying the TES observation operator.....	84
Figure 2.24 O ₃ changes (assimilated fields-the <i>a priori</i>) at selected OMI sampling locations for (a) <i>Case AS</i> ; (b) <i>Case AO</i> ; (c) <i>Case AT</i> ; (d) <i>Case AD</i> . In (a-d), black dots compare the raw data in OMI pressure grids and red dots compare the results after applying the OMI observation operator. (e) O ₃ vertical profiles at THD on 5 July from sondes, <i>STEM a priori</i> , <i>Cases AS</i> and <i>AD</i> ; (f) O ₃ changes (assimilated fields-the <i>a priori</i>) at THD for <i>Cases AT</i> and <i>AO</i>	85
Figure 2.25 Comparison between measurements and the assimilated O ₃ in the case the surface observations were assimilated.....	86
Figure 3.1 (a) 24-h average total anthropogenic emissions over tracer hemispheric domain; (b) 24-h average total anthropogenic BC/(SO ₂ +OC) emission mass ratios; (c) 24-h average total anthropogenic BC/OC emission mass ratios; (d) 24-h average total anthropogenic BC/SO ₂ emission mass ratios; (e) Mean total BC emissions from biomass burning; (f) Fire occurrence frequency. The fire occurrence frequency is defined as the number of days that the fire emissions>0/total days in the study period (i.e., 14 days), reported in %.....	109
Figure 3.2 Ratios of two-week (13-26 June) mean (a;c) surface BC and (b;d) column BC responses to 100% and 20% perturbations in (a-b) NA transportation and (c-d) non-NA residential BC emissions, scaled by 5. These two sectors were found to be the major anthropogenic contributors among NA and non-NA sectors, respectively. For most US regions, the responses of BC distributions to emission perturbations are close to linear.....	110
Figure 3.3 Two-week (13-26 June) mean (a) surface BC concentrations (μg/m ³); (b) BC column (mg/m ²); (c) BC vertical distributions (μg/m ³) in ten EPA regions; (d) The ten EPA regions.	111
Figure 3.4 Mean (a) observed and (b) modeled BC (μg/m ³) on 14, 17, 20, 23, 26 June at the IMPROVE sites; Mean (c) observed and (d) modeled BC (μg/m ³) on 14, 17, 20, 23, 26 June at the EPA urban sites; (e) Observed	

and modeled BC ($\mu\text{g}/\text{m}^3$, at standard temperature and pressure) vertical profiles shown as boxplots along 20, 22, 24 June DC-8 flight tracks.....	112
Figure 3.5 Two-week (13-26 June) mean surface BC ($\mu\text{g}/\text{m}^3$) contributed from (a) NA biomass burning; (b) shipping; (c) NA industrial; (d) NA power; (e) NA residential; (f) NA transportation emission sectors.....	113
Figure 3.6 Two-week (13-26 June) mean surface BC ($\mu\text{g}/\text{m}^3$) contributed from (a) all non-NA; (b) non-NA biomass burning; (c) non-NA industrial; (d) non-NA power; (e) non-NA residential; (f) non-NA transportation emission sectors.....	114
Figure 3.7 Stack plots of contributions from eleven sectors to US (a) surface BC ($\mu\text{g}/\text{m}^3$); (b) column BC (mg/m^2); (c) BC vertical profiles ($\mu\text{g}/\text{m}^3$) during 13-26 June, 2008.....	115
Figure 3.8 (a) Temporal correlation r between surface and column BC during 13-26 June, 2008; (b) Comparison between tracer extra-regional CO% and extra-regional BC% calculated by the forward sensitivity simulations for ten EPA regions.	115
Figure 3.9 (a) The 24 June DC-8 flight path (where aerosols, acetonitrile and green band SSA measurements were made), colored by flight altitude (ASL, km), overlaid on MODIS cloud fraction at 18:45 UTC (11:45 am PDT); (b) BC source attribution along the flight, shown every 500 m in boxplots, AN and BB stand for anthropogenic and biomass burning, respectively; (c) Scatter plot of SAE against BC/(OM + SO ₄ + NO ₃), colored by observed BC. Inner panel are pie plots of cooling aerosol compositions along the path in (a) for terrestrial and oceanic samples; (d) Scatter plot of SAE against BC/SO ₄ , colored by observed acetonitrile. (MODIS: Moderate Resolution Imaging Spectroradiometer).....	116
Figure 3.10 Spring (1-20 April, 2008) mean surface BC ($\mu\text{g}/\text{m}^3$) contributed from (a) all non-NA emission sectors and (b) NA biomass burning emissions.....	117

LIST OF NOMENCLATURE

Chemical Formula

CH ₄	methane
CO	carbon monoxide
CO ₂	carbon dioxide
HNO ₃	nitric acid
HNO ₄	peroxynitric acid
H ₂ O ₂	hydrogen peroxide
NO	nitric oxide
NO _x	sum of nitric oxide and nitrogen dioxide
NO _y	nitrogen oxides
NO ₂	nitrogen dioxide
NO ₃	nitrate
N ₂ O ₅	dinitrogen pentoxide
OC	organic carbon
OM	organic matter
O ₃	ozone
PAN	peroxyacetyl nitrate
SO _x	sulfur oxides
SO ₂	sulfur dioxide
SO ₄	sulfate
VOCs	volatile organic compounds

Abbreviations

4-d var	Four-dimensional Variational data assimilation
---------	---

AGL	Above Ground Level
ARC-IONS 2008	Arctic Intensive Ozonesonde Network Study 2008
AMS	Aerosol Mass Spectrometry
AN	Anthropogenic
AQS	Air Quality System
ARCTAS	Arctic Research of the Composition of the Troposphere from Aircraft and Satellites
ASL	Above Sea Level
BB	Biomass Burning
BC (Chapter 2)	Boundary Conditions
BC (Chapter 3)	Black Carbon
CA	California
CARB	California Air Resource Board
CASTNET	Clean Air Status and Trends Network
CEOS	Committee on Earth Observation Satellites
CIMS	Chemical Ionization Mass Spectrometer
COUNS	Continental United States
CSN	Chemical Speciation Network
DA	Data Assimilation
DRF	Direct Radiative Forcing
DU	Dobson Unit
EC	Elemental Carbon
EPA	Environmental Protection Agency
FINN	Fire INventory from NCAR
GB	Green Band

GEO-CAPE	Geostationary Coastal and Air Pollution Events
HTAP	Hemispheric Transport of Air Pollution
ID	Idaho
IMPROVE	Interagency Monitoring of Protected Visual Environments
INTEX-B	Intercontinental Chemical Transport Experiment-B
IP	Impacting Probability
IPCC AR5	Intergovernmental Panel for Climate Change 5 th Assessment
LARGE	Langley Aerosol Research Group
LBC	Lateral Boundary Conditions
LIDAR	Light Detection And Ranging
LRT	Long Range Transport
LT	Local Time
L-BFGS	Limited memory-Broyden-Fletcher-Goldfarb-Shanno
MBO	Mountain Bachelor Observatory
MDA8	Monthly mean Daily maximum 8-hour Average ozone
MFB	Mean Fractional Bias
MFE	Mean Fractional Error
MISR	Multi-angle Imaging SpectroRadiometer
MODIS	Moderate Resolution Imaging Spectroradiometer
NA	North America(n)

NASA	National Aeronautics and Space Administration
NCAR	National Center for Atmospheric Research
NEI	National Emission Inventory
NIOSH	National Institute for Occupational Safety and Health
NMC	National Meteorological Center (now National Centers for Environmental Prediction)
NRC	National Research Council
NV	Nevada
NWR	Northwestern US Receptor
OMI	Ozone Measurement Instrument
OR	Oregon
PBL(H)	Planetary Boundary Layer (Height)
PDT	Pacific Daylight Times
PM	Particulate Matter
PM _{2.5}	Fine Particulate Matter (diameter≤2.5 micrometer)
PTR-MS	Proton-Transfer-Reaction Mass Spectrometry
RAQMS	Real-time Air Quality Modeling System
RMSE	Root Mean Square Error
RPPP	Radiative Power Per Plume
SAE	Solar Absorption Efficiency
SC	South Coast

SCAPE	Simulating Composition of Atmospheric Particles at Equilibrium
SCR	Southern California Receptor
SD	Standard Deviation
SLP	Sea Level Pressure
SP2	Single Particle Soot Photometer
SSA	Single Scattering Albedo
SS	Sea Salt
STEM	Sulfur Transport and dEposition Model
TBC	Top Boundary Conditions
TBG	Transported Background
TES	Tropospheric Emission Spectrometer
THD	Trinidad Head
TSVD	Truncated Singular Value Decomposition
TUV model	Tropospheric Ultraviolet-Visible radiation model
UNEP	United Nations Environment Programme
US	United States
USGS	US Geological Survey
UTC	Co-ordinated Universal Time
UTLS	Upper Troposphere/Lower Stratosphere
UV	Ultraviolet
VMR	Volume Mixing Ratio
W126 MI	W126 Monthly Index
WA	Washington
WMO	World Meteorological Organization
WRF	Weather Research and Forecasting model

WY

Wyoming

Greek and non-alphabetical Symbols

μm

micrometer

μg

microgram

ε

retrieval error

λ

adjoint variable

ϕ

forcing term

∂

partial derivative operator

ρ

air density

∇

gradient operator

δ

variation

σ

standard deviation

%

percent

\pm

plus/minus

Superscripts

T

transpose

°

degree

-1

inverse

Alphabetical Symbols

A_{TES}

averaging kernel matrix for TES

$A_{\text{OMI}}^{\text{vmr}}$

averaging kernel matrix for OMI (vmr)

$A_{\text{OMI}}^{\text{DU}}$

averaging kernel matrix for OMI (DU)

B

background error covariance matrix

C_i

concentration of a chemical species i

C_0

initial conditions

C_0^b	initial conditions (background)
E_i	the local sources term
F	a tensor function
F_{TES}	interpolation operator from STEM to TES grid
Gg	gig gram
H	derivative of $h(c_i)$
$h(c)$	vmr form of observation operator
hPa	hectopascal
h_z	natural log form of observation operator
J	cost function
K	turbulent diffusivity tensor
km	kilometer
L_i	the local sink term
m	meter
mg	milligram
MW	megawatt
O	observation error covariance matrix
p	model parameter
P_i	pressure at OMI pressure level i
P	error covariance matrix for model parameter
p_0^b	model parameter (background)
ppb	parts per billion
ppm	parts per million
r	correlation coefficient
sec	second
S1	absolute sensitivity

S_2	relative sensitivity
t	time
u	wind field vector
y_i	observation at time i
z	natural log form of true state
z_c	natural log form of constraint vector
\hat{z}	natural log form of estimated state (retrieval)

CHAPTER 1

INTRODUCTION

1.1 Background and significance

1.1.1 Tropospheric ozone and aerosols

The unevenly distributed short-lived air pollutants and climate forcers (such as tropospheric ozone (O₃ thereafter) and particulate matter (PM)) affect chemical cycles, create/exacerbate air quality problems, and induce climate change impacts at local, regional and global scales. The chemical, environmental, and climate significance of O₃ and selected aerosol species, their atmospheric lifetimes and current national standards are summarized in Table 1.1. It has been recognized that the distributions of these species can be attributed to local/regional and distant emission sources (for O₃, stratospheric O₃ is also a contributor), through complicated processes that occur on synoptic, meso- and micro-scales (Task Force on Hemispheric Transport of Air Pollution (HTAP), 2010; National Research Council (NRC), 2009). The mitigation of their climate and health impacts would benefit from efforts to control/reduce the emissions of these species and their precursors from various sources (United Nations Environment Programme (UNEP) and World Meteorological Organization (WMO), 2011), and the impacts of these reductions would be immediate due to their short lifetimes (compared to carbon dioxide (CO₂) and methane (CH₄)). Therefore, a better understanding of the processes that determine O₃ and PM distributions in the complex atmospheric system and a better ability to perform source attribution would help improve the predictability of their pollution levels, and assist making sound policy decisions and implement effective controlling strategies, in both short-term and long-term.

For the short-term air quality and climate benefits, the US Environmental Protection Agency (EPA) had proposed to lower the federal 8-hour primary O₃ standard from current 75 ppb to a level within 60-70 ppb. EPA also proposed to establish a seasonal "secondary" standard in the form of "cumulative peak-weighted index" (W126) within the range of 7-15 ppm-hours,

instead of the current secondary O₃ standard of 75 ppb (US EPA, 2010)). The proposal was withdrawn in 2011 per the request of President Obama (<http://www.whitehouse.gov/the-press-office/2011/09/02/statement-president-ozone-national-ambient-air-quality-standards>), and the next revision is expected to occur in 2013 based on the most recent scientific evidence of O₃ impacts on human health and welfare. The primary standard (to protect human health) tend to focus on acute O₃ pollution episodes while the secondary standard (to protect welfare including vegetation and sensitive ecosystems) is suggested to focus on long-term chronic exposure. The W126 metric is generally viewed as better assessing vegetation impacts than other metrics that calculate the average values such as AOT 40 and SUM 60 (Mauzerall and Wang, 2001; Heath et al., 2009), because it includes both the peak and the duration of O₃ concentrations, and the higher hourly average O₃ concentrations are given greater weights. Based on the data during 2006-2008, larger non-attainment areas (Figure 1.1) and higher costs for reducing air pollution levels are expected in response to the potential new thresholds (McCarthy, 2010). Thus, making accurate estimates of the pollution levels and the background (defined as the concentration that is not affected by recent locally-emitted/produced anthropogenic emissions, below which the air quality standard is not recommended to be set), including variability in its various components (such as long-range transport (LRT) of pollution, stratospheric O₃, natural sources such as biogenic and biomass burning emissions) will help evaluate the potential air quality standards and implement controlling strategies. Furthermore, as the science community is preparing for the Intergovernmental Panel for Climate Change 5th assessment report (IPCC AR5), accurate simulations of both magnitude and spatial distribution of O₃ and PM would improve the quality of subsequent radiative forcing calculations, which is an important factor in climate change (Agheto et al., 2011).

For the long-term air quality and climate benefits, O₃ and PM are currently controlled by air quality regulations without consideration of their effects on climate. Treating air pollution and climate change in common policy frameworks is recommended to be a long-term goal (Arneeth et al., 2009; Unger et al., 2009; Shindell et al., 2008). However, with high uncertainties, recent

studies (Levy et al., 2008; Shindell et al., 2008) have shown that changes in pollutant and precursor emissions, atmospheric burden, and radiative forcing are not necessarily proportional. Therefore, developing policy metrics reflecting the combined climate and air quality implications is important but challenging for achieving this goal.

1.1.2 Western US air quality

The western US is the focus of this study. It has a wide range of terrain types including mountains, valleys, water (oceans, rivers and lakes) and deserts, and also has varied climate because of the wide span of latitudes and the complexity of the terrain. The population and economy have grown rapidly over these regions in the past 20 years, especially in the state of California (CA), which is the most populous and the third largest state by area in the US (2010 Resident Population Data, US Census Bureau, <http://2010.census.gov/2010census/data/apportionment-pop-text.php>). Although substantial progress in reducing concentrations of many major air pollutants and their precursors have been made in the past 20 years (e.g., reducing nitrogen oxides (NO_x) by 34 %, Volatile Organic Compounds (VOCs) by 57%, Carbon Monoxide (CO) by >70 %, respectively over CA, Cox, 2010), there still exist large nonattainment areas for O₃ and fine particulate matter (PM_{2.5}) (Figures 1.1-1.2). In addition, the estimates of the contributions from distant and local anthropogenic and natural sources (biogenic, biomass burning, etc) have large uncertainties.

1.1.3 Integrated modeling-observation study

Reducing the uncertainties in model predictability and source contribution estimates will benefit future air pollution and climate policies. Over the past few decades, our ability to measure atmospheric composition and simulate the atmospheric chemistry has been significantly improved, but air quality predictions and source attribution still remains a challenging problem, with uncertainties associated with quality of model key inputs, missing science elements and poor parameterization, model resolution, etc. Thus, better predicting air quality and understanding the processes that determine the pollutants' distributions require the

integration of three-dimensional chemical transport modeling and observational-approaches (NRC, 2009; HTAP, 2010; Carmichael et al., 2008). Modeling studies provide multi-dimensional context for observations to assist the design/improvement of observational networks and help evaluate the individual chemical and physical processes that influence the observations. Observations can be used to assess and improve the model performance and the quality of its inputs (such as meteorological fields, emission estimates and boundary conditions), and can provide insights into the information/processes outside of the regional model domain.

1.1.4 Overall research goal and method

This study has three major objectives: 1) to understand the factors (such as transport and emissions) that determine O₃ and PM distributions in the complex atmospheric system; 2) to quantify and/or minimize the uncertainties in model predicted O₃ and PM; and 3) to embed the air quality and climate implications from 1) and 2) in policy-relevant context. Although this study has a strong focus on summertime western US, some comparisons between western US and other US regions, as well as between summertime and springtime will be included in certain parts of the study.

Regional-scale modeling tools and available observational products are combined to better address these issues, and to assess the current computational and methodological limitations in order to answer the scientific/technical questions associated with the establishment of future observational system (e.g., extended ozonesonde network, measurements on regional airlines, and geostationary satellites including Geostationary Coastal and Air Pollution Events (GEO-CAPE) over the North America (NA)) as well as the development of next generation community models, and the combination of global and regional modeling tools. Specific research objectives will be listed in Section 1.3.

1.2 Model and observations

The studied period is mid-June to mid-July, 2008, during which period the Arctic Research of the Composition of the Troposphere from Aircraft and Satellites (ARCTAS) field

campaign (<http://www.espo.nasa.gov/arctas/>) was conducted by National Aeronautics and Space Administration (NASA) (Jacob et al., 2010). Observations were made on various platforms, and several global and regional modeling teams conducted forecast and reanalysis to support this experiment.

1.2.1 STEM model

The studied period is simulated, using the Sulfur Transport and dEposition Model (STEM)–Version 2K3, one of the regional models that assisted in flight planning during the ARCTAS-CARB campaign. This model has been also used during a number of field experiments in the past decade. A detailed description of the most updated STEM-2K3 model can be found in Adhikary et al. (2010). The STEM model solves the equation to calculate the concentration of a given chemical species (C_i) from an eulerian view point as shown in (1.1):

$$\frac{\partial C_i}{\partial t} = \left[\frac{\partial C_i}{\partial t} \right]_{TRANSPORT} + \left[\frac{dC_i}{dt} \right]_{LOCAL} \quad (1.1)$$

where the transport operator (advection; turbulence) is: $\frac{\partial C_i}{\partial t} = -u \cdot \nabla C_i + \frac{1}{\rho} \nabla \cdot (\rho K \nabla C_i)$;

and the local (chemistry) operator is $\frac{dC_i}{dt} = E_i - L_i$

u represents the wind velocity vector, K is the turbulent diffusion tensor, and ρ is the air density. E_i and L_i represent local sources and sinks (reflect emissions, transformations, etc), respectively.

The STEM modeling system applied here includes three components (study flow chart shown in Figure 1.3):

- 1) A hemisphere tracer model to study long range transport of pollutants on a 60×60 km polar stereographic grid and includes 30 vertical layers to the stratosphere, and with a 6-hour output time resolution;
- 2) A continental scale gas-phase and aerosol chemical transport simulation on a subset of 1), and includes 18 vertical layers with the same intervals as the 1) (i.e., the 18 lowest layers to the top troposphere/lower stratosphere), and a 6-hour output time resolution;

- 3) A regional-scale gas-phase and aerosol chemical transport domain centered over the western US on a 12 km×12 km Lambert conformal conic grid and includes 32 vertical layers at smaller intervals than in 1) and 2), and a 1-hour output time resolution.

The 60 km simulations represent the general picture of pollutant distributions over the eastern Pacific and the continental US, while the 12 km cases concentrate on detailed pollutant spatial and temporal distributions under the impacts of transport and local productions over the western US.

The 60 km tracer and full-chemistry domains were described in detail in Huang et al. (2010a, 2012). This model calculates a variety of aerosols, as well as several air mass markers. The calculations are based on simple decay rates, and include dry deposition and wet scavenging. Carbon Monoxide is one of the primary tracers used to estimate the contributions of geographic areas to hemispheric-scale transport, because of its long atmospheric life-time of 1-2 months. The tracer system included both anthropogenic and biomass burning CO tracers. The anthropogenic tracers included: the U.S. mainland; Alaska; Canada; Greenland; Europe; Russia; China; and other Asia nations. Three biomass burning tracers (North America, North Asia/Russia, and South Asian/Africa) were also included. The tracer calculations also include estimates of air mass age, which represents a combination of transport time, source intensities and diffusion, using ethane emission and decay rates as a proxy (Tang et al., 2004).

The full-chemistry version of STEM model calculates 225 gas phase chemistry reactions based on SAPRC 99 gaseous chemical mechanism (Carter, 2000), with thirty different photolysis rates calculated by the online Tropospheric Ultraviolet-Visible radiation model (TUV) (Madronich, 2002). STEM also couples a four-bin aerosol module (0.1-0.3 μm , 0.3-1.0 μm , 1.0-2.5 μm and 2.5-10.0 μm) with thermodynamics calculated using the Simulating Composition of Atmospheric Particles at Equilibrium (SCAPE II) model (Kim and Seinfeld, 1995).

1.2.2 Sensitivity analysis and data assimilation

Two types of sensitivity simulations/analyses are applied in this study. Model forward sensitivity studies quantify the response of chemical distributions in all grids at future times to the perturbations of model inputs (e.g., emissions and boundary conditions) or parameterizations. In contrast, in adjoint sensitivity analysis, the distributions of the adjoint variable λ_n in the entire computational domain, named as “instantaneous areas of influence” (Sandu et al., 2005), reflect backward in time the change of chemical distributions of the species n in grids that influence the response function (e.g., O₃ concentrations at given receptor at a specific time). Combining the forward and adjoint sensitivity help understand the contributions and effects of various sources/processes to the state of atmosphere and interpret the sources of model biases.

Data assimilation (DA) is also applied to improve modeled O₃ distributions over the western US. DA is an efficient mathematical method to improve the model performance with the measurements incorporated. Four dimensional variational (4-d var) method has shown moderate/strong capabilities of improving modeled O₃, compared to other data assimilation techniques (Singh et al., 2011; Wu et al., 2008). The 4-d var method requires a minimization routine, a model and its adjoint, and the detailed configuration of the O₃ 4-d var DA is described in Chapter 2.

1.2.3 Observational products

Various types of observational data collected on different platforms, including satellite remote sensing products and flight and surface *in-situ* measurements are used as model inputs, and to evaluate/interpret or improve model performance (summarized in Table 1.2).

1.3 Specific objectives and thesis outline

The specific aims of this study include:

- 1) To set up a multi-scale STEM modeling system and simulate summertime gas and aerosol concentrations, which can be evaluated/improved by available observations and be used to study the transport/chemistry of pollutants.

- 2) To study the impacts of extra-regional sources on western US O₃ distributions.
 Tasks include: 1) evaluate the impacts of US versus non-US sources on O₃ levels at selected sites and model capability of capturing O₃ temporal variability there, and to demonstrate the connections of surface O₃ and O₃ aloft at previous times at these locations; 2) assess the relative importance of NA stratosphere and several O₃ precursor species in LRT plumes, to two policy-relevant O₃ metrics over different geographical regions and land types; 3) study effects of model horizontal and vertical resolution on representing the inflow transport/subsidence and the impacts on surface O₃; and 4) evaluate the extents of improvement in model predictability through assimilating several types of observations during a LRT transport episode.
- 3) To estimate sectoral and geographical contributions to BC distributions over the continental US (CONUS), and to evaluate the representativeness of several metrics that could help prioritize BC warming impacts on climate, as well as their sensitivities to reductions in sectoral emissions.

Chapter 2 discusses the impacts of extra-regional sources on western US O₃ distributions, using sensitivity analysis and data assimilation techniques, which is related to the specific aim 2). Chapter 3 demonstrates the sectoral and geographical contributions to the black carbon spatial distributions over the continental US, which is related to the specific aim 3. Finally, Chapter 4 summarizes this research and suggests the directions for future work.

1.4 Citations to published or presented work

The O₃ work in Chapter 2 has been previously presented out of campus at Jet Propulsion Laboratory (February, 2012), Sandia National Laboratory (February, 2012), TF HTAP workshop (February, 2012), and AGU Fall meeting (December, 2010, Huang et al., 2010b), and has been submitted to the journal of Atmospheric Chemistry and Physics entitled:

“Impacts of transported background pollutants on summertime western US air quality: model evaluation, sensitivity analysis and data assimilation”

The aerosol work in Chapter 3 has been published in: Huang et al. (2012)

The submission and revision of the following two peer-reviewed journal publications (Huang et al., 2010a, 2011) were also part of my PhD work.

Table 1.1 Environmental, chemical and climate significance of several species, their lifetimes and current national standards

Species		Tropospheric Ozone (O ₃)	Sulfur Oxides (SO _x): Sulfur Dioxide (SO ₂) and Sulfate (SO ₄)	Organic Matter (OM)	Black Carbon (BC)
Environmental significance		harmful to human health, environment and welfare, belonging to the six EPA "criteria pollutants"			
Chemical significance		affects oxidation cycles removing other polluting gases	critical to atmospheric removal processes heterogeneous chemistry modification of actinic fluxes and photolysis rates		
Climate significance (+/- indicate warming/cooling effects)	direct	greenhouse gas (+), warming potential well established	scattering & adsorption (-)	scattering & adsorption (mostly -)	scattering & adsorption (+), complicated in mixture
	indirect	oxides other gases	modification of clouds (-)	modification of clouds (-); co-change with black carbon	modification of clouds (-); co-change with organic carbon (OC)
		Inhibit/damage plants' natural uptake of CO ₂			
Lifetimes		22.3±2 days (Stevenson et al., 2006)	SO ₂ <2 days (Lee et al., 2011); SO ₄ : 2.6-5.4 days (Chin et al., 2009)	4.3-11 days (Chin et al., 2009)	5.3-15 days (Chin et al., 2009)
Current national standards		Primary: 75 ppb (8-hour); 120 ppb (1-hour), possibly be further lowered to a value between 60-70 ppb (8-hour); Secondary: now same as primary, but will be at a level within 7-15 ppm-hours	75 ppb (1-hour) and 140 ppb (24-hour) for SO ₂	Fine particulate matters (PM _{2.5}): 35µg/m ³ (24-hour); 15 µg/m ³ (annual)	

Table 1.2 Observations used in this study and purposes

Observations			Model Input	Model Evaluation/ Interpretation	Model Improvement	Platform/ Networks
Flight (<0.5 km to ~12 km)	Gases	O ₃ , NO _y , CO, PAN, acetonitrile		X		DC-8 (flight tracks by day in Figure 1.4)
	Aerosols	BC, SO ₄ , OM, NO ₃ , SSA		X		
Ground	Gases	O ₃ , NO ₂		X	X	EPA AQS, CASTNET
	Aerosols	BC, SO ₄ , OC		X		IMPROVE, EPA urban (CSN&NIOSH)
Sondes	Gases	O ₃		X	X	ARC-IONS 2008 at Trinidad Head, California
Satellites	Wildfire characteristics		X	X	X	MODIS, MISR
	Gases	O ₃	X	X	X	OMI, TES
	Cloud fraction			X		MODIS

Abbreviations: AQS: Air Quality System; ARC-IONS: Arctic Intensive Ozonesonde Network Study; CASTNET: Clean Air Status and Trends Network; CSN: Chemical Speciation Network; EPA: Environmental Protection Agency; IMPROVE: Interagency Monitoring of Protected Visual Environments; MISR: Multi-angle Imaging SpectroRadiometer; MODIS: Moderate Resolution Imaging Spectroradiometer; NIOSH: National Institute for Occupational Safety and Health; OMI: Ozone Measurement Instrument; PAN: peroxyacetyl nitrate; SSA: Single Scattering Albedo; TES: Tropospheric Emission Spectrometer.

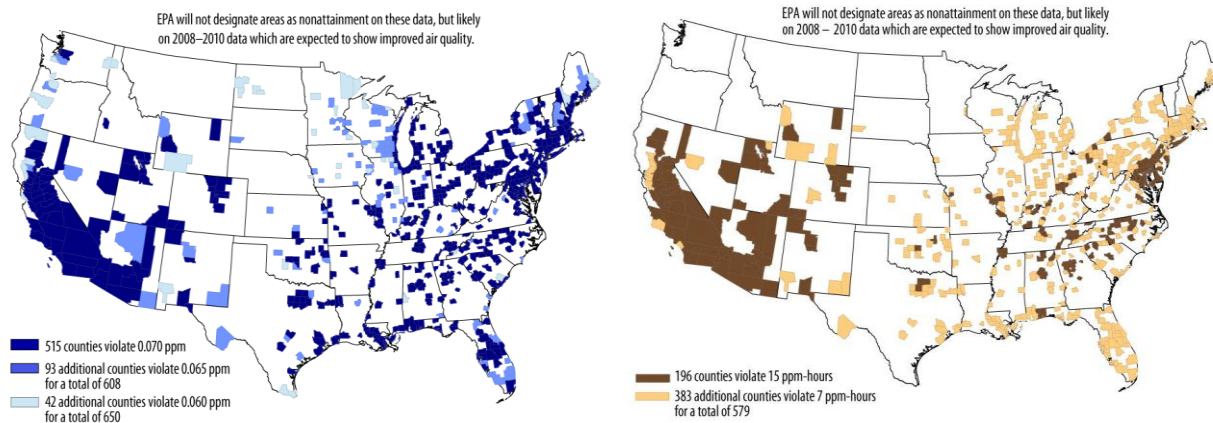


Figure 1.1 The US O₃ nonattainment areas based on projected standards and 2006-2008 O₃ data for eight-hour average (left) and W126 (right) O₃ metrics (McCarthy et al., 2010)

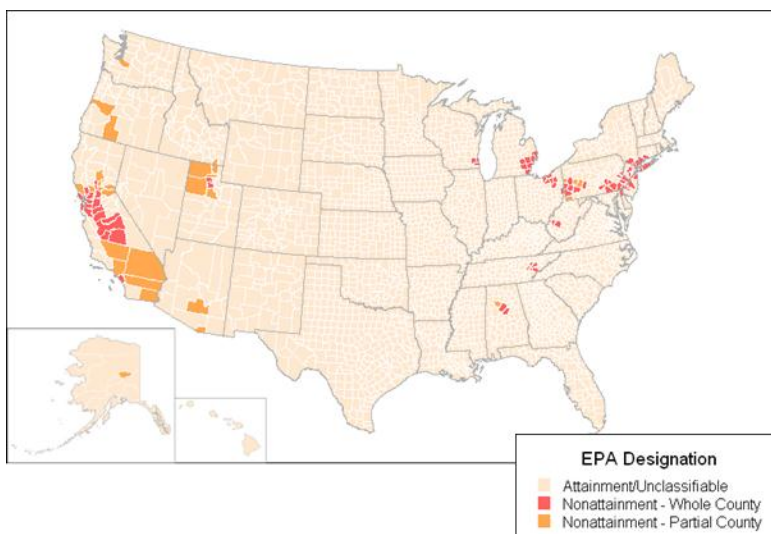


Figure 1.2 Map of 24-hour PM_{2.5} nonattainment areas (source: US EPA, 2011, <http://www.epa.gov/pmdesignations/2006standards/regs.htm#4>)

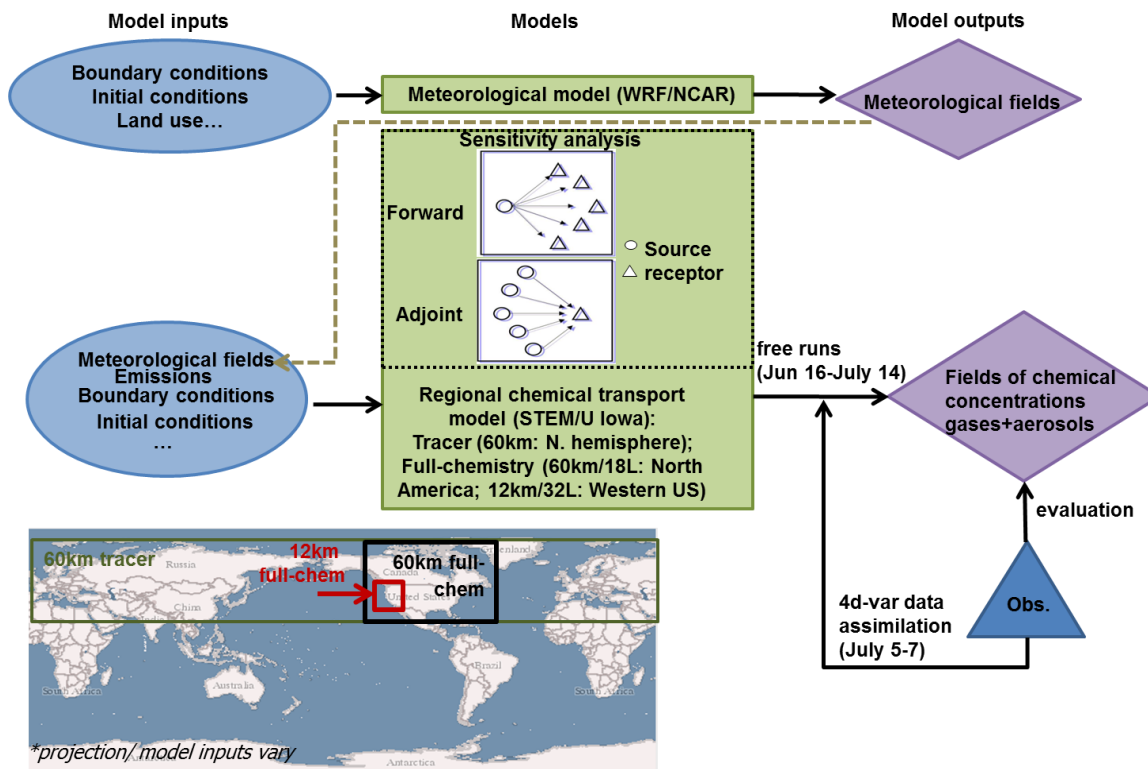


Figure 1.3 The flow chart of this study and model domains

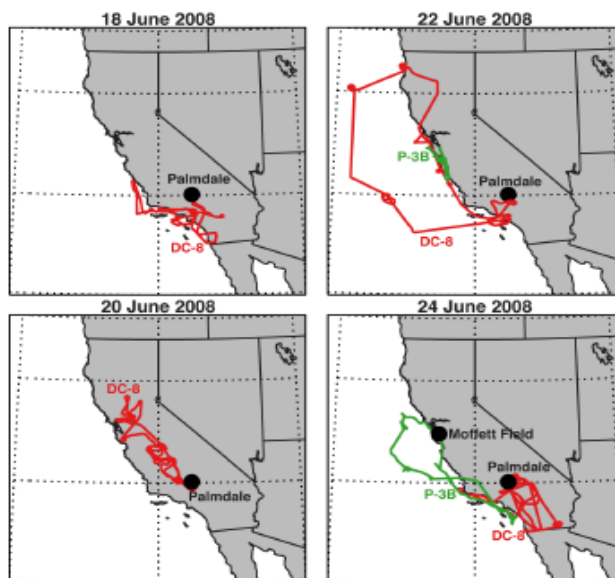


Figure 1.4 Flight tracks during the ARCTAS-CARB deployment (Jacob et al., 2010)

CHAPTER 2

IMPACTS OF TRANSPORTED BACKGROUND POLLUTANTS ON SUMMERTIME WESTERN US O₃ DISTRIBUTIONS

2.1 Introduction

Transported background (TBG) ozone (O₃) and its precursors from the eastern Pacific and the lower stratospheric O₃, together with the locally-formed O₃ from anthropogenic and natural (such as biogenic/geogenic, lightening and biomass burning) emissions, affect the O₃ variability over the western United States (US) (Task Force on Hemispheric Transport of Air Pollution (HTAP), 2010; National Research Council (NRC), 2009). The contribution from TBG indicates the influences from extra-regional emission sources and the stratospheric O₃, and accounts for a significant part of the background O₃, defined as the concentration that is not affected by recent locally-emitted/produced anthropogenic emissions (HTAP, 2010). The magnitude of TBG is expected to increase as the emissions from international sources grow (HTAP, 2010). This trend is especially important in the context of US air quality standards, which are proposed to become more stringent to protect both human health and ecosystems. The US Environmental Protection Agency (EPA) proposed to lower the federal 8-hour primary O₃ standard to a level within 60-70 ppb, and the establishment of a seasonal "secondary" standard to protect sensitive vegetation and ecosystems, in the form of "cumulative peak-weighted index" (W126) within the range of 7-15 ppm-hours (US EPA, 2010)). The proposal was withdrawn in 2011 and the next revision is expected to occur in 2013 to protect health and welfare based on most recent scientific evidence (The White House Office of the Press Secretary, 2011).

Observational and modeling studies have been conducted to evaluate the impacts of extra-regional sources on western North America (NA) O₃ variability. Not only O₃ itself in the extra-regional plumes affects the NA O₃ concentrations, O₃ precursors (e.g., peroxyacetyl nitrate (PAN)) in these plumes can generate O₃ during the transport and subsidence processes (Alvarado et al., 2010; Zhang et al., 2008; Fischer et al., 2010, 2011; Mena-Carrasco et al., 2007; Walker et

al., 2010). Existing studies have shown that trans-Pacific transport episodes are frequent and intense during the spring time (Cooper et al., 2010; HTAP, 2010). There is growing recognition that contributions from extra-regional sources in summer are also important (Bertschi et al., 2004; Jaffe et al., 2004; Parrish et al., 2010; Pfister et al., 2008, 2011a,b; Huang et al., 2010a). However, most of the summertime studies focused on O₃ itself in extra-regional plumes.

Modeling studies have been used to estimate the extra-regional contributions to US pollution levels or background O₃ levels. To date, most of these studies use global models with horizontal resolution ranging from several degrees to ~half degree and perturb emissions from various source regions/sectors by 20% or 100% (HTAP, 2010; Zhang et al., 2011; Lin et al., 2012). The estimated extra-regional contributions from these studies by different model configurations vary significantly in terms of magnitude and seasonal variability, and thus remain large uncertainties. One source of uncertainty derives from the model resolution. The advantages of using finer model resolution in representing the pollutant import/export processes have been demonstrated (Lin et al., 2010; Wild and Prather, 2006), especially over urban areas and the regions with complex terrain. Results indicate that increasing model horizontal resolution may result in higher estimates of extra-regional contributions to the western US (Zhang et al., 2011; Lin et al., 2012). Model vertical resolution is also critical for representing boundary layer structure, fluxes and vertical mixing (Saide et al., 2011 and references therein), which are the key processes that are associated with inflow subsidence. The impacts of model vertical resolution on the sensitivity of NA O₃ distributions to extra-regional pollutants are not well characterized. Another source of uncertainty is that due to the extrapolation of emission perturbation results to estimate source attribution. Using global models, Fiore et al. (2009) and Wild et al. (2012) have shown that the estimates of absolute contribution from European NO_x emissions to NA O₃ levels between those extrapolated from 20% perturbations were lower than those based on 100% perturbations, and the extent of the differences depended on season. A better understanding of the non-linear effects of NA surface O₃ in response to perturbations of various species in extra-

regional plumes is needed, especially in light of the fact that future emission scenarios indicate a wide range of possible emission changes.

Various types of observations over three dimensions are available to characterize pollution distributions and their evolution, and the capabilities for observational-based estimates of extra-regional pollutants are also increasing (Ambrose et al., 2011; Cooper et al., 2011; Parrish et al., 2009; Langford et al., 2011; Wigder and Jaffe, 2012). These include: surface observations from monitoring programs and research sites at remote locations which provide valuable information for identifying inflow characteristics and estimating the extra-regional contributions; aircraft *in-situ* measurements and sondes, which provide information on pollutant vertical structures and can be extensive during field campaigns; and satellite measurements that routinely provide broad geographic coverage, and which are taking efforts to improve the near-surface sensitivity of the retrievals (e.g., combined retrieval of the ultraviolet (UV), infrared (IR) and visible (Vis) spectral ranges, Worden et al., 2007; Zoogman et al., 2011), and to better characterize/represent the upper troposphere vertical structures (Pommier et al., 2011; Moody et al., 2011).

Improving our understanding of the impacts from extra-regional sources on NA O₃ distributions requires a closer integration of the observations and models, and will benefit from better understanding of the chemical and physical processes associated with the transport/subsidence processes and further improvements in the current observation system. These improvements can be also guided by sensitivity studies and data assimilation (DA) techniques (Bouttier and Courtier, 1999; Carmichael et al., 2008; Sandu and Chai, 2011) to: 1) assess the degree to which the current observations can detect/represent long-range transport (LRT) airmasses and reduce model uncertainties; 2) help identify regions where additional observations (such as extended O₃ sonde networks, profiles from regional airlines) may be valuable; and 3) provide suggestions for future geostationary satellite missions that are expected to have higher spatial coverage and temporal resolution (Committee on Earth Observation

Satellites (CEOS), 2011, http://www.ceos.org/images/ACC/AC_Geo_Position_Paper_v4.pdf;
 Geostationary Coastal and Air Pollution Events (GEO-CAPE), <http://geo-cape.larc.nasa.gov/>).

In this chapter, the STEM regional-scale modeling system is used to address the issues raised above. Specifically we study the impacts of extra-regional pollutants on western US surface O₃ during a one-month period in summer (mid-June to mid-July) 2008 when the Arctic Research of the Composition of the Troposphere from Aircraft and Satellites (ARCTAS) field campaign was conducted (<http://www.espo.nasa.gov/arctas/>) by National Aeronautics and Space Administration (NASA). This study extends the findings in Huang et al. (2010a), which focused exclusively on O₃ over CA during a short period (~one-week period during the California (CA) phase of the ARCTAS campaign), by: extending the study period; expanding the study domain to western US; and extending the analysis to 1) assess the relative importance of NA stratosphere and various TBG pollutants to two policy-relevant O₃ metrics over different geographical locations and land types; 2) compare the TBG with other contributors to background O₃; and 3) evaluate the effects of model horizontal and vertical resolution on representing the inflow transport/subsidence processes (Section 2.3.1). Ozone sources at selected sites are analyzed in detail, as well as the processes that connect the airmasses aloft with surface O₃ (Section 2.3.2). Finally, a case study demonstrates the value of various observations in identifying LRT episode and improving model predictability through DA (Section 2.3.3).

2.2 Data and methods

2.2.1 Study period, meteorological conditions and fire activities

The study period spans from 16 June to 14 July, 2008, during which the NASA ARCTAS-CARB and ARCTAS-B field experiments were conducted (Jacob et al., 2010).

Climatologically, the central and eastern Pacific during summertime is dominated by a surface high pressure system, while Asia and the western Pacific experience a low pressure system associated with the seasonal monsoon. Fuelberg et al. (2010) generalized synoptic conditions during 18 June-13 July, 2008, and found no major departures from climatology.

Cyclones were frequent and intense, mostly forming over Northern Russia and Canada, but had little impact on California (CA). The jet stream at 300 hPa was located over central China (close to climatology) and northern Asia (with strong positive anomaly).

Fire activity was overall high during summer 2008 over CA, Canada, and Eurasia. Rapid PAN conversion from fire-emitted NO_x was indicated, and the lifting of emissions above the boundary layer due to buoyancy led to LRT events (Jacob et al., 2010). LRT of anthropogenic and fire plumes together with NA fires plumes were frequently sampled by the DC-8 during ARCTAS (<http://www.espo.nasa.gov/arctas/flightDocs.php>). Compared with previous years fire records (Table 2.1), the 2008 Siberia fire counts and total radiative power were higher, but with a lower value of radiative power per plume (RPPP) than those in 2002-2003 (Bertschi et al. (2004) and Jaffe et al. (2004) studied the summer 2003 Siberia fire impacts on northwestern US, as cited in Section 2.1).

A record lack of rainfall, severely dry vegetation and uncharacteristically windy weather combined to cause the strong fire activity over CA, the majority of which started from 20-21 June due to lightning and dry thunderstorms over northern and central CA. The same thunderstorms also caused fires in OR. The areas burned in 2008 (1,593,690 acres) far exceeded previous years (2003-2007 five-year average: 757,986 acres, <http://www.fire.ca.gov/downloads/redbooks/2008/02-wildland-statistic-all-agencies/11-2008-FIRE-SUMMARY.pdf>). Fires can result in O_3 enhancements, which are shown to be intensified when interacting with urban smog over CA (Singh et al., 2012).

2.2.2 Observation data

The observations used as model inputs and to evaluate/improve the model performance are summarized in Table 2.2. They include:

1) Ozone sondes: Twenty O_3 sondes launched (8 in June, 12 in July) at Trinidad Head (THD, topography ~20 m above sea level (ASL)), mostly at ~19-22 UTC (noon-3 pm local time (LT)) in support of the ARCTAS experiment. THD is a coastal remote air quality measurement

site located in northern CA, which is thought to well represent the properties of airmasses entering the US (Oltmans et al., 2008);

2) Surface O₃ measurements: Hourly O₃ at all US EPA Air Quality System (AQS) and Clean Air Status and Trends Network (CASTNET) sites in CA, Nevada (NV) and Oregon (OR), Washington (WA) and Idaho (ID) (multiple measurement methods in Table 2.2); and hourly O₃ measurements by UV Photometric Ozone Analyzer at Mt. Bachelor Observatory (MBO, topography ~2.7 km ASL). This high-altitude site has been demonstrated to represent LRT of pollution into the northwestern US (e.g., Fischer et al., 2010, 2011; Weiss-Penzias et al., 2007; Ambrose et al., 2011);

3) Satellite products: Measurements from the Tropospheric Emission Spectrometer (TES) and Ozone Monitoring Instrument (OMI), both on board the NASA Aura satellite, which has an ascending equator crossing time of ~13:45 LT were used. TES Level 3 carbon monoxide (CO) and tropospheric O₃ columns on multiple days were used to locate the movement of transported pollutants from Asia to the western US, and the Level 2 V004 nadir O₃ vertical profiles from special observations (in the “step-and-stare” mode where the separation between observations is ~35 km along the orbit (Beer, 2006)) were used for evaluating the model performance over the eastern Pacific and for DA on 5 July. TES Level 2 V002 data had 3-10 ppb of positive biases in 2004-2006 over sondes (Nassar et al., 2008) and 5-15% positive biases over Light Detection And Ranging (LIDAR) profiles in 2006 (Richards et al., 2008), and V003/V004 data had an overall positive bias (<+15 %) over sondes during ARCTAS over high latitude regions (Boxe et al., 2010). The TES retrieval does not have the capability of resolving the boundary layer O₃ distribution except in summertime when there is strong thermal contrast between ground and air; OMI Level 2 V003 O₃ vertical profiles where cloud fraction=0 (selected by Moderate Resolution Imaging Spectroradiometer (MODIS) MOD06_L2 cloud products (Platnick et al., 2003) as suggested by Russell et al., 2011) were also assimilated on 5 July. The OMI vertical profiles have larger horizontal coverage but much lower vertical resolution than TES, showing overall positive biases ranging from <10% to ~30% (Wang et al., 2011; Kroon et al., 2011) for mid-

latitude regions, with lower sensitivity at lower and upper troposphere (Veefkind et al., 2009); Daily total O₃ columns from OMI were used in the online Tropospheric Ultraviolet-Visible (TUV) radiation model (Madronich, 2002) to generate the photolysis rates for STEM; and

4) Aircraft measurements: PAN, total oxides of nitrogen (NO_y), O₃ and CO sampled on the 22 June DC-8 flight off shore of CA. These observations were used to evaluate the model boundary conditions, which were perturbed in the forward sensitivity simulations as described in Section 2.2.3.2.

2.2.3 STEM model experiments and input data

We simulated the 29-day study period using tracer and full-chemistry versions of STEM (2K3) modeling system, including its forward and adjoint versions, which have been used and evaluated in a number of field campaigns in the past decade (Carmichael et al., 2003a, b; Tang et al., 2007; Adhikary et al., 2010; Tang et al., 2004; Stith et al., 2009; D'Allura et al., 2011).

The tagged tracer version of STEM calculates a variety of aerosols and several air mass markers (such as CO, sulfur oxides, black carbon, primary organic carbon, dust and mercury). Because of its long atmospheric life-time (1-2 months), CO is a commonly used tracer to estimate the contributions of geographic source areas to hemispheric-scale transport. The tracer system used here focused on primary emitted CO only, including eight anthropogenic (the US mainland, Alaska, Canada, Greenland, Europe, Russia, China, and other Asia nations) and three biomass burning (North America, North Asia/Russia, and South Asian/Africa) tracers. Estimated air mass ages based on simple chemical clocks were also calculated as described in Tang et al. (2004). The full-chemistry version of STEM uses 225 gas-phase chemistry reactions based on the SAPRC 99 gaseous chemical mechanism (Carter, 2000) with thirty photolysis rates calculated online by the TUV model.

A set of simulations were performed using a continental scale 60×60 km polar stereographic grid with 18 vertical layers from surface to top of the troposphere (~11-12 km above ground level (AGL)), similar as in Huang et al. (2010a). They were analyzed to

characterize the general picture of pollutant distributions over the eastern Pacific and continental US. One base simulation (Case C0 in Table 2.3) and several forward sensitivity simulations, and two adjoint sensitivity simulations were conducted on this grid to compare the importance of various species (i.e., transported O₃ and its precursors, upper troposphere/lower stratospheric (UTLS) O₃) to the distributions of O₃ regulatory indexes over different geographical regions/land types, and for transport/subsidence process analysis. To discuss the impact of model vertical resolution on surface O₃ sensitivity to extra-regional pollutants, base and forward sensitivity simulations were also conducted on a 60×60 km/32 vertical layer grid.

A set of simulations were also conducted using a 12 km×12 km Lambert conformal conic grid over the western US, with 32 vertical layers from the surface to the top of the troposphere (~11-12 km AGL). They were used to study in greater detail the processes that link extra-regional inputs to the surface. A base simulation (Case F0 in Table 2.3), one forward and two adjoint sensitivity simulations were conducted on this grid for transport/subsidence process analysis.

The 18 layer grid had ~7 layers below 1 km and ~10-11 layers below 4 km, and the 32 layer settings had ~11 layers below 1 km and ~20-21 layers below 4 km.

2.2.3.1 Model inputs

Meteorology fields for the 60 km and 12 km grids were generated by the Advanced Research Weather Research & Forecasting Model (WRF-ARW) (Skamarock et al., 2007, 2008) driven by Global Forecast System and North American Regional Reanalysis data (Mesinger et al., 2006), respectively. The same physics options were used as in Huang et al. (2010a).

In the 60 km base case, lateral boundary conditions (LBCs) for thirty gaseous species and top boundary conditions (TBCs) for ten gaseous species (O₃, CO, NO, NO₂, NO₃, HNO₃, HNO₄, PAN, N₂O₅, and H₂O₂) were downscaled from archived 2°×2° Real-time Air Quality Modeling System (RAQMS) (Pierce et al., 2007) global real-time chemical analyses. The 60 km LBCs for black carbon, organic carbon, dust, sea salt and sulfate were taken from the 60 km hemispheric

tracer results introduced in Huang et al. (2012). The 12 km BCs came from the 60 km STEM full-chemistry simulations for both gas and aerosol species.

Since time-varying BCs downscaled from results in a coarser grid can significantly affect the regional model results (Tang et al., 2007; Huang et al., 2010a; Pfister et al., 2011a), we evaluated the BCs used in this study by comparing RAQMS and 60 km STEM results with 1) O₃, CO, PAN and NO_y sampled by the 22 June DC-8 flight over eastern Pacific, and 2) TES nadir tropospheric O₃ vertical profiles for the days that “step and stare” observations were available over eastern Pacific [150-120°W, 30-60°N] (Figure 2.1). RAQMS-modeled PAN, NO_y, and O₃ agree well with the flight observations on 22 June, with slight overprediction <4 km, while CO shows 40-50 ppb bias below 4 km, and low variability at higher altitudes. The 60 km STEM simulations are similar to RAQMS with slight improvement (e.g., for NO_y below 4 km). Both mean RAQMS and STEM 60 km O₃ profiles (with the TES observation operator (Section 2.2.4) applied) show good agreement with the TES retrieval (which usually has a positive bias up to ~15%), but underestimate the variability.

Emission inputs for the three modeling components differed, based on different demands for resolution and completeness (e.g., detailed VOC speciation). In the hemispheric tracer model, we used the most recent bottom-up global 1° × 1° gridded inventory developed by Q. Zhang and D. G. Streets for the ARCTAS mission (<http://www.cgrer.uiowa.edu/arctas/emission.html>). This inventory is based largely on the NASA INTEX-B inventory (Q. Zhang et al., 2009), and includes national-level information on fuels and activity by economic sector, including anthropogenic, biomass, and global shipping emissions. Anthropogenic emissions in the 60 km simulations were taken from the 2001 National Emissions Estimate Version 3 (NEI 2001), an update of the 1999 U.S. National Emissions Inventory with growth factors applied by Source Classification Code, and augmented with national inventories for Canada (2000) and Mexico (1999). Simulations with this inventory produced a significant negative bias for predicted sulfur species, especially over southern CA, as described in Huang et al. (2011). Biogenic emissions of monoterpene and isoprene were from twelve-year-averaged values from the Orchidee model

(Lathiere et al., 2006). Daily biomass burning emissions were provided by RAQMS (provided by the Cooperative Institute for Meteorological Satellite Studies). The total emissions were then unevenly distributed vertically from the surface to the 12th model level (~4-5 km), with nonlinear factors decreasing as the model height increased (i.e., 0.12,0.12,0.11,0.101,0.101,0.096,0.083,0.082,0.082,0.074,0.018,0.013). For the 12 km simulations over CA and during the ARCTAS-CARB mission period, we used daily-varying anthropogenic and biogenic emissions re-gridded from a recent California Air Resources Board (CARB) 4 km emission inventory (received in July 2009, by personal contact with A. Kaduwela and C. Cai in CARB). This inventory produced much better results for sulfur species than NEI 2001 but still showed negative biases (Huang et al., 2011). For the time period outside of the ARCTAS-CARB mission, we used averaged CARB emissions without daily variation. Anthropogenic and biogenic emissions outside of the CARB domain were taken from NEI 2001. Biomass burning total emissions were generated with PREP-CHEM-SRC (Freitas et al., 2011) by processing the MODIS-detected point fire information at 1 km ground resolution (Giglio et al., 2003; Davies et al., 2009). The total emissions were then unevenly distributed from surface to ~1.5-2 km, with the same nonlinear factors used the 60 km case. The injection heights were closer to the analyzed satellite (i.e., Multi-angle Imaging SpectroRadiometer (MISR)) wildfire plume injection heights during previous years over various regions, as summarized in Table 2.1).

2.2.3.2 Forward sensitivity simulations

Eleven forward sensitivity simulations were conducted in the 60 km/18 layer continental grid to study the impacts of extra-regional pollutants on O₃ distributions (Table 2.3, Cases C1-C11). To estimate the effects of the UTLS air masses on NA O₃, the O₃ concentrations at the TBC were perturbed by 50% in Case C1. Three simulations where O₃ concentrations at both TBC and LBC were reduced by 75%, 50%, and 25%, respectively (Cases C2-C4) were conducted to study the surface O₃ response curve to extra-regional O₃. To investigate the influence of extra-regional precursor species, another three simulations were performed in which

eight non-O₃ species (CO, NO, NO₂, NO₃, HNO₃, HNO₄, PAN, and N₂O₅) in the LBCs and TBCs were perturbed by 75%, 50% and 25%, respectively (Cases C5-C7). With specific interest in the impacts of transported PAN on O₃ levels, two simulations with PAN in TBC and LBC reduced by 50% and 75% were conducted (Cases C8-C9). In addition, PAN chemistry was partially (Case C10) and completely (Case C11) blocked in separate simulations, and the differences in PAN and O₃ levels between these represent the amounts of decomposed transported PAN, and its contributions to O₃.

Forward sensitivity simulations with TBC and LBC O₃ perturbed by 50% were also conducted: 1) under scaled US anthropogenic emissions (Case CR1) to compare with the sensitivities generated between Cases C0 and C3 in the 60 km/18 layer grid; and 2) in a 60 km/32 layer (Cases CL0/CL1) and the 12 km (Cases F0/F1) configurations to discuss the impacts of model resolution on the sensitivities.

Biomass burning and biogenic emissions were turned off in two additional emission sensitivity simulations (Cases CBB and CBG) to compare their contributions to background O₃ with the TBG at surface and selected sites (Sections 2.3.1.3 and 2.3.2.3).

2.2.3.3 Four-dimensional variational (4-d var) DA and adjoint sensitivity analysis

The performance of contemporary numeric models is highly dependent on model parameterizations, the quality of model inputs (e.g., emissions and meteorological fields), chemical mechanisms, and resolution (Stevenson et al., 2006; Shindell et al., 2006; Fiore et al., 2009; McKeen et al., 2009; Wild et al., 2012). Accurately modeling of air pollutants distributions still remains a challenge, especially for O₃ which is involved in complex chemical processes. DA is an efficient mathematical method to improve the model performance by integrating observations, and the 4-d var method has shown moderate/strong capabilities of improving modeled O₃, compared to other DA techniques (e.g., Singh et al., 2011; Wu et al., 2008). This method seeks the optimal solution to minimize the cost functional in equation (2.1):

$$J(c_0, p) = \frac{1}{2}(c_0 - c_0^b)^T B^{-1}(c_0 - c_0^b) + \frac{1}{2}(p - p^b)^T P^{-1}(p - p^b) + \frac{1}{2} \sum_{i=0}^N (h(c_i) - y_i)^T O_i^{-1}(h(c_i) - y_i) \quad (2.1)$$

where B , P , and O are error covariance matrices for the *a priori* model forecast (background), for any model parameters (such as emissions), and for available observations at any instant time $t = t_i$ within the assimilation window, respectively. h is a projection operator, calculating the observation vector $y = y(x, t)$ from the model space $c = c(x, t)$.

The 4-d var method minimizes equation (1) by applying minimization routines (in this study we use Quasi-Newton limited memory-Broyden-Fletcher-Goldfarb-Shanno (L-BFGS), a limited-memory quasi-Newton code for bound-constrained optimization as introduced by Zhu et al. (1997) and applied by Chai et al. (2006, 2007) in STEM 4-d var) through iterations, and requires a model and its adjoint. The evolution of the adjoint variable vector λ reads as

$$\frac{\partial \lambda}{\partial t} + \nabla \cdot (u\lambda) = -\nabla \cdot \left(\rho K \cdot \nabla \frac{\lambda}{\rho} \right) - (F \cdot \lambda) - \phi \quad (2.2)$$

where u is the wind field vector, ρ the air density, K the turbulent diffusivity tensor, and ϕ is a forcing functional vector which will be defined in Section 2.2.4. The backward integration of equation (2.2) gives adjoint variables at any time, and the variation of the cost functional due to small changes in initial conditions is

$$\delta J = \left[\lambda_0^T + (c_0 - c_b)^T \cdot B^{-1} \right] \cdot \delta c_0 \quad (2.3)$$

where $\lambda_0^T + (c_0 - c_b)^T \cdot B^{-1}$ is the gradient information needed for the minimization. In contrast to the model forward sensitivity studies which quantify the response of chemical distributions in all grids at future times to the perturbation of model inputs/parameters, the distributions of the adjoint variable λ_n in the entire computational domain, named as “instantaneous areas of influence” (Sandu et al., 2005), reflect backward in time the change of chemical distributions of the species n in grids that influence the response function (e.g., O_3 concentrations at given receptor at a specific time). The adjoint values can: 1) help understand the specific processes that lead to a state of the atmosphere; 2) identify areas where perturbations/uncertainties in the concentration of the chemical species of interest at earlier times

will result in significant changes in O₃ levels at the receptor site at future time; and 3) help explain the 4-d var DA efficiency. Adjoint sensitivity analyses and the 4-d var DA technique have been applied in a number of previous studies from global to regional scales for gases and aerosols (e.g., Zhang et al., 2009; Kopacz et al., 2010; Zoogman et al., 2011; Henze et al., 2009; Campbell et al., 2006; Carmichael et al., 2008; Chai et al., 2006, 2007, 2009; Hakami et al., 2005, 2006; Pan et al., 2007).

This study used STEM adjoint sensitivity simulations to understand the surface O₃ sensitivities at two selected receptor regions (i.e., northern CA and OR (NWR) and southern CA (SCR)) with respect to concentrations of O₃ backward in time during the 29-day period, noted as Cases FA1/FA2 and CA1/CA2 in Table 2.3, for the 12 km and 60 km/18 layer configurations, respectively. These cases help interpret the linkages between O₃ at surface and at upwind measurement sites, as well as the effect of model resolution on the forward sensitivities in Section 2.3.1.6. The adjoint simulations require completion of forward model simulations, and they used the same model inputs as in the forward simulations. In each case, 27 adjoint sensitivity simulations (spanning the period of 16 June-14 July) were conducted, with 00 UTC of each day during 18 June-14 July as the final time, and a simulation interval for each simulation of 49 hours.

Several types of observations (i.e., hourly surface O₃, and the vertical profiles on 5 July from THD sonde, TES and OMI) were assimilated into the 12 km grid starting from 5 July, 18 UTC to 7 July, a LRT episode detected by satellite and *in-situ* measurements (Ambrose et al., 2011). Ozone initial conditions were controlled in all DA cases (Table 2.4). The background error correlation matrix was prepared through the NMC (National Meteorological Center, now National Centers for Environmental Prediction) method as introduced by Chai et al. (2007), using the 3-day, 2-day and same-day forecasts and, and was inverted using the truncated singular value decomposition (TSVD). The construction of background variances followed the method in Singh et al. (2011). Observation error covariance matrices are diagonal, and the selection of observation errors for each case (in Table 2.4) took into account the instrument uncertainties and

the representative errors (due to the gap of spatial resolution between measurement and model resolution). Upper-limits of each chemical species (useful for the optimization routine, as described in Chai et al., 2006) varied vertically, and for O₃ they were set at 200 ppb from surface to mid-troposphere, and 400 ppb in the upper troposphere reflected by the satellite measurements on 5 July (Section 2.3.3). Twenty-five iterations were used in all DA cases, and the cost function decreased significantly after 12-15 iterations (e.g., >~40%, Figure 2.20f).

2.2.4 Observation operator and the forcing term

The observation operator $h(c)$, which can vary for different types of observations, enables the comparison of modeled O₃ fields with the observations, which is critical for 1) evaluating model performance with observations; and 2) calculating cost function and the forcing term for DA. For surface *in-situ* measurements and sondes, $h(c)$ is linearly-interpolated model output to the locations of the observations.

The TES retrieval follows (2.4) (Chapter 8, TES L2 data user's guide, Version 5.0, 2011):

$$\hat{z} = z_c + A_{\text{TES}}(z - z_c) + \varepsilon \quad (2.4)$$

where \hat{z} , z and z_c are the natural log form of the estimated state, true state, and constraint vectors for O₃ concentrations (in volume mixing ratio (vmr) units), respectively. ε is the TES observation error that assumed to have mean zero and covariance S (Bowman et al., 2006), and A_{TES} is the averaging kernel matrix (usually non-symmetric) reflecting the sensitivity of retrieval to changes in the true state (Rogers, 2000). Retrieval in vmr is $y = \exp(\hat{z})$. The TES observation operator h_z for O₃ is written in (2.5):

$$h_z = z_c + A_{\text{TES}} (\ln(F_{\text{TES}}(c)) - z_c) \quad (2.5)$$

where F_{TES} projects the modeled O₃ fields c to the TES grid using spatial and temporal interpolation. The resulting mismatches in vmr between TES retrieval and the model state are the differences of the exponential form of (4) and (5) (i.e., $\exp(\hat{z}) - \exp(h_z)$) at each location along

the orbit, which is used to calculate the cost functional in equation (2.1). Usually \mathcal{E} is much lower than the mismatches between model and the satellite retrieval.

The OMI observation operator is built upon the similar function of constraint vectors and averaging kernels as for TES, except that the O_3 concentrations in retrievals are in Dobson Units per layer, and should be converted to layer average by using (2.6):

$$\langle \text{vmr} \rangle_i \text{ (in ppmv)} = 1.2672 \times N_i / dP_i \quad (2.6)$$

where N_i is partial column in DU in the layer, and dP_i is the pressure difference between the bottom and the top of the layer in hPa. Accordingly, the OMI averaging kernel for the profiles in DU should be converted for the profiles in vmr using equation (2.7), following the instructions by Veefkind et al., 2009 and Zhang et al., 2010:

$$A_{OMIij}^{\text{vmr}} = A_{OMIij}^{\text{DU}} \times dP_j / dP_i \quad (2.7)$$

The forcing term ϕ in equation (2.2) appears as in equation (2.8)

$$\phi = H^T O^{-1} (h(c) - y) \quad (2.8), \text{ where } H = \partial h(c) / \partial c \text{ and } y \text{ is the observation}$$

For assimilating surface observations, h is assumed to be linear (i.e., $h(c) = H \cdot c$, where H reflects interpolation in space and time when constructing model counterparts of the observations). For assimilating TES and OMI profiles, we follow equations (2.9) and (2.10), respectively.

$$H^T = \left(\frac{\partial [\exp(h_z)]}{\partial c} \right)^T = \left(\frac{\partial [\exp(z_c + A_{\text{TES}} (\ln(F_{\text{TES}}(c)) - z_c))]}{\partial c} \right)^T = F_{\text{TES}}^T \frac{1}{F_{\text{TES}}(c)} \cdot A_{\text{TES}}^T \cdot \exp(h_z)^T \quad (2.9)$$

$$H^T = F_{\text{OMI}}^T \cdot A_{\text{OMI}}^{\text{vmr}T} \quad (2.10)$$

2.3 Results and discussions

2.3.1 Forward sensitivity of surface O₃ to boundary conditions

2.3.1.1 Model evaluation for base case surface O₃

Figure 2.2 compares two O₃ regulatory metrics at all EPA Air Quality System (AQS) and Clean Air Status and Trends Network (CASTNET) sites (231 AQS sites and 8 CASTNET sites in total that had data available for $\geq 75\%$ of the studied period and were located inside of both 60 km and 12 km model domains) with the model results generated in 60 km and 12 km grids. The two metrics are Monthly mean Daily maximum 8-hour Average O₃ (MDA8) and W126 Monthly Index (MI, calculation followed the method: <http://www.epa.gov/ttn/analysis/w126.htm>) for primary and secondary O₃ standards, which set limits to protect human health and public welfare, respectively. High O₃ concentrations are observed and modeled over the Central Valley and southern CA (with MDA8 > 75 ppb and W126 > 15 ppm-hours). Ozone levels over most areas of NV, OR and WA are lower (with MDA8 < 60 ppb and W126 < 7 ppm-hours). The 60 km and 12 km simulations present similar gradients, and the 12 km results capture more accurately the local features. The predictions show higher positive biases along the coast, larger in the 60 km grid. Positive bias in simulated surface O₃ is also found in other contemporary chemical transport model simulations in this region (e.g., Lin et al., 2012). The poorer performance over the coastal regions may be caused by inaccuracies in predicted meteorology associated with complicated land-sea breezes and topography, as well as the uncertainties in emissions (e.g., coarse resolution of biomass burning emissions) and the BCs.

Statistical comparisons between the observations and model simulations for MDA8 and W126 were calculated at these AQS (Tables 2.5) and CASTNET sites (Tables 2.6), including root mean square error (RMSE), mean bias ($bias = modeled - observed$), mean error ($error = |modeled - observed|$), mean fractional bias ($fractional\ bias = 2 \times (modeled - observed) / (modeled + observed)$) and mean fractional error ($fractional\ error = 2 \times |modeled - observed| / (modeled + observed)$)

(modeled+observed) /). The model performance is generally good for MDA8, similar to the contemporary community chemical weather forecast model evaluations (McKeen et al., 2009). The model performance for W126 is worse for W126 than for MDA8, due to the non-linear function used in calculation that may amplify the uncertainties at higher O₃ values. The 12 km results show lower bias, error and RMSE, and the model shows better performance at CASTNET sites than at AQS sites in both resolutions, due to the fewer number of CASTNET sites and weaker anthropogenic influences on these rural/remote locations.

2.3.1.2 Extra-regional contributions from tracer CO

Period-mean surface distributions of extra-regional CO% (both anthropogenic and biomass burning) are shown in Figure 2.3a-b for surface and the free troposphere, respectively. Approximately 5-10% higher extra-regional contributions are shown at the free troposphere than at the surface. Elevated values (>70%) over the eastern Pacific indicate two major LRT legs during this period. The lowest values (~5-10% extra-regional CO%) are shown over southern CA, while northern CA and coastal regions are most strongly affected by the extra-regional sources (>30% extra-regional CO%).

These results can be compared with those in a study by Pfister et al. (2011) who also used a regional chemical transport model to examine the CO budget over CA during this period. They used a different fire emission inventory (the Fire INventory from NCAR (FINN)) which possibly has an overall negative bias. Their results over CA reveal that $53 \pm 21\%$ and $78 \pm 16\%$ of CO at surface and free troposphere were from inflows, and about a quarter of them had Asian origin (the major extra-regional contributor). The magnitude of our results are broadly close to their findings over California (i.e., 5-30% and 10-40% from extra-regional sources).

2.3.1.3 Impacts of multiple trans-boundary species and NA stratospheric O₃ on surface O₃

The sensitivities of surface MDA8 and W126 metrics to various species in BCs were evaluated by a number of forward sensitivity simulations (Section 2.2.3.2), and the results were

averaged over ten EPA regions (Figure 2.4a-b). The largest sensitivities are found in the west (Regions 8, 9, and 10), which is less populated (text below Figure 2.4c) and has larger grass/shrub coverage (barplot in Figure 2.4c, grouped from the US Geological Survey (USGS) 24 land types used in the model simulations (Table 2.7)). The eastern US has a higher population density and larger forest coverage, and shows ~1/3 of the sensitivity to TBG pollutants as that for the west. For all EPA regions, surface MDA8 and W126 are most sensitive to TBG O₃, followed by PAN.

We further analyzed the sensitivity of MDA8 and W126 in Regions 9 and 10 over different geographical regions/land types to the size of BC perturbations for multiple species (Figure 2.4e-f). The extra-regional sources show strongest impacts on grass+shrub and smallest impacts on forest for all sensitivity cases. Both MDA8 and W126 show close-to-linear response to perturbations in non-O₃ species in BC, but small non-linear responses to perturbations in BC O₃ and PAN alone. MDA8 sensitivity over Region 9 shows stronger non-linearity to BC PAN perturbations than over Region 10, reflecting stronger local impacts.

Sonde-based studies have shown that the impacts of stratospheric O₃ may be the main reason for differences in summertime O₃ vertical structures over the northern and southern CA coasts (Cooper et al., 2007). Impacts of stratospheric O₃ over NA on surface MDA8 and W126 are smaller in the western US (Figure 2.4a-b), with the largest sensitivities (to 50% perturbation in TBC O₃) over the high topography regions of eastern ID, Wyoming (WY) and Colorado. The period-mean sensitivities over the eastern Pacific and northwestern coastal regions are slightly negative and slightly positive over southern CA in lower/mid troposphere (Figure 2.5). The largest impacts are in the upper troposphere O₃ (>~6 km, not shown), and are larger at higher latitudes. Note that these represent lower-limit estimates as some stratospheric-origin O₃ is included in LBC O₃.

The impacts of stratospheric O₃ can also be inferred from analysis of the O₃-CO relationship (e.g., slope/correlation), which have been used to mainly reflect the intensity of photochemical production, and degrade as the contributions of stratospheric O₃ and secondary

CO formation grow (e.g., Parrish et al., 1993, 1998; Chin et al., 1994; Li et al., 2002). The STEM-modeled O₃-CO correlation and slopes over the western US at ~2-4 km are close to DC-8 measurements during the ARCTAS-CARB mission (Figure 2.5) and the results from global model calculations and satellite retrievals in previous studies (Zhang et al., 2006; Voulgarakis et al., 2011). Lower values over the high altitude regions of ID and the Sierra Nevada indicate the impacts from stratospheric O₃ and secondary CO formation (according to the WRF-Chem calculations by Pfister et al. (2011b)), respectively. The higher values are shown over the eastern Pacific where PAN/NO_y ratios are high, indicating the LRT impacts.

2.3.1.4 TBG, biomass burning and biogenic emissions

contributions to background O₃

We calculated the contributions from TBG to surface O₃ by summing up the contributions from TBG O₃ and its precursors, extrapolated from the sensitivity of MDA8 and W126 to 75% reduction in BCs (Figure 2.4e-f). The TBG contributions over the western US are ~20-55 ppb (~30-70%) and up to >20 ppm-hours (>50%) for MDA8 and W126, respectively, with the maxima occurring over northwestern US and the Central Valley, respectively (Figure 2.4a;d).

Pfister et al. (2011b) concluded that 53±21% of CO over CA came from model boundary and ~1/4 of these (14±6%) had an Asian origin, for the same study period and region. Based on this relationship and the STEM-calculated TBG contributions, the upper limit of Asian contribution to MDA8 and W126 were ~5-14 ppb and <~5 ppm-hours, respectively. Since O₃ and CO have different lifetimes and sources, a more quantitative estimation of the Asian emissions contribution to O₃ will require sensitivity simulations in global models.

The contributions from TBG are compared to other contributors to background O₃, i.e. biomass burning and biogenic emissions (Figure 2.6). Compared to the broad impacts of TBG, the impacts of these two factors are much more limited to certain regions. Biomass burning contributes <15 ppb and 8 ppm-hours to MDA8 and W126, respectively, mainly over the

northern CA. Biogenic emissions have slight negative impacts over most regions in NV, ID, WA and OR, due to the NO_x sensitive regime. The strongest positive sensitivities occur over northern CA and the Central Valley, up to ~15 ppb and 6-8 ppm-hours for MDA8 and W126, respectively.

2.3.1.5 Impacts of US anthropogenic emissions and model resolution on surface O_3 sensitivities to BC O_3

The spatial distributions of the period-mean sensitivities of surface MDA8 and W126 to 50% reduction in BC O_3 are shown in Figure 2.7 for the western states. OR and WA show the lowest sensitivity $S1$ ($S1 = \text{base case-sensitivity case}$) for W126 but highest for MDA8, while broad regions in CA and NV show the highest sensitivity to W126 but lowest for MDA8. ID shows strong sensitivity of both MDA8 and W126 due to its high topography. The relative sensitivities $S2$ ($S2 = (\text{base case-sensitivity case}) / \text{base case}$) of MDA8 and W126 both show maxima over the northwestern US, where O_3 in the base case is much lower than over CA. The different features in W126 and MDA8 reflect the non-linear versus linear functions used in their calculations. The ratio of W126/MDA8 sensitivities can indicate regions where W126 levels are more sensitive to extra-regional sources than MDA8, and where monitoring data may be helpful for evaluating O_3 damage to vegetation. Regions of high $S1$ ratios (>0.6) appear over the Central Valley and southern CA where regional photochemical production is strong. The $S2$ ratios are overall higher than 1, with the higher values in NV, ID and OR (>3).

To evaluate the extent to which $S1$ of MDA8 and W126 are dependent on the magnitude of NA anthropogenic emissions, we conducted base and half BC O_3 forward sensitivity simulations in the 60 km/18 layer grid, with scaled US anthropogenic emissions. The NO_x , CO, and VOCs emissions were scaled based on the US emission trend from ~2000 to 2008 (<http://www.epa.gov/ttnchie1/trends/>). The changes in $S1$ of surface MDA8 and W126 in the scaled emission conditions are generally within ± 1.5 ppb and ppm-hours, respectively (Figure

2.8a-b). The urban regions in CA show lower SI for MDA8 but higher SI for W126, while the remaining areas show the opposite sign for the changes (due to different O_3 production regimes).

The impacts of US anthropogenic emissions on relative sensitivity $S2$ reach similar conclusions as those for SI (not shown).

2.3.1.6 Impacts of model vertical and horizontal resolution on surface O_3 sensitivities to BC O_3

To assess the impacts of vertical resolution on SI of MDA8 and W126, we conducted base and half BC O_3 simulations in 60 km/32 layer grid to compare with SI in the 60 km/18 layer grid. Adding vertical resolution reduces SI of MDA8 and W126 by up to ~10 ppb and 6 ppm-hours, respectively, and the largest reduction in SI for MDA8 and W126 occur over the OR/ID mountain areas and ID/NV grass+shrub/forest areas, respectively (Figure 2.8c-d). This indicates that the coarser vertical resolution can produce unrealistic meteorological conditions (boundary structure, wind fields, vertical mixing, etc) that can result in stronger net subsidence of airmasses to the surface.

The impacts of horizontal resolution were also assessed by comparing SI of surface MDA8 and W126 in the 60 km/32 layer and 12 km/32 layer grids (Figure 2.8e-f). The finer horizontal resolution produces sharper gradients, and SI of MDA8 in 12 km grid is generally higher by up to ~6 ppb. A few regions such as LA-San Diego, Seattle, Reno and the east ridge of the Central Valley show lower sensitivities, indicating differences at the local/urban scale that cannot be reflected in the coarse grid. The differences in W126 in the two grids range from -5 to ~3 ppm-hours, and the 12 km sensitivities are lower over NV, central and southern coast of CA, western OR and southern ID. In general the sensitivities to resolution are larger than those due to the US emission perturbations.

Again, the impacts of model grid resolution on relative sensitivity $S2$ reach similar conclusions as those for SI (not shown).

2.3.1.7 Importance of BC to predicted daily surface MDA8 O₃

Figure 2.9 presents the scatter plots of modeled daily MDA8 at all EPA AQS sites, colored by their sensitivities to half reduction in BC O₃. Regions A and B marked in both panels refer to “erroneously-predicted non-attainment areas” and “the actual non-attainment areas missed by the model”, respectively. More data points fall into Region A, indicating the overall over-prediction in O₃ as discussed in Section 2.3.1.1. It is shown in both 12 km/32L and 60 km/18L that BC affects the middle of the predicted O₃ distributions, and will be more important as the primary standard pushes down in future (the misclassification of non-attainment regions will more likely be due to the uncertainties in boundary conditions). These results are consistent with the findings by Koumoutsaris and Bey (2012) that emissions from distant sources do not affect significantly the O₃ trends at the high and low ends of the distribution. In contrast, emissions affect the high-predicted O₃ values and pushing down the primary standard exclude many of the locations in A that are very sensitive to the US emissions (not shown).

2.3.2 Connecting air mass aloft with surface O₃

The results in Section 2.3.1 show that TBG significantly affects western US surface O₃. To better understand the processes that link transported plumes to surface O₃, we studied in detail of O₃ at three sites (MBO, THD and South Coast (SC)) along the western US that span ~10° in latitude, and compared and contrasted how O₃ aloft at these sites impacted downwind surface O₃ concentrations.

2.3.2.1 Evaluation of model base simulation

Figure 2.10a compares the observed and modeled O₃ time series at MBO. Several high O₃ episodes were observed, with hourly maxima over 80 ppb. The model captures most of the observed variability, with major discrepancies at the beginning and at the end of the study period (18-20 June and 12-14 July), when predicted boundary layer heights (PBLH) were highest (not shown). Erroneously high mixed layer heights (Section 2.3.2.3.4), too strong downwind transport, and/or uncertainties in BCs are possible reasons for the overprediction. Statistics for all

simulations indicate better performance in the 12 km/32 layer grid (except correlation r due to more data): correlation r , mean bias, mean error, and RMSE are 0.37, 4.28 ppb, 10.67 ppb, 14.0 ppb, respectively, compared to the 60 km /18 layer simulations: 0.56, 9.44 ppb, 12.42 ppb, 14.50 ppb.

The THD sonde data were binned to the 32 model layers and compared with the model simulations (Figure 2.10c-e). The 12 km simulation captures much of the observed variability, including the strong episodes that occurred between 22-24 June (Huang et al., 2010a) and 5-7 July, as well as clean periods such as 2-4 July. In the lower free troposphere (~1.5-4 km ASL) mean O₃ levels ranged from <40 ppb to ~120 ppb and concentrations >40 ppb are observed 65%-80% of the time. Daily model performance statistics were calculated, and in general the r values were >0.5, RMSE were <20 ppb, and biases across all levels were <15 ppb. The model shows positive biases near the surface, consistent with the evaluations at the coastal AQS sites (Section 2.3.1.1), and in the upper troposphere, possibly due to the BCs. The 60 km simulation looks similar in terms of the general temporal variability, but overpredicts some periods (e.g., 28-29 June) due to the uncertainties in biomass burning emissions, and misplaced some vertical features (e.g., 9 July).

Modeled O₃ at a CARB surface monitoring site at SC, (i.e., LA North Main Street: 34.1°N, -118.27 °W, elevation 87 m, http://www.arb.ca.gov/qaweb/site.php?s_arb_code=70087) were also compared with the observations (Figure 2.10b). This location was chosen to characterize the eastern Pacific airmasses entering southern CA, and to study the impacts of these airmasses along with the local urban pollution on the downwind O₃ levels. The strong O₃ diurnal cycle indicates local O₃ production, and again the 12 km simulation better captures the temporal variability, with higher r values (0.61) than 60 km (0.25). The largest model discrepancies occur during ~26 June and ~10 July when the actual O₃ levels were low. The 60 km simulation shows ~20-30 ppb higher positive biases than 12 km, reflecting its incapability of capturing the nighttime minima due to the coarse meteorology and the smoothed/diluted NO_x emissions (in the coarse grid) over the urban area. The strong diurnal variations seldom modified

the simulated O₃ vertical structures above ~3 km. Elevated O₃ concentrations were predicted above 5-6 km around 24 June and 6-8 July, but they remained decoupled from the lower troposphere (not shown).

2.3.2.2 Source attribution from tracer results

The NO_x ages at MBO (2.7 km) and THD (2.5 km) ranged from 100 to 250 hours, and were correlated with each other during the Jun 22-24, and July 5-8 periods (Figure 2.11a), indicating that MBO and THD were influenced by the same synoptic flow conditions. The air masses were older at THD, reflecting the LRT pathways and the different extents of local contributions. In contrast, much younger NO_x ages at SC (1.5 km) from 10 to 50 hours indicate the strong local impacts.

Time series of regional source contributions based on CO tracers are shown in Figure 2.9b-d for THD, MBO and SC, respectively, at altitudes with strong coupling with downwind surface O₃ in Section 2.3.2.4. In the following discussions, BB and AN are short for biomass burning and anthropogenic tracers, respectively. Original anthropogenic tracers are regrouped for presentation: NA AN combines the US, Canada and Alaska tracer CO%, Asia AN includes China and other Asian nations tracer CO%, and Europe AN adds up the original Europe, Greenland and Russia tracer CO%.

Throughout the study period, airmasses at THD 2.5 km were frequently influenced by Asia AN and NAsia BB (on ~half of the days, their contributions > 30%), and five major NA fire events were identified, with contributions greater than 60% (Figure 2.11b). Contributions from other distant sources were much smaller but not negligible (e.g., European AN contributions were often greater than those from the NA AN). The time series plot at MBO (Figure 2.11c) shows high Asian AN and BB contributions (> 20%), and frequent strong contributions (> 20%) from NA BB. NA AN sources contributed on average 15%, with maximum contributions in excess of 20%. The situation at SC 1.5 km (Figure 2.11d) significantly differed from those at THD and MBO, dominated by the NA AN emissions, with periods that local fires also

contributing significantly, such as late June, 2-5 July, and after 8 July. The monthly mean tracer CO contributions at these locations were also calculated. THD (2.5 km) was mostly affected by NA BB (38.8%), followed by NAsia BB (24.95%) and Asia AN (23.1%) sources. MBO (2.7 km) was also mainly influenced by these three sources, with NAsia BB the leading contributor (29.2%). NA BB and Asian AN contributions were 24.7% and 24.1%, respectively. SC (1.5 km) was also influenced by NA BB sources (18.8%), but the dominating contributor was the NA AN sources (59.5%).

We explored the relationships between these CO tracers and the modeled daytime mean O₃ concentrations at these sites. The mean modeled O₃ concentrations at THD 2.5 km, MBO surface and SC 1.5 km are 57.6 ppb, 52.1 ppb and 72 ppb, with high O₃ values (i.e., >75th percentile) at 66.4 ppb, 55.9 ppb, and 84.2 ppb, respectively. At THD, the high O₃ values (>75th percentile) occurred under conditions with maximum influences from NA BB. In contrast, at MBO the highest values occurred when NAsia BB and Asia AN had maximum influence, while at SC the highest values occurred when NA AN sources showed the highest contributions. Ambrose et al. (2011) analyzed 2004-2009 O₃ data at MBO on high O₃ days, defined as 8-hour averages greater than 70 ppb. The 8-hour averages were 86 ppb and 76 ppb on 7 July and 8 July, respectively, and they concluded that these high O₃ periods were categorized as mixed Asian pollution and UT/LS air, which is consistent with our results.

The correlation r between NO_x age and the extra-regional CO % (sum of non-US anthropogenic + biomass burning tracer CO%) were also analyzed. At THD and MBO, extra-regional CO% was highly correlated with NO_x age (0.91 and 0.76, respectively). At SC, these two parameters were not as well correlated (0.37), indicating the strong impacts of local emissions and complicated flow patterns in this region.

2.3.2.3 O₃ sensitivities to BC and emissions

The time series of O₃ sensitivities (SI) to: 1) half reductions in BC O₃ in three model resolutions; 2) to the scaled US anthropogenic emissions; and 3) to zeroing out biomass burning

and biogenic emissions (2) and 3) used the 60 km/18 layer grid) are shown at MBO 2.7 km, THD 2.5 km and SC surface/lowest level (Figure 2.12). Ozone levels at these altitudes are highly connected with downwind surface O₃ levels as indicated in Section 2.3.2.4. Ozone sensitivities to BC O₃ at THD and MBO show similar temporal variability and magnitude (10-40 ppb, with correlations of 0.6-0.8 depending on resolution), indicating that they are influenced by similar sources/synoptic flow conditions during this period. This supports the findings by Zhang et al. (2009) for spring 2006 when they found that both sites were affected by northern China emissions. The BCs correctly reflect the major LRT episodes during 22-24 June and 5-7 July, resulting in good model performance at THD and MBO during these periods. The uncertainty in the BCs is the major reason causing the O₃ overprediction at both locations during 18-20 June and after 12 July. An additional high O₃ period (30 June-4 July) at MBO (above the period mean level as shown by the thin red horizontal line) is shown to be affected by the US anthropogenic and biomass burning emissions. Impacts of biogenic emissions are overall slightly negative due to the NO_x sensitive conditions. THD O₃ at 2.5 km was intensively affected by northern CA wildfires, which led to O₃ enhancements during ~29-30 June and ~10 July (as indicated from the high sensitivity (up to >50 ppb) to biomass burning emissions). Uncertainties in fire/biogenic emissions possibly caused the overprediction in O₃ from the surface to ~4 km (Figure 2.10e). The impacts of BC O₃ at SC show much lower magnitude due to the lower altitude, with a similar diurnal cycle as the total O₃ concentrations. SC O₃ is less strongly affected by biomass burning during this period than the other two locations, and the varied sensitivities to US anthropogenic emissions indicate the different photochemical regimes and meteorological conditions. The high positive sensitivities to anthropogenic and biogenic emissions after 10 July possibly caused the overprediction in O₃ for this period.

2.3.2.4 Connection of surface O₃ and O₃ aloft at previous times

2.3.3.4.1 Trajectories, the “*Impacting Probability*” metric, and time-lag correlations

The pathways of descending airmasses from MBO 2.7 km, THD 2.5 km and SC 1.5 km (~top of the PBL, based on measurements of daily maximum PBLH at Pasadena in spring 2010 ranged from ~600-1800 m, Newman et al., 2012) were studied by two-day forward trajectories (calculated hourly) based on the 12 km WRF meteorology. The trajectories originating from MBO at all night times (to minimize the local contributions and to study the influences of free troposphere air which typically has higher O₃ concentrations) during the 29-day period were calculated, together with the forward trajectories originating from THD 2.5 km and SC 1.5 km at all day times during the studied period. Daytime trajectories were chosen because of the higher O₃ and the dominance of on-shore flows during the daytime (Figure 2.13). Most of the trajectories from THD travel towards CA, ID, OR and NV at altitudes below ~1.5 km, whereas trajectories from SC travel towards the southern CA air basin, southern NV and Mexico at ~0.5-1 km. Airmasses from MBO impacted OR, WA, ID and northern CA at 0.5-2 km.

To quantify the likelihood of transported air mixing with local air pollution, the entrainment *Impacting Probability (IP)* metric for transported air, defined in equation (2.11), were calculated:

$$IP \text{ (dimensionless)} = \frac{\text{(number of trajectory points at a specific time lower than local PBLH)}}{\text{(number of all trajectory points at the same time)}} \quad (2.11)$$

The *IP* metric is an indicator of how often the entrainment of transported airmasses occurs at a specific time, and was calculated at all local day times (Table 2.8). The MBO and THD airmasses show the highest chance to be entrained into the PBL in the early afternoon (i.e., *IP*=0.34 and 0.66, respectively, at ~3 pm PDT), when the PBL is deep and well-mixed over most regions. The overall higher magnitude of *IP* for MBO than those for THD indicates the effect of downwind impacted regions' topography (i.e., most impacted regions downwind of MBO have

higher topography). The IP values for SC 1.5 km airmasses demonstrate a flatter shape than those for THD and MBO, are greater than 0.5 from 9 am to 4 pm. This reflects that on-shore winds and the boundary layer growth quickly connect 1.5 km airmasses above SC with the surface regions.

To further analyze the impact of the airmasses at elevated locations on inland surface O_3 , we correlated modeled daily daytime O_3 time series, at 2.5 km at THD and 1.5 km at SC with modeled surface daily daytime O_3 time series using no time offset, one-day and two-day offsets, referred to as "same-day", "one-day" and "two-day" cases, respectively. A similar methodology was applied between THD and the northern Sacramento Valley monitoring site at Tuscan Butte by Huang et al. (2010a). As correlations do not have directions, they were filtered by all daytime-departing trajectories from THD and SC. Only the correlations over terrestrial regions are shown. The correlations calculated with no time offset help identify regions that are mainly affected by changing synoptic conditions, or fast transport. Regions with high "same-day" correlations (>0.6) with THD O_3 extended ~ 100 - 200 km inland (not shown). High "one-day" correlation regions cover a wide region over northern CA and western OR (Figure 2.13d), showing the scale of the transport processes during this period. The "two-day" correlations were generally lower, with the maxima in the Central Valley (0.5-0.6) (not shown). In contrast, SC 1.5 km daytime O_3 shows strong correlations with same-day O_3 (> 0.8), and the regions with high correlations covered large portion of southern CA (Figure 2.13e). This reflects the faster transport speed over these areas, and will be discussed in more detail in the adjoint sensitivity analysis (Section 2.3.2.4.3). The regions with high "one-day" correlations extended further inland and reach NV with lower magnitudes, and the "two-day" correlations dropped below 0.5. Correlations were calculated between modeled nighttime O_3 at MBO and the modeled daytime O_3 at the surface, and they were filtered by the nighttime forward trajectories originating from MBO. Nighttime O_3 at MBO was highly correlated with the "same-day" daytime surface O_3 at surrounding areas out to hundreds of km (Figure 2.13f). The area impacted reflects the growth in the daytime boundary layer height and the nighttime down slope flows. The "one-day" high

correlations (>0.6) covered vast areas of eastern OR and western ID, reflecting the predominant westerly flows. "Second-day" correlations dropped below 0.5 (not shown).

2.3.2.4.2 Adjoint sensitivity analysis: areas of influence

We calculated adjoint sensitivities to surface O_3 at receptor regions to further explore the impacts of transport/subsidence of airmasses on surface O_3 . The STEM adjoint sensitivity analysis has demonstrated advantages over trajectory analysis and correlation-based analysis in previous studies (e.g., Huang et al., 2010a, b and Section 2.3.2.4.3) in that it includes horizontal transport, vertical mixing and chemistry processes in the calculations (Sandu et al., 2005). The selected northwestern US receptor (NWR) (4250 grids) and the southern CA receptor (SCR) (1200 grids) (areas in the blue line boxes in Figure 2.14a-b) were shown to be affected by the transported airmasses over THD, MBO or SC in the trajectory and correlation analyses (Huang et al., 2010b). The O_3 adjoint sensitivities ($\lambda[O_3]$) were calculated 49 hours backward in time from 00 UTC of each day, and the areas of influence for each case were averaged to produce the monthly mean areas of influence with 49 time steps, which are used for discussions below.

Figure 2.14a-b show the vertically-integrated $\lambda[O_3]$ averaged over the previous day daytimes calculated on the 12 km grid. They show the locations that have the biggest impact on next day surface O_3 at NWR and SCR regions, respectively. Surface O_3 in the NWR at 00 UTC is sensitive to previous day O_3 concentrations over a large geographical region that extends over hundreds of kilometers (Figure 2.14a). The western extent of the influence area helps identify the multiple transport pathways that bring eastern Pacific air masses into this region, which are controlled by the moving Pacific-high pressure systems from June to July. Surface O_3 over southern CA is shown to be sensitive to O_3 in the Central Valley, and the near-shore areas along the central and south coast on the previous daytime, which indicates the impacts of inter-basin transport and sea breezes (Figure 2.14b). Returning airmasses from NV to the northern Central Valley in the previous daytime also impact southern CA in the following day.

Similar adjoint sensitivity analysis was also done on the 60 km grids. The results are qualitatively similar, but are much smoother than those for the 12 km analysis (Figure 2.15a-b).

2.3.2.4.3 Adjoint sensitivity analysis: Surface O₃ sensitivity to O₃ at sampling locations at earlier times

To connect the results from forward trajectory analysis and previous correlation analysis conducted for the THD, MBO and SC locations, we plot the time-height curtain of adjoint sensitivities at these sites (i.e., surface O₃ sensitivity to O₃ at these sites through time) based on 12 km results, normalized by the number of receptor grids. Figure 2.14c-d illustrates the temporal evolution of $\lambda[\text{O}_3]$ at MBO and THD with respect to the NWR surface O₃ at final time. Two hotspots are found in the MBO plot (Figure 2.14c): within the boundary layer 1-5 hours before the final time; and in the free troposphere 10-15 hours backwards in time. The THD plot (Figure 2.14d) also shows two hotspots: within the boundary layer during the first 1-5 hours; and 1.5-2.5 km in free troposphere 25-30 hours backwards in time. These results indicate that surface O₃ at NWR is not only affected by local production (close to the final time) but also by O₃ in the free troposphere at MBO and THD.

The temporal evolution of $\lambda[\text{O}_3]$ at SC for SCR is shown in Figure 2.14e. The gradients at SC are strongest in the first 10 hours before the final time, extend out to 30 hours before, and are highest below 2 km ASL. These results indicate that the transport of O₃ at SC to the SCR surface involve transport above the nocturnal and marine boundary layers and subsequent entrainment into the daytime boundary layer. The transport most strongly affects O₃ over downwind areas in the next 1-2 days. Ozone in the free troposphere over THD also influences the surface O₃ levels at SCR (Figure 2.14f) with a much weaker intensity (the scale $\times 5$). The maximum sensitivities are found 30-40 hours backward in time at 1-2 km ASL, the height at which the plumes enter northern CA, move through the Central Valley, and reach the surface SCR. Again these results are consistent with the trajectory analysis.

Adjoint sensitivities in the 60 km/18 layer grid cannot represent these processes as clearly as in the 12 km grid (Figure 2.15c-f).

2.3.2.4.4 Uncertainty

The analysis in Section 2.3.2.4 can be highly affected by the WRF-predicted PBLH. We compared the predicted PBLH on a single day (June 20) resulting from various WRF PBL schemes, which is a key factor that determines the predicted PBLH. Similar as findings by Saide et al. (2011) over Santiago, Chile, overall MYNN3 and QNSE schemes generate the shallowest and deepest PBLH, respectively, and the differences between YSU and MYJ schemes vary by region. The WRF version also affects predicted PBLH (Figure 2.16). Extending these comparisons to a longer period with careful evaluation (which would benefit from denser/more frequent PBLH observations) and exploring the relationship between meteorological conditions and pollutants are important future directions.

2.3.3 Case study: DA during a LRT episode

Results from Sections 2.3.1 and 2.3.2 show that elevated pollution levels over the eastern Pacific at mid-altitudes (2-5 km) can be transported inland and entrained into the PBL during summertime. Therefore, improving modeled O_3 concentrations over the eastern Pacific can reduce uncertainties in modeled surface pollution levels over the western US. In this section we explore how well existing O_3 observations can constrain modeled surface O_3 concentrations using the DA technique. Since model resolution is critical for reflecting the subsidence processes (Section 2.3.1.6), all DA cases shown here were performed in the 12 km/32 layer grid.

We selected 5-7 July as a representative LRT episode for the case study, during which time the northwestern US began to be impacted by extra-regional emissions. As indicated in Figures 2.9-2.10, the LRT plumes started to influence O_3 levels at THD 2.5 km and MBO 2.7 km on 5-6 July. Twelve-day back-trajectories (Figure 2.17a) based on the 60 km WRF meteorology from these two locations at 18 UTC on 6 July are colored by travelling heights (in km, AGL), and they show similar transport pathways. About eleven days before the airmasses were over the

Arctic (80°N over Canada) at 9-10 km. Then they were transported over Siberia (where the wildfires occurred as indicated by the overlaid RAQMS fire emissions in grey color scale at 00 UTC on 1 July) in the upper troposphere, descended into the mid-troposphere over northeast Asia and across the Pacific, while continuing to descend, and finally reached the western US.

The transport of pollutants during this period was observed by TES. In Figure 2.17b-d, we matched the TES-observed CO total column and tropospheric O₃ column during the trans-Pacific transport period. Strongly enhanced CO columns (up to $5-6 \times 10^{18}$ molecules/cm²) were observed on 30 June near the fire sources in northeastern Asia. Enhanced O₃ tropospheric columns (up to 60-70 DU) were seen during 2-4 July in the middle of Pacific spanning 40-50°N. After ~5-7 days of transport from the fire events in Russia, O₃ column enhancements were seen over the western US (4-6 July, up to 60-70 DU).

To discuss the impacts of this event on inland air quality, Figure 2.17e-f show the 12 km WRF-predicted flow fields (overlaid on WRF-predicted color-shaded surface level pressure (SLP)) on 5 July and 6 July, 18 UTC at ~2.5-3 km AGL. On 5 July, winds are mostly westerly, directly bringing the offshore pollution inland. On the following day, the winds shifted towards the south and the on-shore winds affected northern CA.

2.3.4.1 Discrepancies between model *a priori* results and OMI/TES retrievals

At ~22 UTC, 5 July, Aura overpassed the eastern Pacific when the TES special observations and OMI measurements were made (Figure 2.18a). The model *a priori* (without assimilation) at this time are compared with the selected (criteria of selecting TES and OMI data for DA is described in Table 2.4) satellite retrievals in the DA domain (a subset of the 12 km/32 layer grid covering WA, OR and northern CA, Figure 2.18a). The *a priori* with satellite observation operators agrees fairly well with the satellite retrievals, and is overall underpredicted compared to OMI, over a wide area of the eastern Pacific north of 42°N. Compared to TES, the *a priori* overpredicts O₃ in the upper troposphere and underpredicts in the lower/mid-troposphere.

The highest negative biases occur at 500-900 hPa (~1-5 km) south of 44°N. Note that the discrepancies between satellite and model are determined by both model performance and the retrieval method/quality.

To discuss how the model biases (with respect to the satellite retrievals) over the eastern Pacific might impact surface O₃ over the NWR region (defined in Section 2.3.2.4.2), we plot the adjoint sensitivities $\lambda[\text{O}_3]$ along the TES and OMI sampling locations at the Aura overpass time (Figure 2.19a;c). These sensitivities show that surface O₃ over the NWR region ~30 hours after the Aura overpass time (00 UTC, July 7) was most sensitive to the O₃ concentrations at ~2-4 km at TES and OMI sampling locations. The magnitudes of $\lambda[\text{O}_3]$ at the OMI sampling locations are overall higher than those at TES, possible due to the wider horizontal coverage of samples and wind fields. These findings are different from the conclusions by Zoogman et al. (2011) over the urban regions, where the local production dominates and the O₃ production efficiency is most sensitive to boundary layer O₃. The two-day forward trajectories originating at the Aura overpass time from TES sampling locations at 4 km (colored by traveling heights) demonstrate that airmasses originating south of 44°N, where highest discrepancies between the model *a priori* and TES retrievals occur, rarely reached inland areas. In contrast, the two-day forward trajectories originating at the same time from OMI sampling locations at 2 km impacted broad inland areas.

Similar analyses were conducted at THD (Figure 2.19e-f), which indicates that airmasses at ~2-6 km at the time of the sonde (~19 UTC on 5 July) had strongest impacts on O₃ over downwind inland areas in northern Central Valley on the following day, and the maximum $\lambda[\text{O}_3]$ is close to the magnitude of the one-month mean (Figure 2.14d, hot spot at ~30 hours before the final time).

2.3.4.2 Data assimilation results

2.3.4.2.1 Assimilation impacts at surface

Figure 2.20a-b show the mean values of modeled daytime mean surface O₃ during the 30-hour assimilation window, before and after assimilating only the available site (AQS, CASTNET

and MBO) observations (*Case AS*). A 54-hour assimilation window (ending at 00 UTC on July 8) was also tested but did not show significant differences for the first 30 hours from *Case AS*. The AQS observations were assimilated from the model surface level, while CASTNET and MBO (located at higher altitudes) observations were assimilated from the model layer(s) that matched their actual altitudes. These observations are overlaid on the plots, most of which are located in northern CA. The *a priori* generally captures the observed O₃ magnitudes over WA and OR, and underestimates O₃ over most northern CA regions, where active biomass burning occurred during this time. In another case, we assimilated the available surface AQS NO₂ measurements and controlled NO_x emissions by using a 24-hour assimilation window (method details are described in Chai et al., 2009). Largest adjustment in NO_x emissions occurred in northern CA, reflecting the high uncertainties in biomass burning emissions (Figure 2.20d-e). After assimilating surface observations, surface O₃ over northern CA increases substantially (mostly by 5-10 ppb, but up to 10-20 ppb, Figure 2.20c). Table 2.9 shows that errors ($error = |modeled - observed|$) at these observational sites are overall reduced after the assimilation, with highest improvement over northern CA due to the largest discrepancies of the *a priori* and the dense number of observations..

Figure 2.21a-c show the differences of mean daytime surface O₃ before and after assimilating vertical profiles from TES (*Case AT*), OMI (*Case AO*) and the THD sonde (*Case AD*), respectively. Figure 2.21d-f compare the O₃ differences between *Cases AT, AO* and *AD*. The effects of assimilating vertical profiles changes mean daytime surface O₃ by $< \pm 0.5$ ppb, and the major differences occur over WA and OR, as well as near the sampling locations. The errors for daytime mean O₃ at the available surface sites were overall very slightly reduced (less than 0.2 ppb, Table 2.9). The limited changes in surface O₃ compared to those in *Case AS* reflect the lack of spatiotemporal resolution for the assimilated vertical profiles.

We also assimilated surface observations and vertical profiles together (*Cases AST, ASO* and *ASD* for adding TES, OMI, and THD sonde, respectively). The differences of mean daytime surface O₃ between these cases and *Case AS* reflect the effects of adding O₃ vertical profiles into

the assimilation. Results are shown in Figure 2.22a-c, respectively, and Figure 2.24d-f further compare the differences between these three assimilation cases. Mean daytime surface O₃ over WA and OR increase slightly due to the underestimated O₃ in mid-altitude offshore, and drop by up to 2-3 ppb in northern CA, different from the features shown in Figure 2.21. The changes in errors after adding vertical profiles are within $\sim\pm 2$ ppb and are overall positive (Table 2.9), indicating the competing/conflicting effects of assimilating the observations taken from different platforms/regions that may be due to retrieval uncertainties and model vertical structure (Section 2.3.3.2.3).

2.3.4.2.2 Assimilating impacts in the vertical

To demonstrate how assimilating different observations modified the O₃ vertical distributions, we plotted the O₃ changes (assimilation case-the *a priori*) at the TES (Figure 2.23), OMI (Figure 2.24a-d) sampling locations and at THD (Figure 2.24e-f) for *Cases AS, AT, AO, and AD*. These compare the consistency in the information provided by these observations.

At the TES sampling locations (Figure 2.23a;c;e;g, raw data: before applying the observation operator), assimilations of all types of observations result in modification of O₃ in the similar location in the mid troposphere (i.e., ~ 500 -700 hPa), mostly south of 44°N, where the highest biases in the *a priori* occur. *Cases AT, AS* and *AD* result in similar spatial distributions of the O₃ changes, and *Case AT* shows the biggest changes (-20 to >40 ppb), while *Case AO* results in approximately the opposite changes. After applying the TES observation operator (Figure 2.23b;d;f;h), the changes between all four cases and the *a priori* were smoothed (showing decreased magnitudes and extended affected regions as high as to the upper troposphere).

At the OMI sampling locations, assimilating different types of observations all modify the O₃ raw data (Figure 2.24a-d black dots) at most altitudes, and *Case AO* shows the biggest changes (-20 to 50 ppb), followed by *Case AS* (-10 to 40 ppb). *Cases AS, AT* and *AD* result in overall negative changes while *Case AO* caused positive changes. Together with Figure 2.23, these indicate a possible high positive bias in OMI measurements. After applying the OMI

observation operator (Figure 2.24a-d red dots), again the changes between all assimilation cases and the *a priori* were smoothed. *Cases AS, AT and AD* result in overall negative changes while *Case AO* caused positive changes.

Figure 2.24e-f present the O₃ vertical distributions at THD from sonde, the *a priori* and the assimilation cases. The model *a priori* overestimates O₃ <2 km and >10 km, and underestimates O₃ at 2-3 km. *Case AD* generates best results, especially the variability at ~2-3 km and >10 km (Figure 2.24e). Assimilating surface measurements modifies O₃ structure <2 km, and O₃ increases at ~2-4 km by up to 15 ppb, but fails to capture the sharp variability. The changes made by assimilating TES and OMI measurements at THD are much smaller (<1 ppb), mainly occurring at ~2-4 km and 6-10 km for TES and OMI, respectively.

2.3.4.2.3 Estimation of uncertainties in the satellite retrievals

We determine the upper limits of satellite retrievals by the discrepancies between retrievals and the assimilated fields of *Case AS* (Figure 2.25). This estimate is based on the assumption that assimilated fields in this case provide the “best” O₃ distributions at lower/mid-troposphere over the domain. TES shows 5-20% positive biases at 500-900 hpa (the region that surface layer O₃ is sensitive to at the overpass time), and OMI has a 5-10% higher bias than TES. This estimation is consistent with conclusions in previous validation studies, but the method needs to be further tested for extended regions and periods.

Discrepancies between THD sonde and assimilated O₃ at THD in *Case AS* are much varied, due to much higher vertical resolution and accuracy of sonde. *Case AS* is not able to correct the detailed vertical variability due to the coarser model vertical structure.

2.4 Conclusions and suggestions on future work

The western US was strongly and extensively affected by TBG during this summer period. Ozone contributed most among the TBG pollutants, and PAN was the most important species among precursors. The impacts of TBG differed among various geographical regions and land types, and stratospheric O₃ had weak impacts on surface O₃ during this time. W126 showed

stronger and higher non-linear responses to perturbations in TBG than MDA8. The TBG impacts show weak dependence on US anthropogenic emissions. The impacts of TBG on surface O₃ were strongly affected by model vertical/horizontal resolution.

At MBO and THD, O₃ was mostly affected by TBG pollutants, under the control of similar synoptic conditions during this period, and was occasionally affected by US emissions. SC O₃ was strongly affected by local emissions. The *IP* metric showed that the probabilities of airmasses originating from THD and MBO impacting downwind surface air quality reached daily maxima of 34% and 66% at 3pm PDT, respectively, and those from SC stayed >50% during 9am-4pm. Correlations of O₃ at these locations with terrestrial surface O₃ with different time offsets are moderate (>0.6) to strong (>0.8) for 1-2 days and cover large downwind areas. Receptor-based adjoint sensitivity analysis further highlighted the transport/subsidence processes (e.g., transport time and altitudes) that link airmasses aloft with the surface.

A case study demonstrated that assimilating surface *in-situ* observations was successful in constraining modeled O₃ spatial distributions in regions where these measurements are dense (i.e., reducing the model error by >5 ppb in average). Satellite products provide information for identifying LRT episodes, but in this case the inclusion of existing O₃ vertical profiles in DA did not efficiently improve the O₃ distributions except the locations near the sampling locations. Assimilating current satellite observations alone may be more efficient in a global model (e.g., Singh et al., 2011; Parrington et al., 2009) by using a longer assimilation period that allows for including more measurements. Assimilating surface observations and vertical profiles may cause conflicts, which can be used to estimate the uncertainties in the satellite retrievals.

Suggestions on future work include:

- 1) A quantitative source attribution requires the use of global models, but the improvement on model predictability and the investigation of the import/export budgets can benefit from nesting with high resolution regional models at the sources/receptors, as well as a better understanding of the distributions of O₃ and its precursors at the regional model boundary.

2) Due to the non-linear function used in calculating W126 and the resulting differences from MDA8 and the higher weights for high O₃ concentrations, continuous efforts on analyzing various contributors to W126 levels and additional observations in regions over different types of vegetations would be helpful for determining the secondary standard and assessing O₃ impacts on ecosystems.

3) To better understand model-based transport/subsidence processes and improve DA efficiency, making denser and routinely measurements for key meteorological variables such as PBLH and other types of O₃ vertical profiles (such as extended ozonesonde network and measurements taken on commercial airlines) are encouraged. Efforts should also focus on exploring the appropriate resolution (and other needs) and retrieval quality for the planned geostationary missions (such as GEO-CAPE over the US) in ~10 years. Finally, it is valuable to continue exploring the reasons for the conflicting effects that occur when assimilating different observations together for improving DA efficiency, evaluating model configurations and estimating quality of the observations.

Table 2.1 Wildfire plumes characteristics from the MISR plume height project

Region	Year	Number of plumes w/ power estimates	Total radiative of power (MW)	Median value of plume top heights (m ASL)	Radiative power/plume (MW)
Siberia	2002	541	269422	1367	498.01
	2003	985	474288	2225	481.51
	2006	433	148157	1597	342.16
	2008	1451	574766	1652	396.12
Canada (end of May-July)	2008	72	92439	2062	1283.9
NA	2002	445	371717	1815	835.32
	2004	1137	501585	1743	441.15
	2005	912	376329	1415	412.64
	2006	439	253488	2191	577.42
	2007	510	237497	1620	465.68

Source: <http://misr.jpl.nasa.gov/getData/accessData/MisrMinxPlumes/>

Table 2.2 Descriptions of observational datasets used in this study

Observational data	Location	Duration	Spatiotemporal resolution	Method
Ground O ₃ ^a	U.S. EPA AQS sites in CA, NV, OR, WA, and ID	16 June-14 July	1 hour	Multiple methods including: UV; UV absorption; UV radiation absorption; UV 2B Model 202
Ground O ₃ ^b	Eight CASTNET sites in CA, NV, OR, WA, and ID	16 June-14 July	1 hour	UV absorbance
Site O ₃	MBO (44°N, -121.7°W, ~2.7 km ASL)	16 June-14 July	1 hour	Ultraviolet (UV) Photometric Ozone Analyzer
O ₃ sondes ^c	THD (40.8°N, -124.2°W, ~20 m ASL)	20 June – 12 July	mostly ~19 UTC, 20 days	Electrochemical detection methods through the reaction of O ₃ in an aqueous potassium iodide solution in an electrochemical cell
DC-8 CO ^d	Eastern Pacific	18-24 June	1 minute (DC-8 speed: ~14 km/min)	Diode laser spectrometer
DC-8 O ₃ & NO _y ^{d,e}				NCAR 4-channel chemiluminescence instrument
DC-8 PAN ^d				CIMS Instrument by Georgia Tech and NCAR
Total O ₃ columns (required by the TUV module) ^f	Model domain wide	16 June-14 July	Daily, 1°×1°	Observes Earth's backscattered radiation (in the UV)
OMI Level 2 O ₃ profiles, V003 ^g	Eastern Pacific and western US	5 July	Daily	

Table 2.2 Continued

TES Level 3 tropospheric O ₃ columns and CO columns ^h	Northern Hemisphere	30 June & 2, 4, 6 July	Every other day, 2°×4°	Measures the infrared-light energy (radiance) emitted by Earth's surface and by gases and particles in Earth's atmosphere (in the infrared)
TES Level 2 special observation nadir O ₃ profiles, V004 ^h	Eastern Pacific (150-120°W, 30-60°N)	16 June-14 July	See sampling density plot in Figure 2.1i	
MODIS (Terra, MOD06_L2) Level 2 cloud product ⁱ	Eastern Pacific	5 July	Several times each day, we use the one at ~20 UTC	Combines infrared and visible techniques to determine cloud physical and radiative properties
MODIS-detected point fire information ^j	Model domain wide	16 June-14 July	Several times each day, 1 km	Multi-spectral detection of fire locations

^a <http://www.epa.gov/ttn/airs/airsaqs/detaildata/downloadaqsdata.htm>

^b http://java.epa.gov/castnet/epa_jsp/prepackageddata.jsp#ozone

^c <ftp://ftp.cmdl.noaa.gov/ozwv/ozone/>

^d ftp://ftp-air.larc.nasa.gov/pub/ARCTAS/DC8_AIRCRAFT/

^e <http://www.espo.nasa.gov/arctas/docs/instruments/NOxyO3.pdf>

^f <ftp://toms.gsfc.nasa.gov/pub/omi/data/ozone/Y2008/>

^g http://disc.sci.gsfc.nasa.gov/Aura/data-holdings/OMI/omo3pr_v003.shtml

^h http://eosweb.larc.nasa.gov/PRODOCS/tes/table_tes.html

ⁱ <http://ladsweb.nascom.nasa.gov/data/search.html>

^j <http://firefly.geog.umd.edu/download/>

Abbreviations: AQS: Air Quality System; ASL: Above Sea Level; CASTNET: The Clean Air Status and Trends Network; CIMS: Chemical Ionization Mass Spectrometer; EPA: Environmental Protection Agency; MODIS: Moderate Resolution Imaging Spectroradiometer; NCAR: National Center for Atmospheric Research; OMI: Ozone Monitoring Instrument; TES: Tropospheric Emission Spectrometer; TUV: Tropospheric Ultraviolet-Visible radiation model; UV: Ultraviolet

Table 2.3 Descriptions of STEM full-chemistry base and forward/adjoint sensitivity simulations ^a

Cases		Descriptions of model inputs and perturbations
F0	Base 12 km (12 km×12 km, 1 hour, 32 layers in troposphere)	CARB anthropogenic and biogenic emissions+ MODIS/prep-chem-source fire emissions, WRF meteorology, TBCs and LBCs from the C0 (base 60 km) results
F1	12 km 50% BC O ₃	TBCs and LBCs from the C3 (60 km 50% BC O ₃) results
FA1/FA2	Adjoint 12 km, NWR/ SCR Case	Northern California and Oregon/ Southern California as receptors, control surface O ₃ at 00 UTC; simulation window for each day is 49 hours.
C0	Base 60 km (60 km×60 km, 6 hours, 18 layers in troposphere)	NEI 2001 anthropogenic/Orchidee biogenic emissions+RAQMS fire emissions, WRF meteorology, RAQMS and 60 km tracer results (D'Allura et al., 2011) as gases/aerosol boundary conditions.
C1	60 km half TBC O ₃	TBC O ₃ reduced by 50% at each time step
C2/C3/C4	60 km 25%, 50% and 75% BC O ₃	TBC and LBC O ₃ reduced by 75%, 50% and 25% at each time step
C5/C6/C7	60 km 25%, 50% and 75% BCs multiple species ^b	TBCs and LBCs for multiple species reduced by 75%, 50% and 25% at each time step
C8/C9	60 km 50% and 75% BC PAN	TBC and LBC PAN reduced by 50% and 25% at each time step
C10/C11	60 km PAN composition/ composition+decomposition off	Reaction(s) of PAN composition/composition+decomposition are blocked
CA1/CA2	Adjoint 60 km, NWR/SCR Case	Northern California and Oregon/ Southern California as receptors, control surface O ₃ at 00 UTC; simulation window for each day is 49 hours.
CL0	Base 60 km (32 layers)	Same as C0, but using 32 vertical layers.
CL1	60 km 50% BC O ₃ (32 layers)	Same as C3, but using 32 vertical layers.
CR0	Base 60 km w/ reduced emissions	Same as C0, but reduced anthropogenic CO, NO _x and VOCs emissions based on EPA emission trend.
CR1	60 km 50% BC O ₃ w/ reduced emissions	Same as C3, but reduced anthropogenic CO, NO _x and VOCs emissions based on EPA emission trend.

Table 2.3 Continued

CBB	Base 60 km w/o biomass burning emissions	Same as C0, but not including the biomass burning emissions
CBG	Base 60 km w/o biogenic emissions	Same as C0, but not including the biogenic emissions

^aThe studied period for each simulation case was 16 June-14 July, 2008.

^bMultiple species in cases C5-C7 refer to the shared gaseous species in TBCs/LBCs except O₃, including: CO, NO, NO₂, NO₃, HNO₃, HNO₄, PAN, N₂O₅.

Abbreviations: CARB: California Air Resource Board; NEI: National Emission Inventory; PAN: Peroxyacetyl nitrate; RAQMS: Real-time Air Quality Modeling System; TBCs/LBCs: Top/Lateral Boundary Conditions; WRF: Weather Research and Forecasting Model

Table 2.4 Descriptions of 4-d var data assimilation cases in the 12 km model grid ^a

Cases		Descriptions	Observation error (s)
AS	Assimilate observations from AQS, CASTNET and MBO sites	Assimilate available observations at all times in the assimilation window. CASTNET and MBO observations were assimilated at actual altitudes. AQS observations were assimilated from the surface level.	constant 3.0 ppb: maximum representative error (defined by Chai et al., 2007) in each grid & ~10% of mean observations in the window
AT	Assimilate O ₃ vertical profiles from TES special observations	TES special observations were assimilated at Aura overpass time (~22 UTC, 5 July). Only the observations with quality flag=1 and cloud optical depth<=2.0 were used.	constant 6.0 ppb for TES (~7% of mean 84 ppb): Nassar et al., 2008, and Boxe et al., 2010
AO	Assimilate OMI O ₃ vertical profiles	OMI observations were assimilated at Aura overpass time (~22 UTC, 5 July). Only the observations at places where MODIS cloud fraction=0 were used (suggested by Russell et al., 2011).	constant 11.0 ppb for OMI: 10% of mean 110 ppb
AD	Assimilate THD O ₃ sonde	O ₃ sondes at THD were binned into model levels and assimilated at the launch time (~19 UTC, 5 July).	constant 5.0 ppb: ~10% (Thompson et al., 2010; Liu et al., 2009) of mean observations at all levels in troposphere
AST	Assimilate site & TES O ₃	Combination of cases AS and AT	
ASO	Assimilate site & OMI O ₃	Combination of cases AS and AO	
ASD	Assimilate site & THD sonde O ₃	Combination of cases AS and AD	

^a All cases used the same background error correlation matrix calculated by the NMC method as introduced by Chai et al. (2007). Assimilation window was 18 UTC, 5 July-00 UTC, 7 July, 2008 (30 hours).

Table 2.5 Statistics for observed and modeled surface O₃ metrics at EPA AQS sites as shown in Figure 2.2 (better performance in bold). Model results were extracted at surface by using linear interpolation method.

Statistics	MDA8			W126 MI		
	Observation	60km/18L	12km/32L	Observation	60km/18L	12km/32L
Mean (ppb)	57.57	74.16	69.39	6.36	13.83	11.14
Standard Deviation (ppb)	16.80	7.76	10.29	5.65	4.15	4.90
Mean Bias (ppb)	/	16.59	11.83	/	7.47	4.78
Mean Error (ppb)	/	18.65	13.57	/	8.00	5.39
Root Mean Square Error (ppb)	/	21.75	16.10	/	8.88	6.20
Mean Fractional Bias	/	0.29	0.22	/	0.95	0.77
Mean Fractional Error	/	0.31	0.24	/	0.98	0.82

Table 2.6 Same as Table 2.5 but for CASTENT sites, and model results were extracted at identical site altitudes.

Statistics	MDA8			W126 MI		
	Observation	60km/18L	12km/32L	Observation	60km/18L	12km/32L
Mean (ppb)	71.61	72.07	70.67	11.77	12.66	10.79
Standard Deviation (ppb)	19.51	7.94	11.78	7.99	4.02	5.70
Mean Bias (ppb)	/	0.46	-0.94	/	0.89	-0.98
Mean Error (ppb)	/	12.52	7.44	/	4.67	3.23
Root Mean Square Error (ppb)	/	13.40	8.28	/	5.37	4.44
Mean Fractional Bias	/	0.04	0.01	/	0.31	0.07
Mean Fractional Error	/	0.18	0.11	/	0.52	0.38

Table 2.7 US Geological Survey (USGS) land type numbers and method of grouping

Land type number	Land type description	Category used in Figures 2.4	Land type number	Land type description	Category used in Figure 2.4
1	Urban and Built-up Land	/	16	Water Bodies	/
2	Dryland Cropland and Pasture	Cropland	17	Herbaceous Wetland	/
3	Irrigated Cropland and Pasture		18	Wooden Wetland	/
4	Mixed Dryland/Irrigated Cropland and Pasture		19	Barren or Sparsely Vegetated	/
5	Cropland/Grassland Mosaic		20	Herbaceous Tundra	/
6	Cropland/Woodland Mosaic		21	Wooded Tundra	/
7	Grassland		Grass + Shrub	22	Mixed Tundra
8	Shrubland	23		Bare Ground Tundra	/
9	Mixed Shrubland/Grassland	24		Snow or Ice	/
10	Savanna				
11	Deciduous Broadleaf Forest	Forest			
12	Deciduous Needleleaf Forest				
13	Evergreen Broadleaf				
14	Evergreen Needleleaf				
15	Mixed Forest				

Source: http://www.mmm.ucar.edu/wrf/users/docs/user_guide_V3/users_guide_chap3.htm#_Land_Use_and

Table 2.8 The "IP" metric for trajectories starting from three locations, at all local daylight times during 16 June-14 July, 2008

Pacific Daylight Times		8:00	9:00	10:00	11:00	12:00	13:00	14:00	15:00	16:00	17:00	18:00	19:00	20:00
Starting locations	MBO 2.7 km	0.13	0.17	0.22	0.39	0.54	0.61	0.65	0.66	0.67	0.65	0.60	0.50	0.20
	THD 2.5 km	0.12	0.15	0.21	0.26	0.29	0.33	0.34	0.34	0.33	0.32	0.27	0.21	0.10
	SC 1.5 km	0.47	0.57	0.59	0.58	0.58	0.55	0.52	0.54	0.51	0.49	0.48	0.40	0.26

Table 2.9 Changes of daytime mean surface O₃ errors between different cases, where error=|modeled-observed| O₃

Cases	Min	1 st Quantile	Median	Mean	3 rd Quantile	Max
<i>AS- a priori</i>	-16.59	-9.15	-4.02	-5.01	-0.21	4.38
<i>AT-a priori</i>	-6.60E-02	-7.00E-03	-2.00E-03	-4.00E-03	1.00E-03	1.50E-02
<i>AO-a priori</i>	-8.10E-02	-2.00E-03	~0	8.00E-03	2.40E-02	1.10E-01
<i>AD-a priori</i>	-1.84E-01	-1.30E-02	-3.00E-03	-1.30E-02	~0	1.60E-02
<i>AST-AS</i>	-1.15	-0.10	0.13	0.18	0.50	1.01
<i>ASO-AS</i>	-0.80	-0.15	0.23	0.22	0.50	1.30
<i>ASD-AS</i>	-0.71	-0.12	0.37	0.35	0.70	1.54

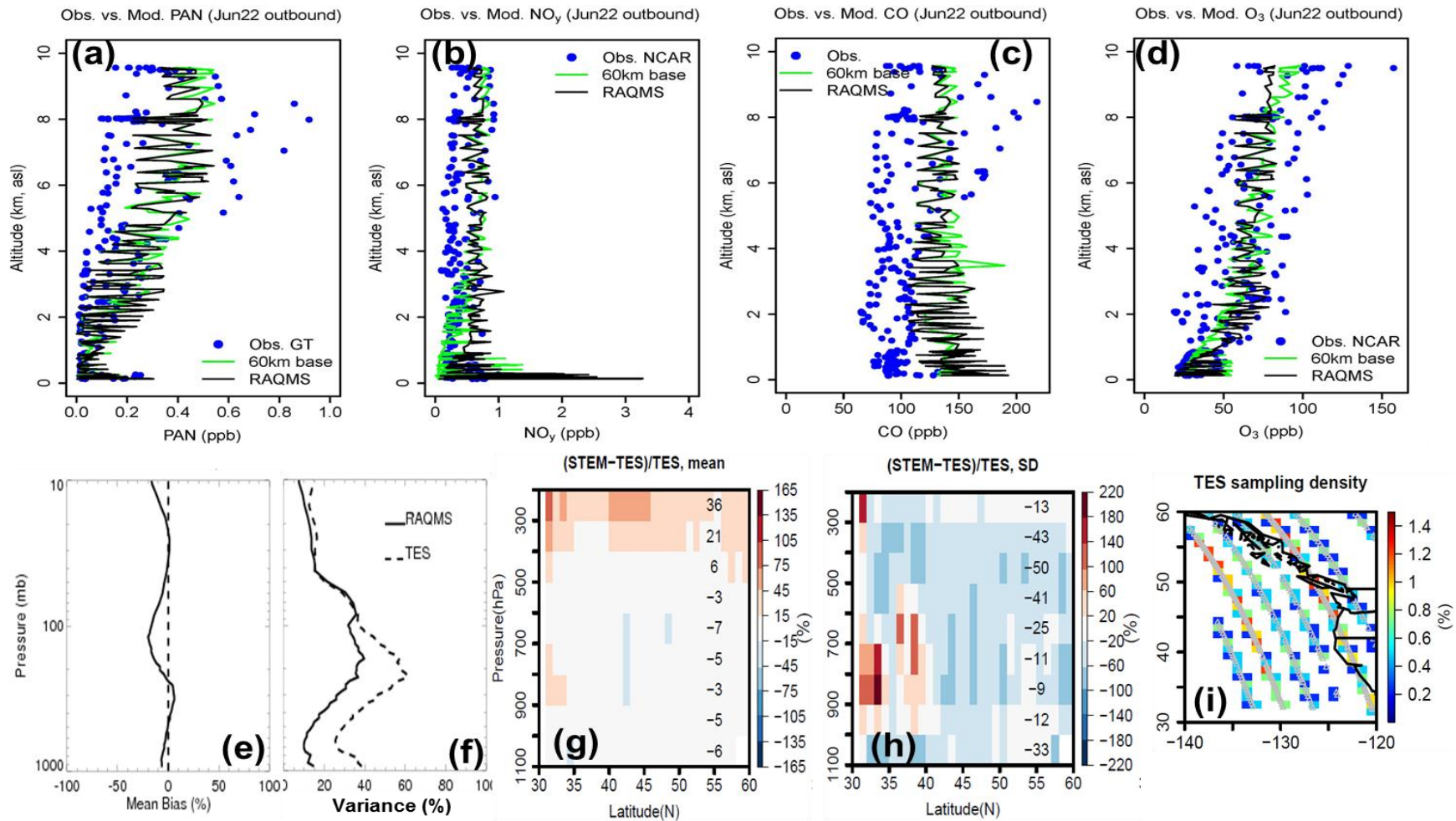


Figure 2.1 Observed and modeled (RAQMS and STEM 60 km) vertical profiles along the outbound part of the 22 June DC-8 flight, for (a) PAN; (b) NO_y; (c) CO; and (d) O₃; Comparison between TES and modeled O₃ mean (e;g) and variability (f;h) from RAQMS (e-f) and STEM 60 km (g-h) over eastern Pacific. TES observational operator was applied. (i) TES special observation sampling density in the compared domain for STEM. Sampling density=number of samples in each 1°×1°/total number of samples.

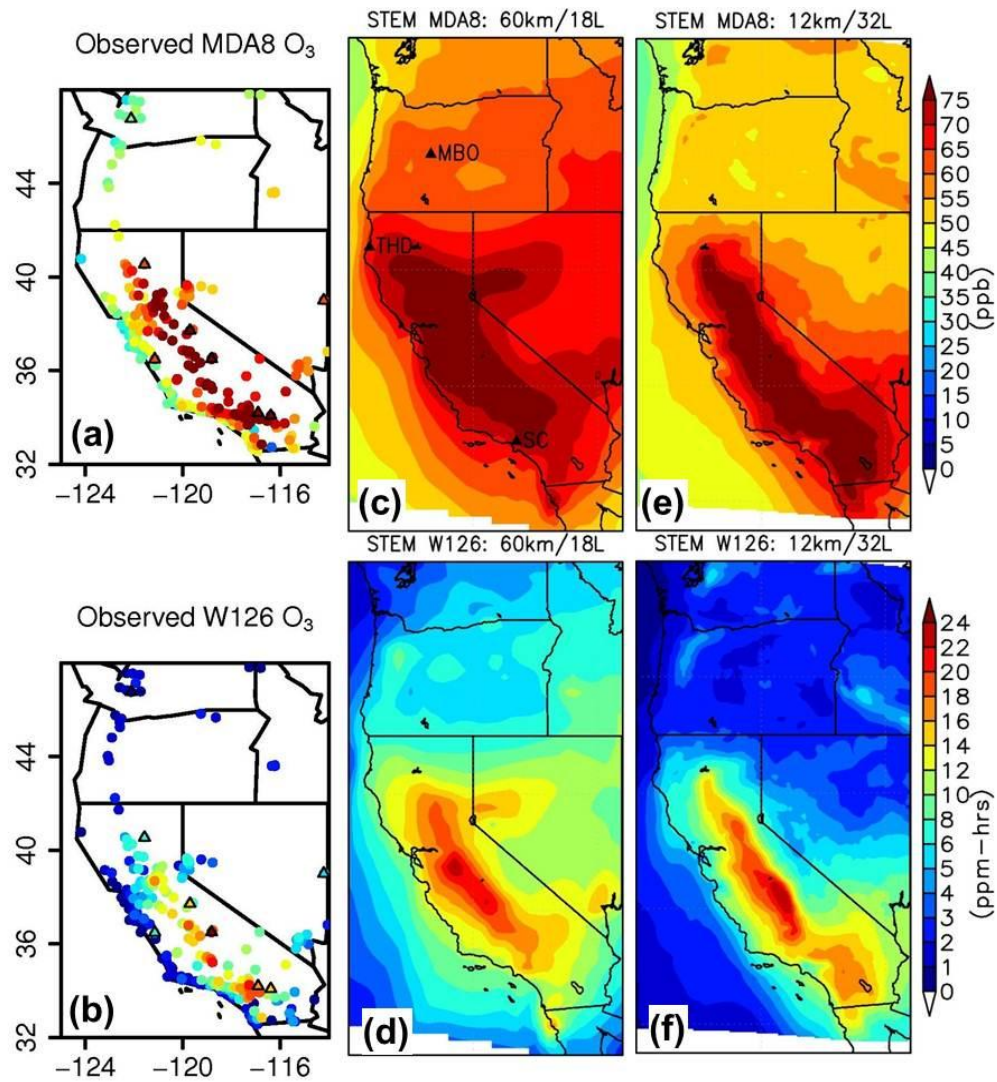


Figure 2.2 (a-b) Observed MDA8 and W126 monthly index (MI) at EPA AQS (dots) and CASTNET (triangles) sites; Modeled surface MDA8 and W126 MI in (c-d) 60 km/18 layer and (e-f) 12 km/32 layer grids.

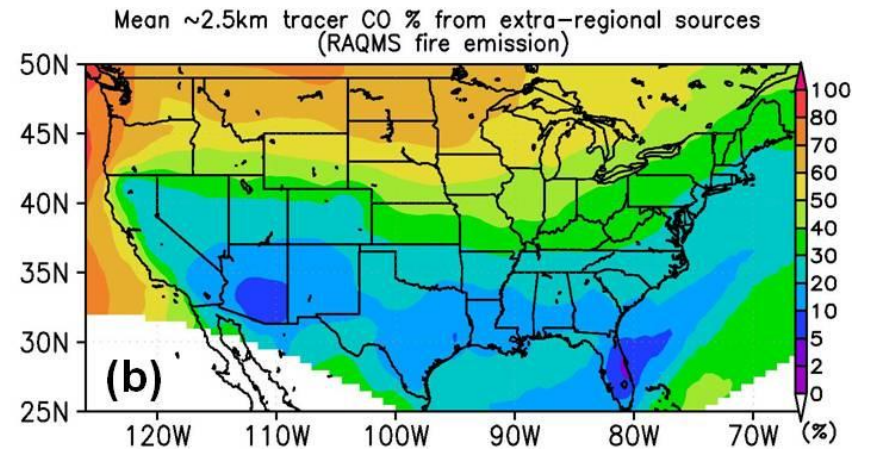
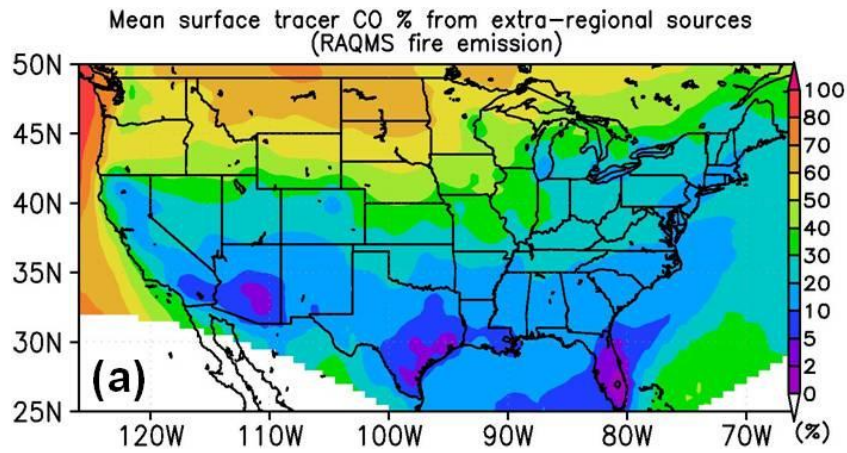


Figure 2.3 Period-mean non-NA tracer CO contributions (a) at surface and (b) at ~2.5 km AGL. The calculations were based on ARCTAS anthropogenic and RAQMS fire emissions.

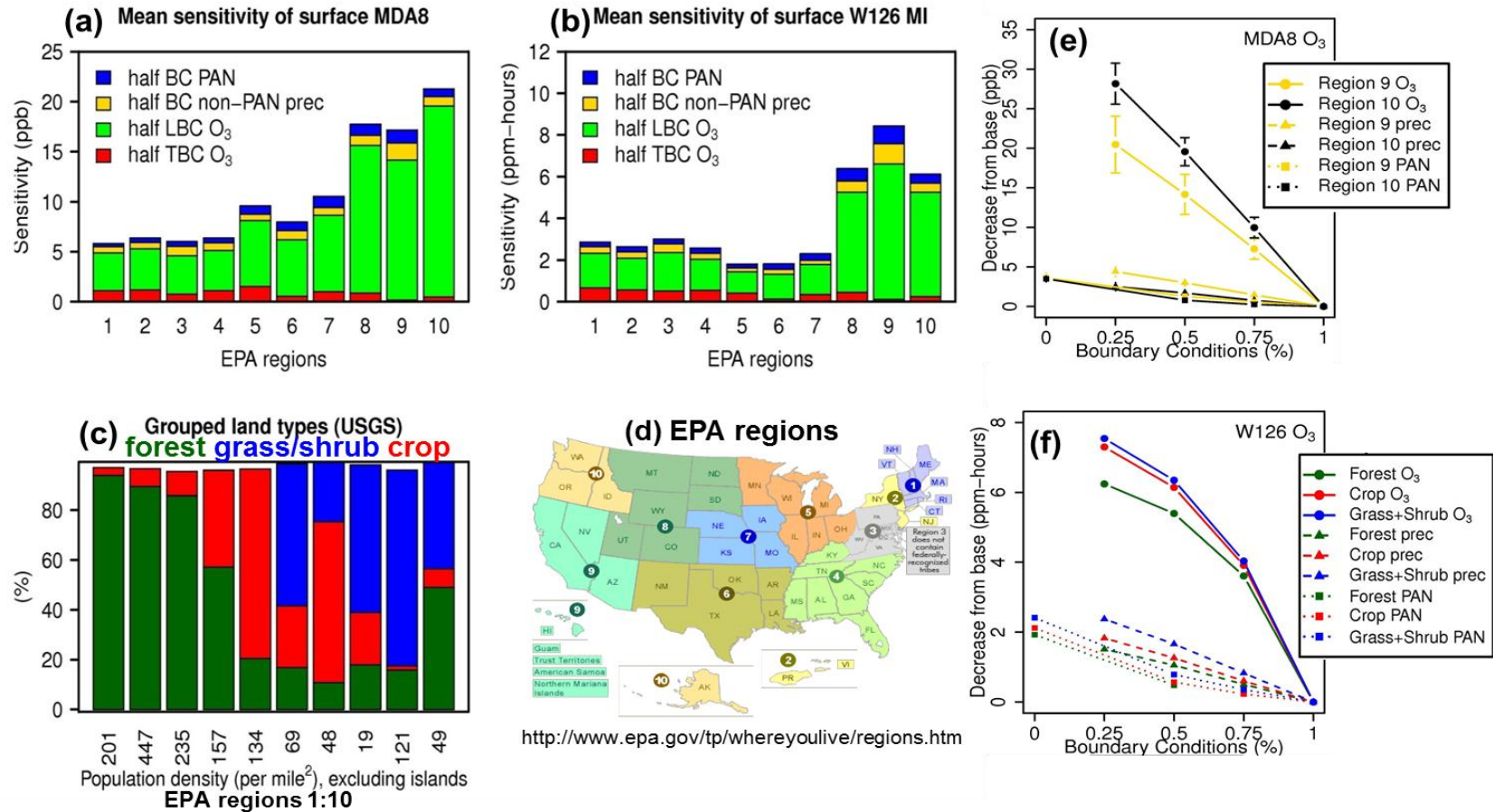


Figure 2.4 Surface (a) MDA8 and (b) W126 O₃ responses to perturbations in boundary conditions in the 60 km/18 layer grid, shown by ten EPA regions; (c) Fraction of the grouped USGS land types (bar) and population density (text below the bar) in ten EPA regions; (d) Ten EPA regions; Surface (e) MDA8 and (f) W126 O₃ responses to perturbations of various species in boundary conditions in the 60 km/18 layer grid, shown by geographical regions (EPA Regions 9 and 10) and grouped USGS land types, respectively (“prec” in legends: the cases in which CO, NO, NO₂, NO₃, HNO₃, HNO₄, PAN, N₂O₅ in BCs were perturbed).

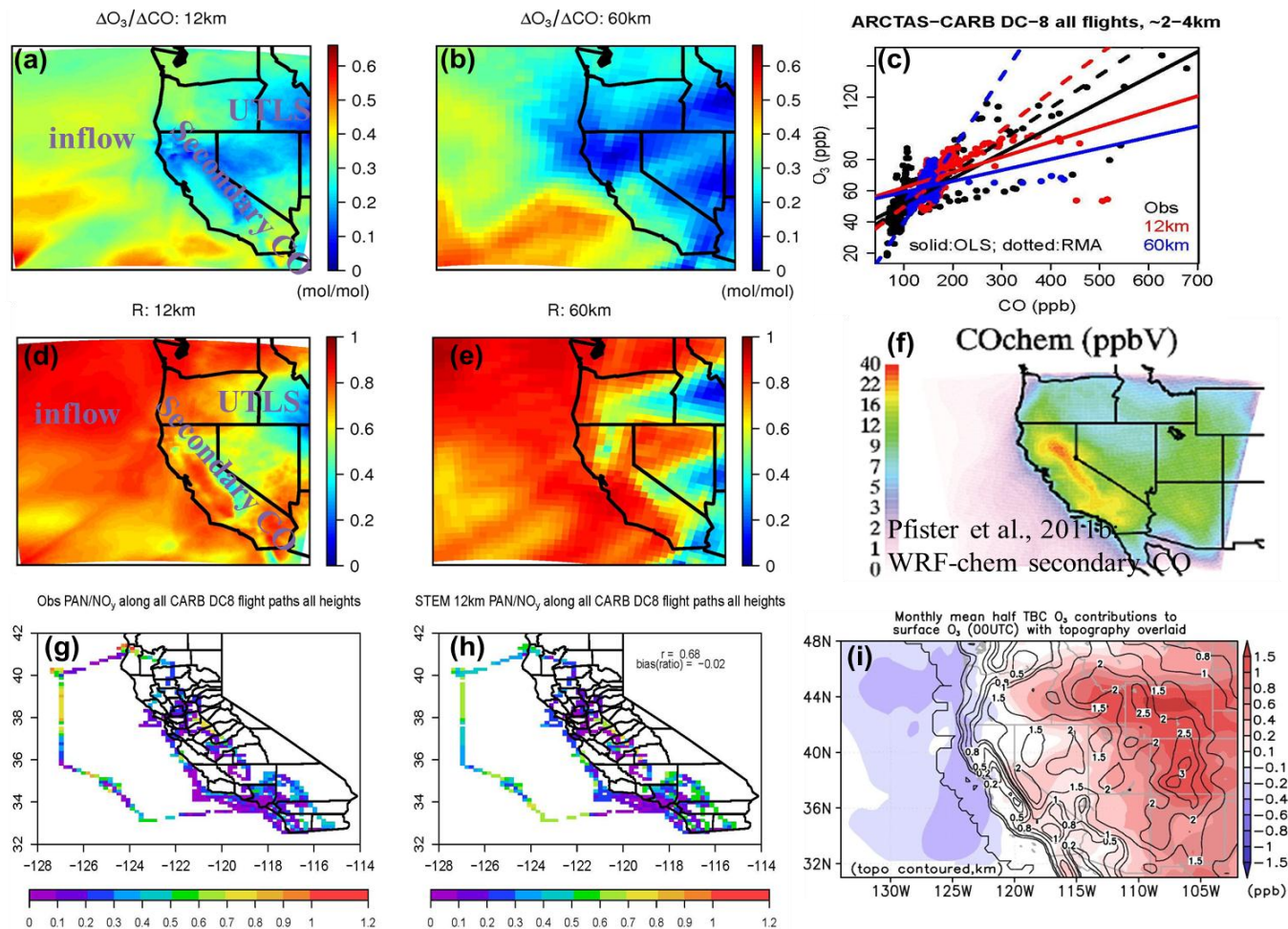


Figure 2.5 (a-b) Slope and (d-e) correlation of O₃ vs. CO at ~2.5 km AGL from (a;d) 12 km and (b;e) 60 km STEM base case for the study period; (c) Scatterplot of O₃ vs. CO along all ARCTAS-CARB DC-8 flight paths (at ~2-4 km); (f) WRF-chem tracer predicted secondary CO during the same studied period in Pfister et al. (2011b); (g) Observed and (h) STEM 12km modeled PAN/NO_y along all ARCTAS-CARB DC-8 flights at all altitudes; (i) Period mean 00 UTC surface O₃ sensitivity to half reduction in TBC O₃.

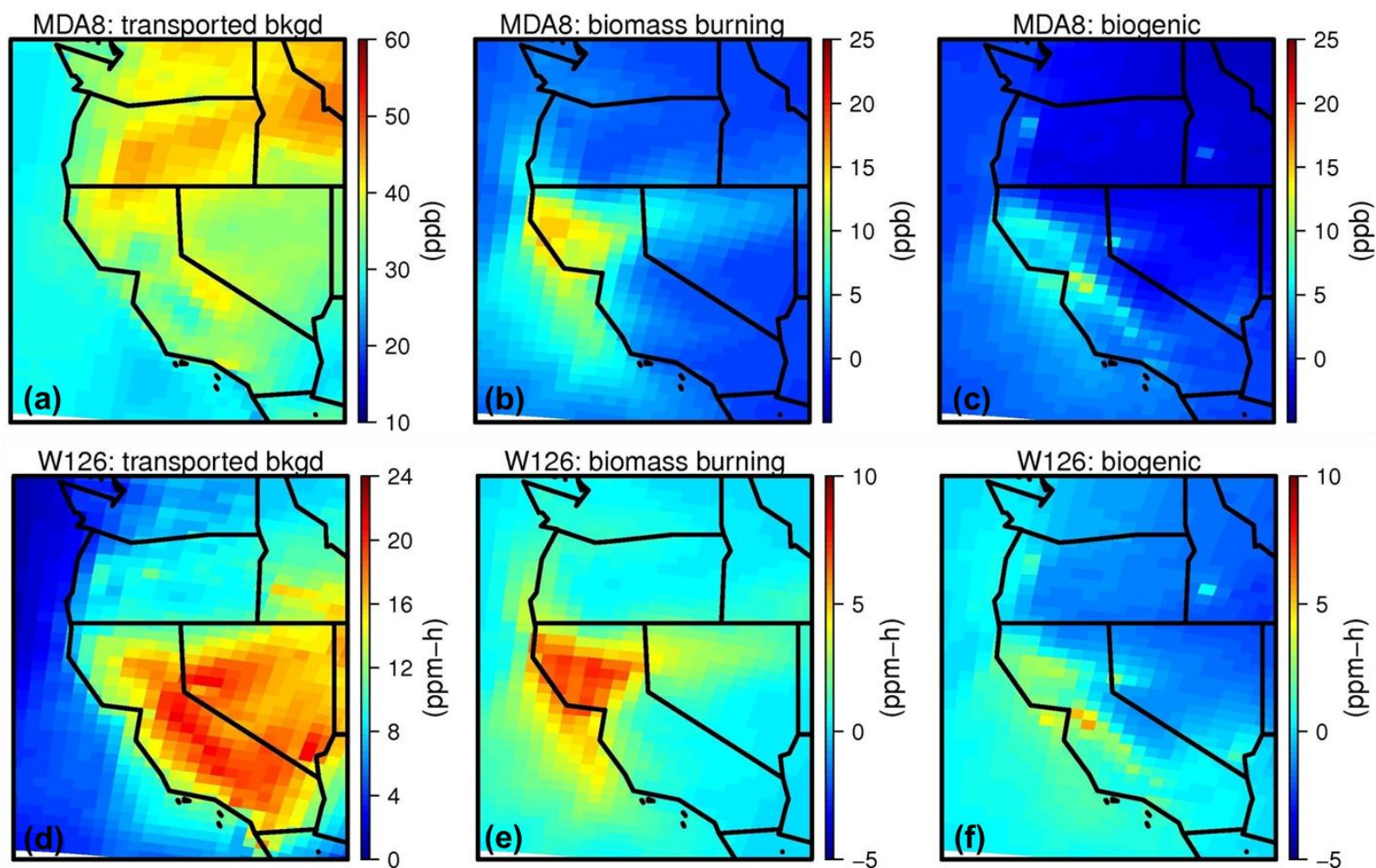


Figure 2.6 Surface (a-c) MDA8 and (b-d) W126 O₃ contributed from (a;d) transported background; (b;e) NA biomass burning emissions; and (c;f) biogenic emissions. To calculate (a) and (d), O₃ sensitivities to 75% reduction in O₃ and precursor BCs were extrapolated to 100% perturbation and summed up.

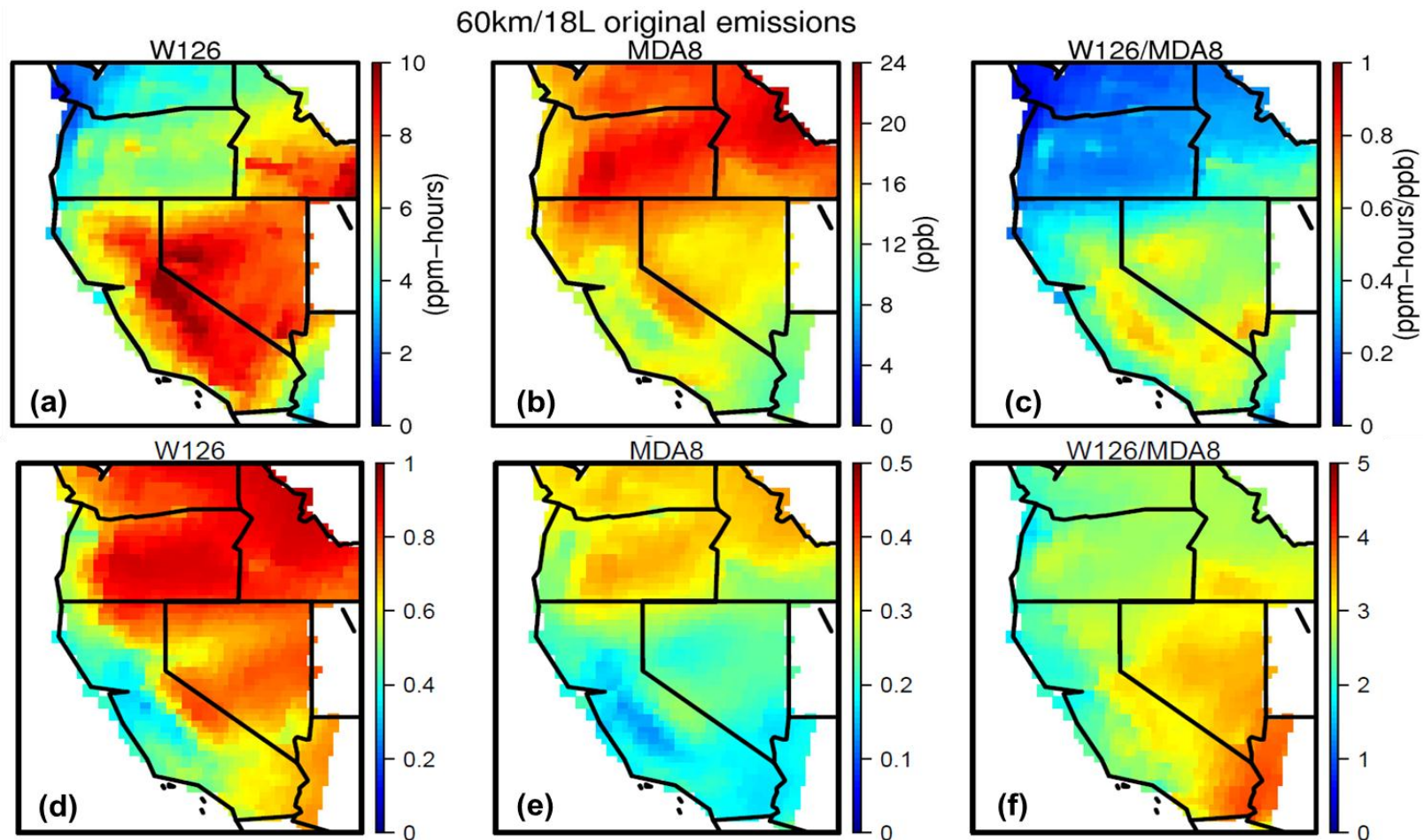


Figure 2.7 The surface O₃ sensitivity ($S1 = \text{base case} - \text{sensitivity case}$) of (a) W126, (b) MDA8 and (c) ratio of (a)/(b); The surface O₃ relative sensitivity ($S2 = (\text{base case} - \text{sensitivity case}) / \text{base case}$) of (d) W126, (e) MDA8 and (f) ratio of (d)/(e). Results are all from the 60 km/18 layer STEM grid. The sensitivity case here refers to 50% reduction in O₃ BC. For subsequent comparison with results from other model grids, the shared areas in EPA Regions 9 and 10 in both 60 km and 12 km domains are shown with the same smoothing method.

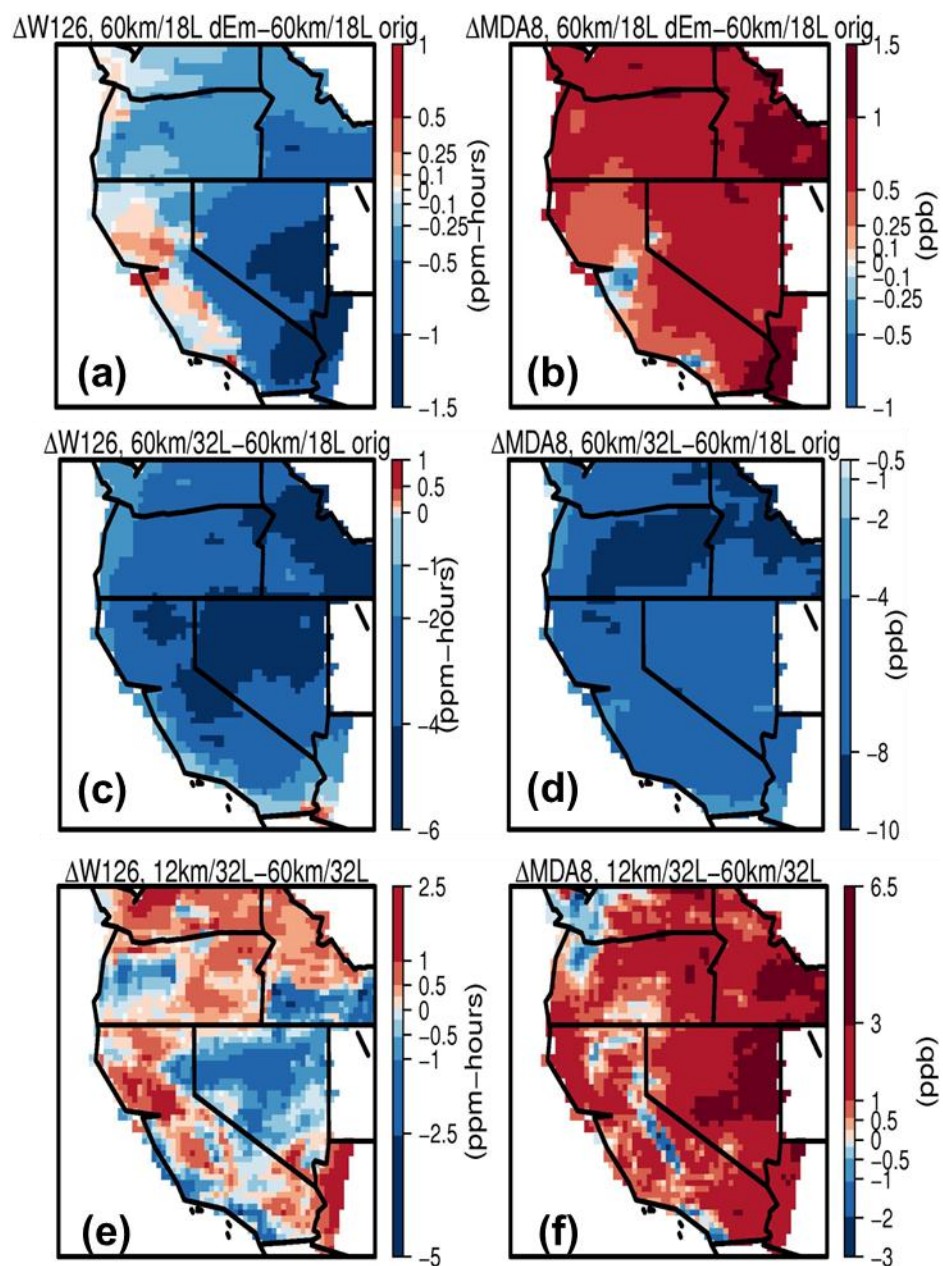


Figure 2.8 Differences of SI (defined in Figure 2.7 caption) for W126 (a;c;e) and MDA8 (b;d;f) between the cases of (a-b) using the scaled and original US anthropogenic emissions in 60 km/18 layer grid; (c-d) in 60 km/32 layer and 60 km/18 layer grids; and (e-f) in 12 km/32 layer and 60 km/32 layer grids.

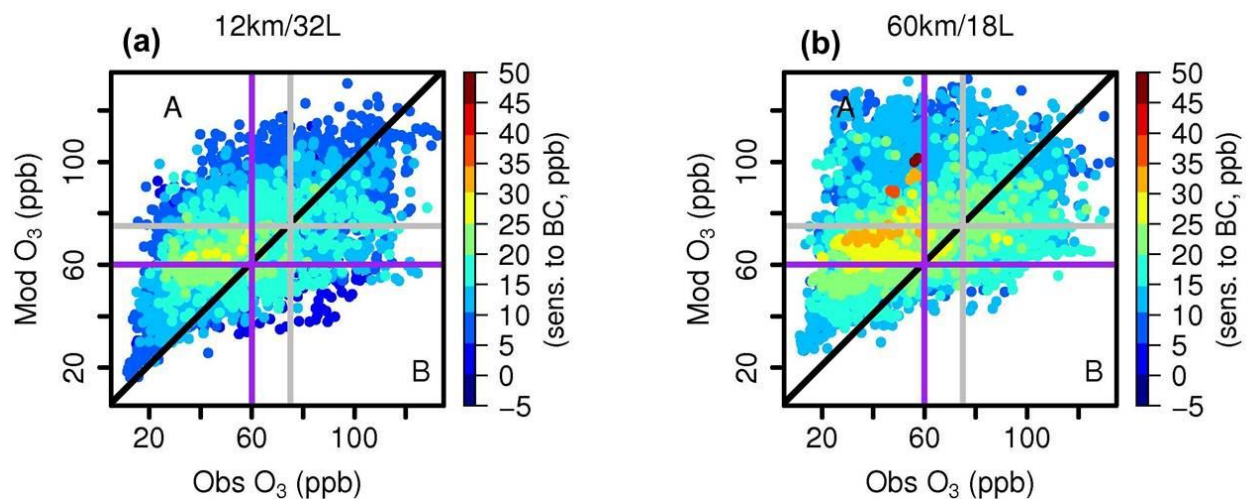


Figure 2.9 Scatter plots of modeled and observed daily maximum 8-hour average O_3 at all AQS sites, colored by their sensitivities to 50% reduction in BC O_3 , in the (a) 12 km/ 32 layer and (b) 60 km/18 layer grids. Regions A and B marked in both panels refer to “erroneously-predicted non-attainment areas” and “the actual non-attainment areas missed by the model”, respectively.

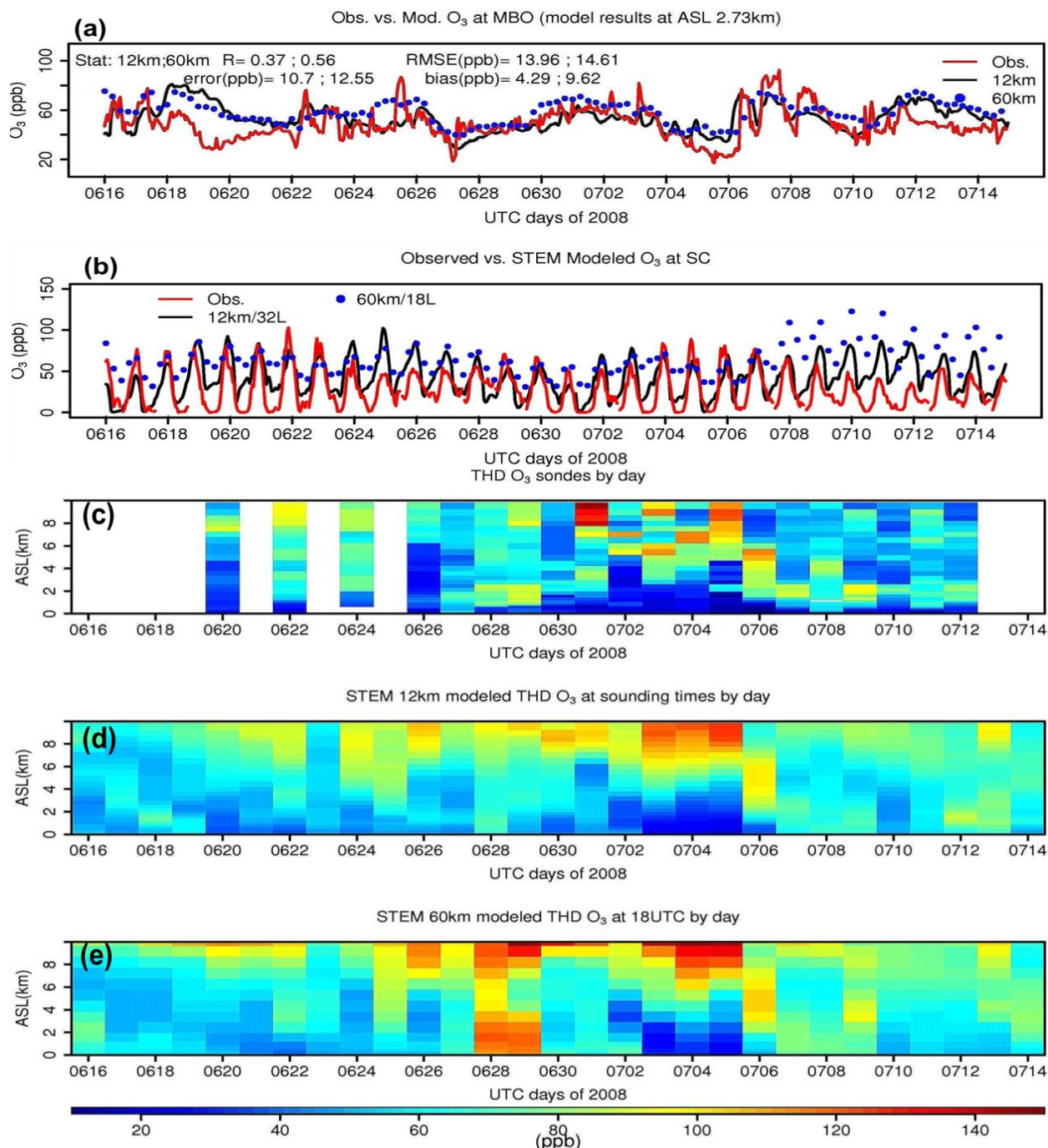


Figure 2.10 (a) Observed and STEM modeled O₃ time series at the MBO site from 60 km/18 layer and 12 km/32 layer grids. The model results were extracted from the layer(s) that matched the actual MBO altitude; (b) Observed and STEM modeled O₃ time series at SC surface site from the 60 km/18 layer and 12 km/32 layer grids; (c) THD daily ozone sonde data during the studied period, binned into 32 model layers; (d) STEM 12 km modeled THD O₃ daily vertical profiles at ~sounding times during the same period; (e) STEM 60 km modeled THD O₃ daily vertical profiles at 18 UTC during the same period.

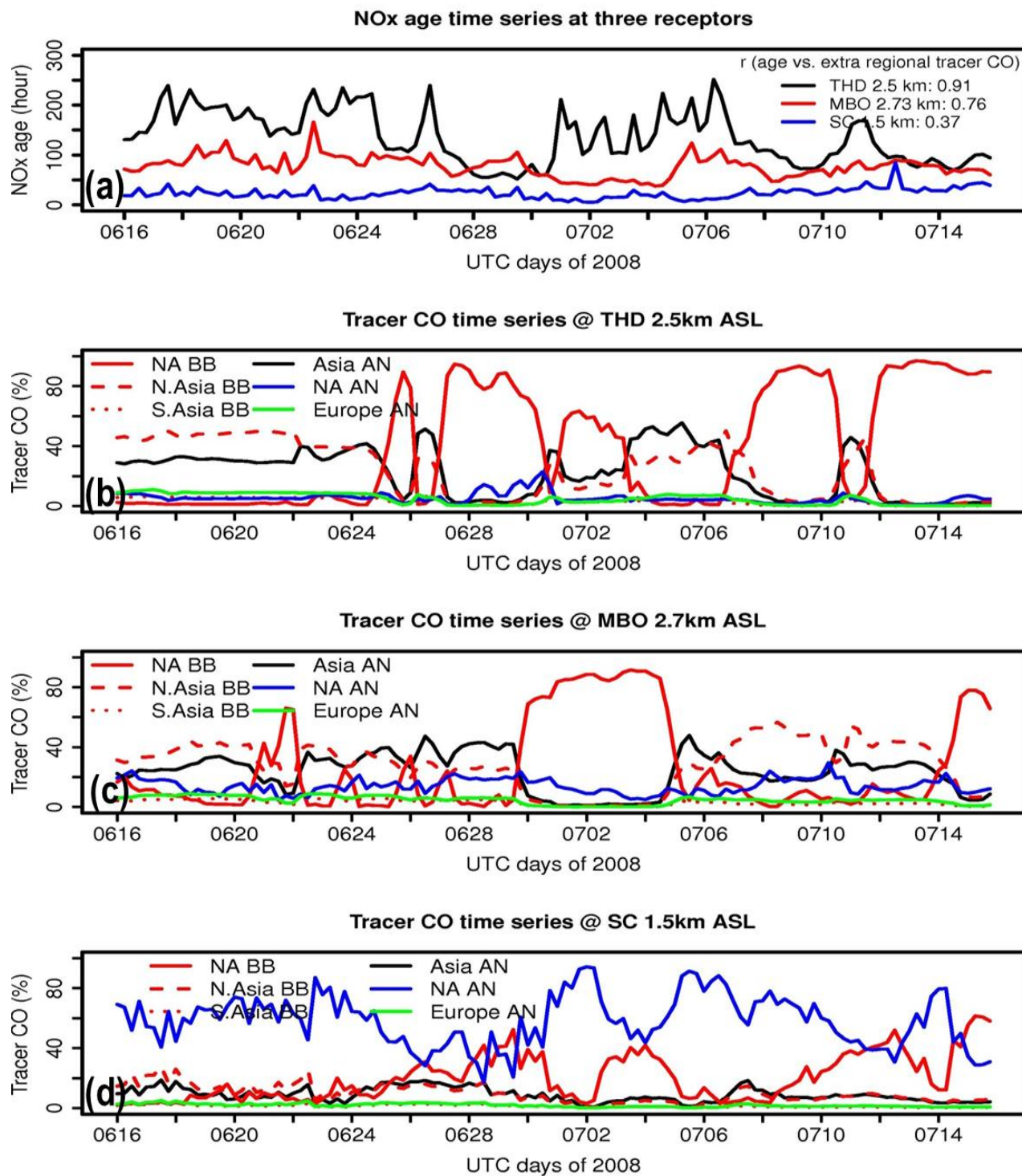


Figure 2.11 Time series plots of (a) Tracer calculated NO_x age (hours) time series at three locations; Tracer CO contributions (%) to (b) THD 2.5 km; (c) MBO 2.7 km; and (d) SC 1.5 km ASL from various sources.

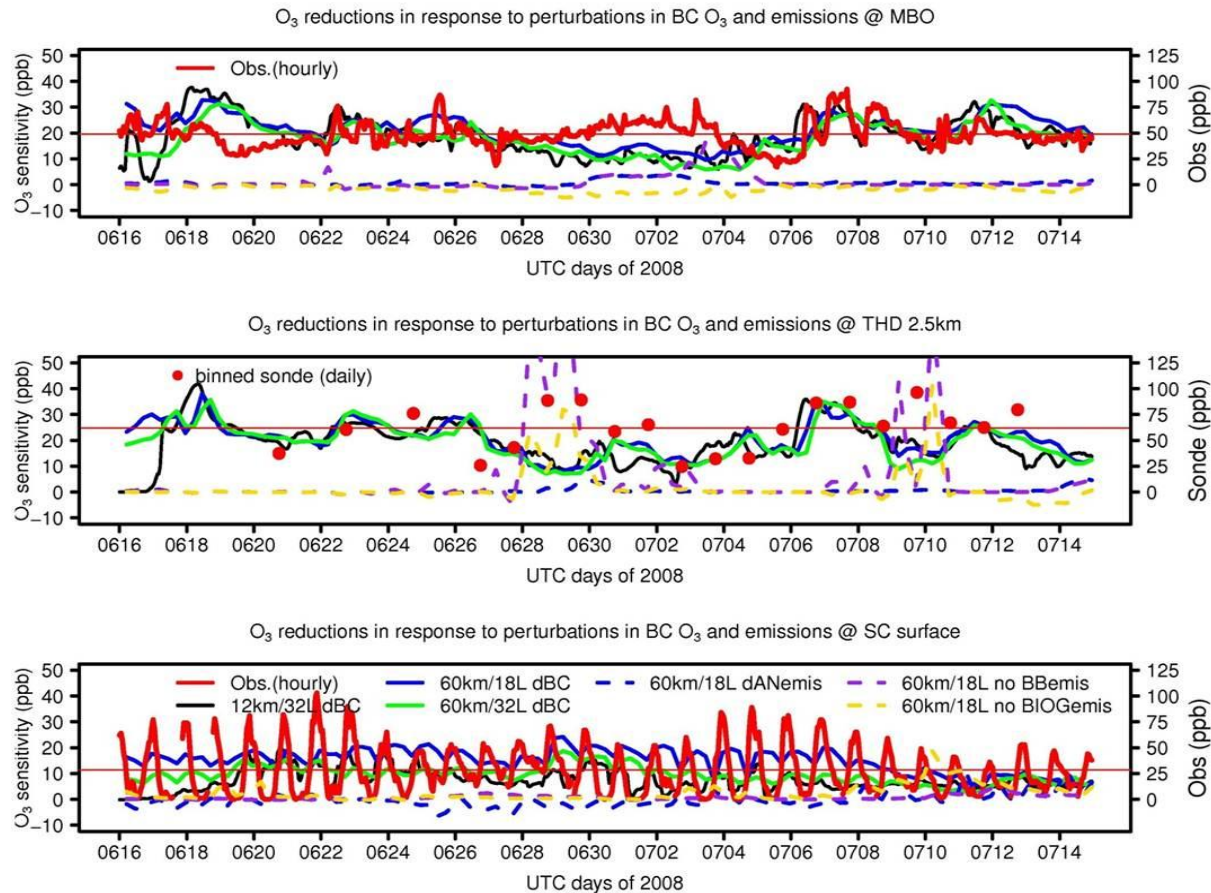


Figure 2.12 Time series of O₃ reductions at (a) MBO 2.7 km ASL; (b) THD 2.5 km ASL; and (c) SC lowest level, in response to 50% perturbations in BC O₃, reduction in US anthropogenic emissions and zeroing out the US biomass burning emissions. Time series of observations at the corresponding altitude are overlaid in red and their period mean are drawn as horizontal thin red lines.

Two-day forward traj during the studied month, averaged by 0.25X0.25 degree

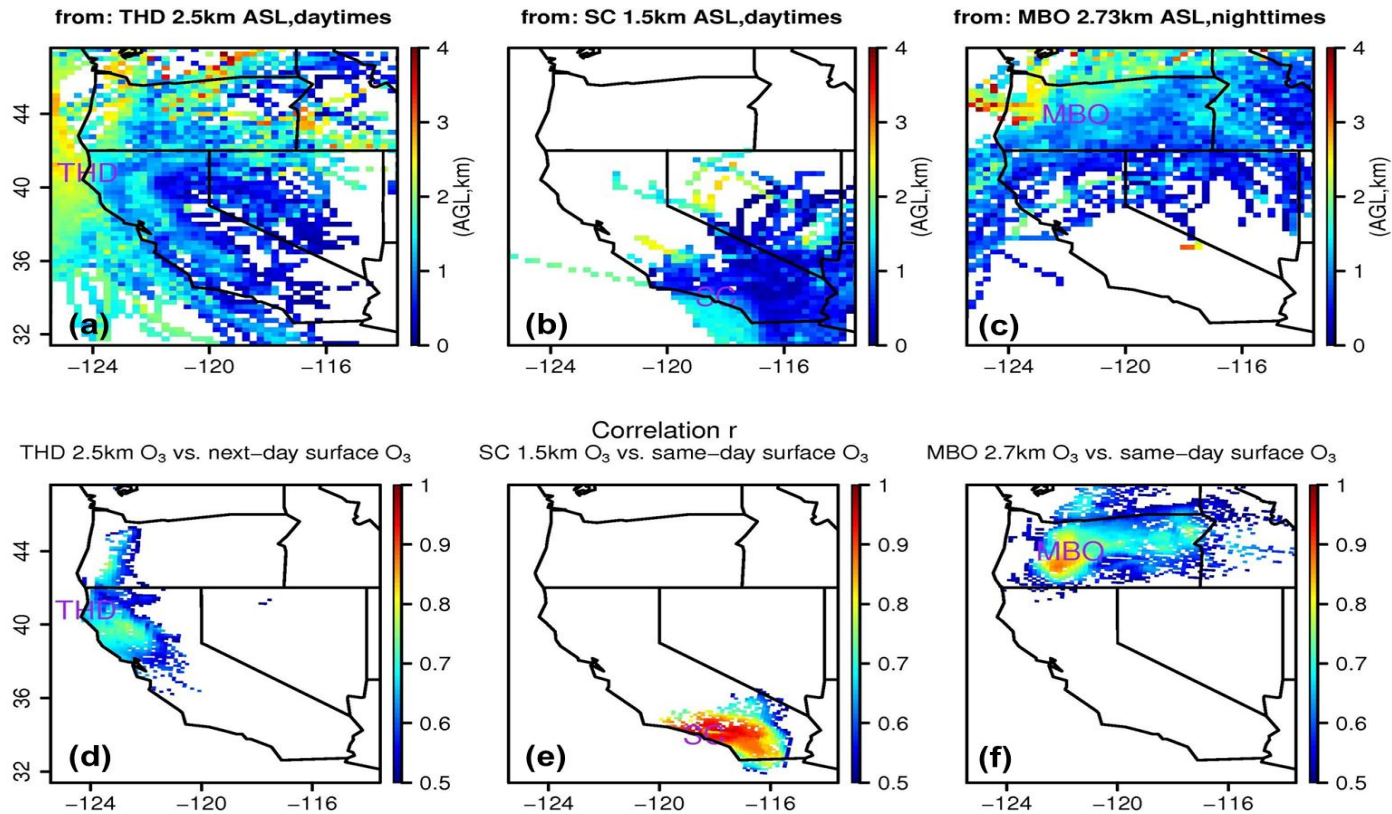


Figure 2.13 PDT 8am-8pm (daytimes) forward trajectories (calculated mean transported altitudes in km, AGL for every 0.25 degree) during the studied period originating from (a) THD 2.5 km ASL and (b) SC 1.5 km ASL; (c) PDT 9pm-7am (nighttimes) forward trajectories during the study period originating from MBO 2.7 km ASL; Correlation of daily mean PDT 8 am-8 pm O₃ at (d) THD 2.5 km ASL; (e) SC 1.5 km ASL with ground O₃ one-day later, and with the same day ground O₃, respectively, during the same period; (f) Correlation of daily mean PDT 9 pm-7 am O₃ at MBO 2.7 km with ground daytime O₃ on the same day ground O₃, during the same period. The correlations are filtered by trajectories.

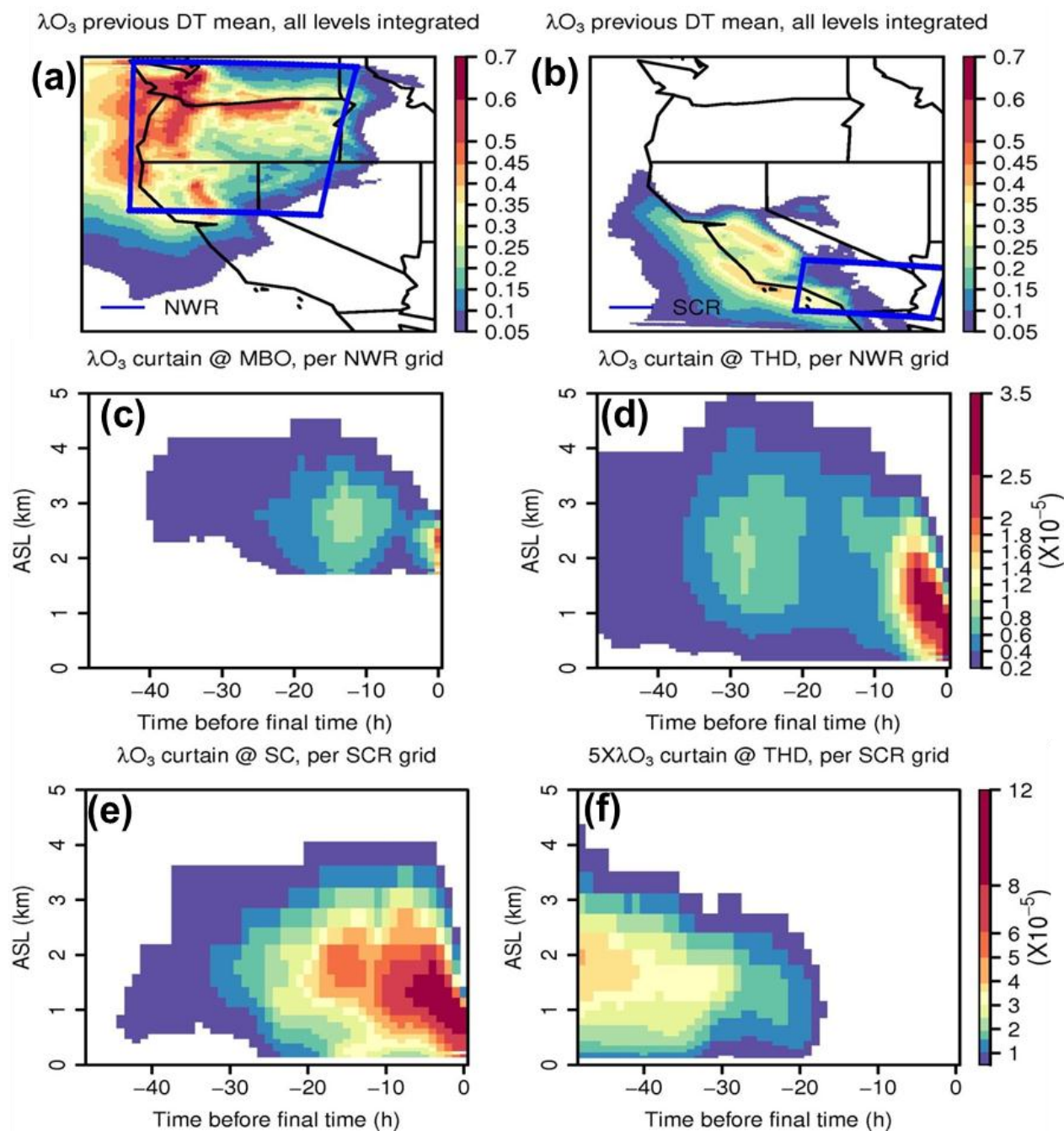


Figure 2.14 Previous daytime mean $\lambda[\text{O}_3]$ in (a) NWR case and (b) SCR case, all levels integrated; Areas within the blue lines indicate receptor regions; (c) $\lambda[\text{O}_3]$ time-height curtain at MBO, NWR case; (d) $\lambda[\text{O}_3]$ time-height curtain at THD, NWR case; (e) $\lambda[\text{O}_3]$ time-height curtain at SC, SCR case; (f) $\lambda[\text{O}_3]$ time-height curtain at THD, SCR case. (c-e) were normalized by receptor grid numbers, note the different color scales. Results from 12 km/32 layer grid.

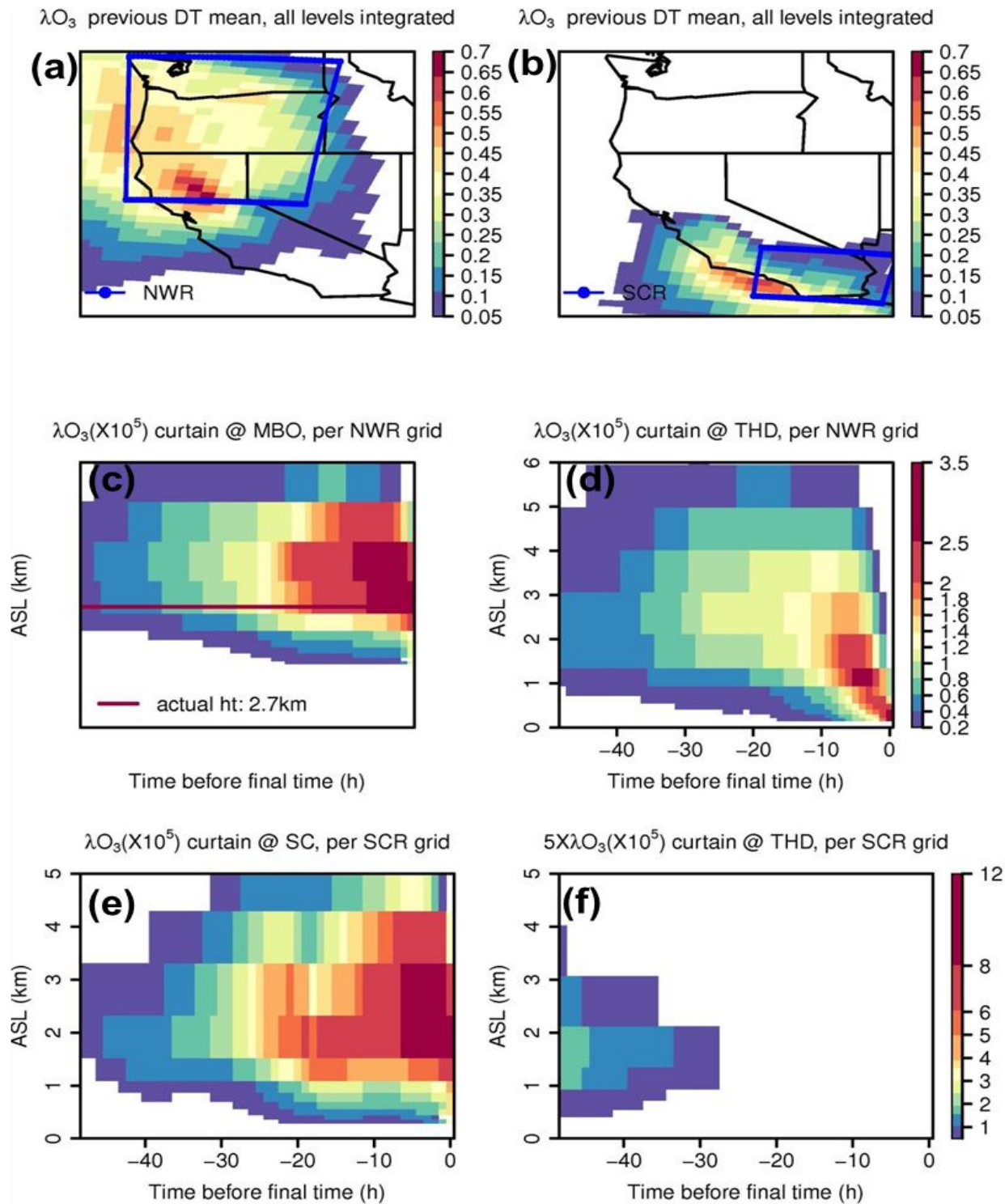


Figure 2.15 Same as Figure 2.14 but for results from 60 km/18 layer grid.

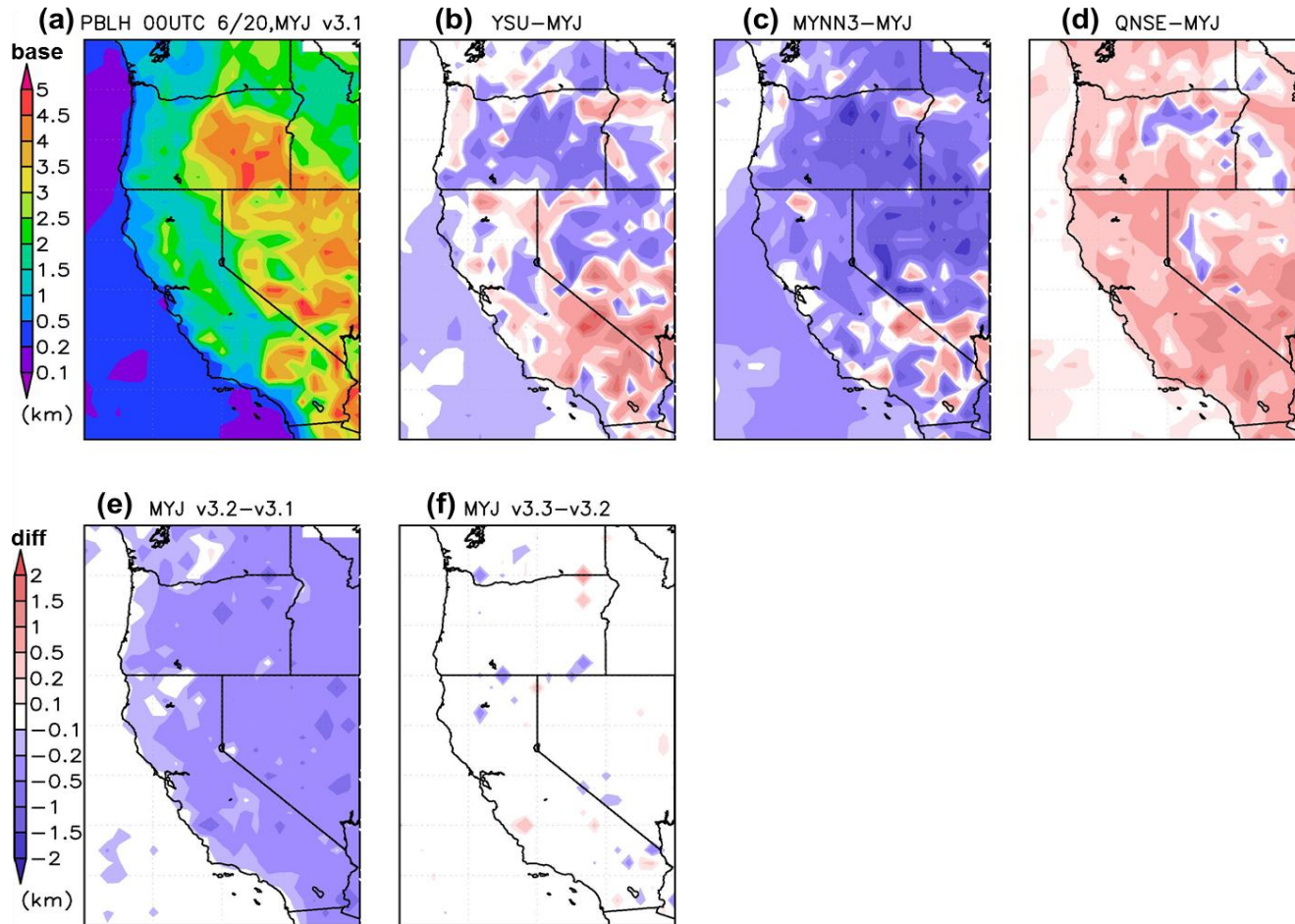


Figure 2.16 (a) 12 km WRF (Version 3.1)-predicted PBLH at 00 UTC, 20 June, by using the MYJ PBL scheme; Differences of WRF (Version 3.1)-predicted PBLH between MYJ case and the cases using (b) YSU; (c) MYNN3; and (d) QNSE PBL schemes; Differences of WRF-predicted PBLH Version 3.1 and the cases using (e) Version 3.2 and (f) Version 3.3.

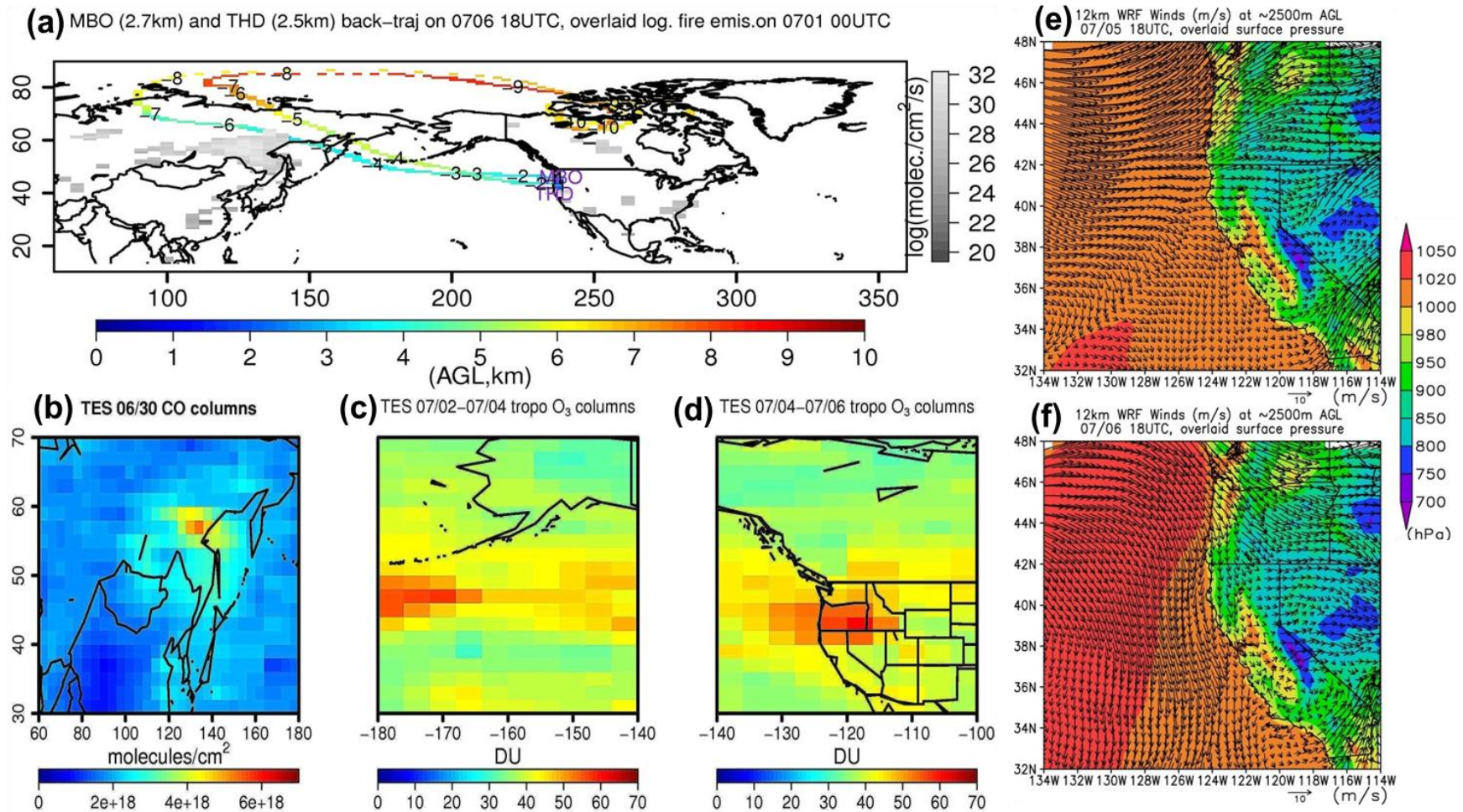


Figure 2.17 (a) MBO and THD back-trajectories ending at 18 UTC on 6 July, colored by travelling heights (AGL, km), based on the 60 km WRF-simulated wind fields. Negative numbers along the trajectories indicate days back from the ending time. RAQMS fire emissions ($\log(\text{molec./cm}^2/\text{s})$) at 00 UTC, 1 July are overlaid with grey color scale; TES Level 3 nadir (b) total CO (on 30 June) and (c-d) tropospheric O₃ (on 2, 4, 6 July) columns; 12 km WRF-simulated ~2.5 km wind fields overlaid with surface level pressure (SLP, hPa) at 18 UTC on (e) 5 July and (f) 6 July.

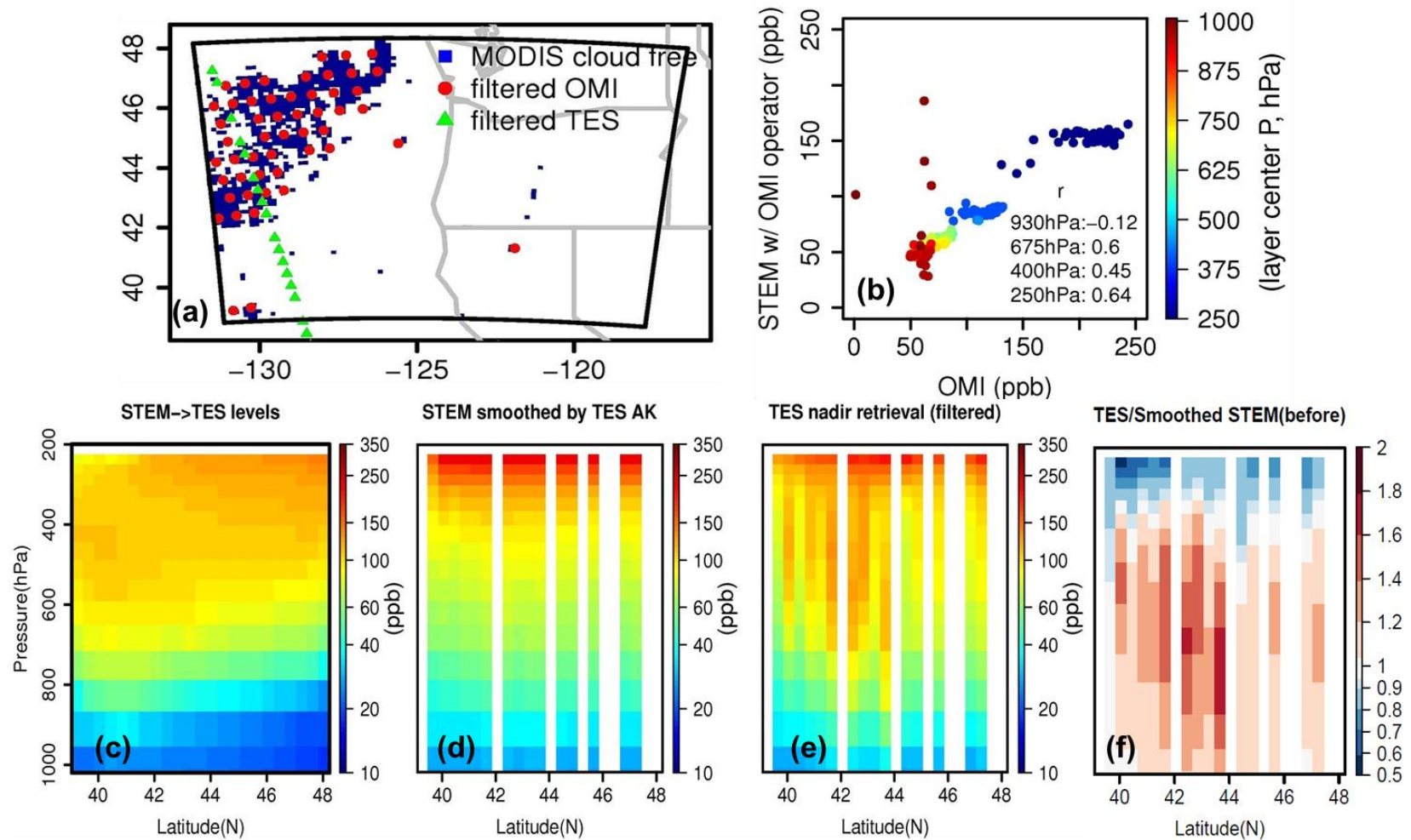


Figure 2.18 (a) DA domain in 12 km/32 layer grid and the locations where the selected (based on criteria described in Table 2.4) TES and OMI measurements were made; (b) Scatter plot of STEM *a priori* (with OMI observation operator) vs. OMI retrieval, colored by OMI layer center pressure (hPa); (c) STEM *a priori* (raw data) along the TES orbit, interpolated into the TES pressure levels; (d) STEM *a priori* (with TES observation operator) along the TES orbit; (e) TES nadir retrieval; (f) The ratios of (e)/(d).

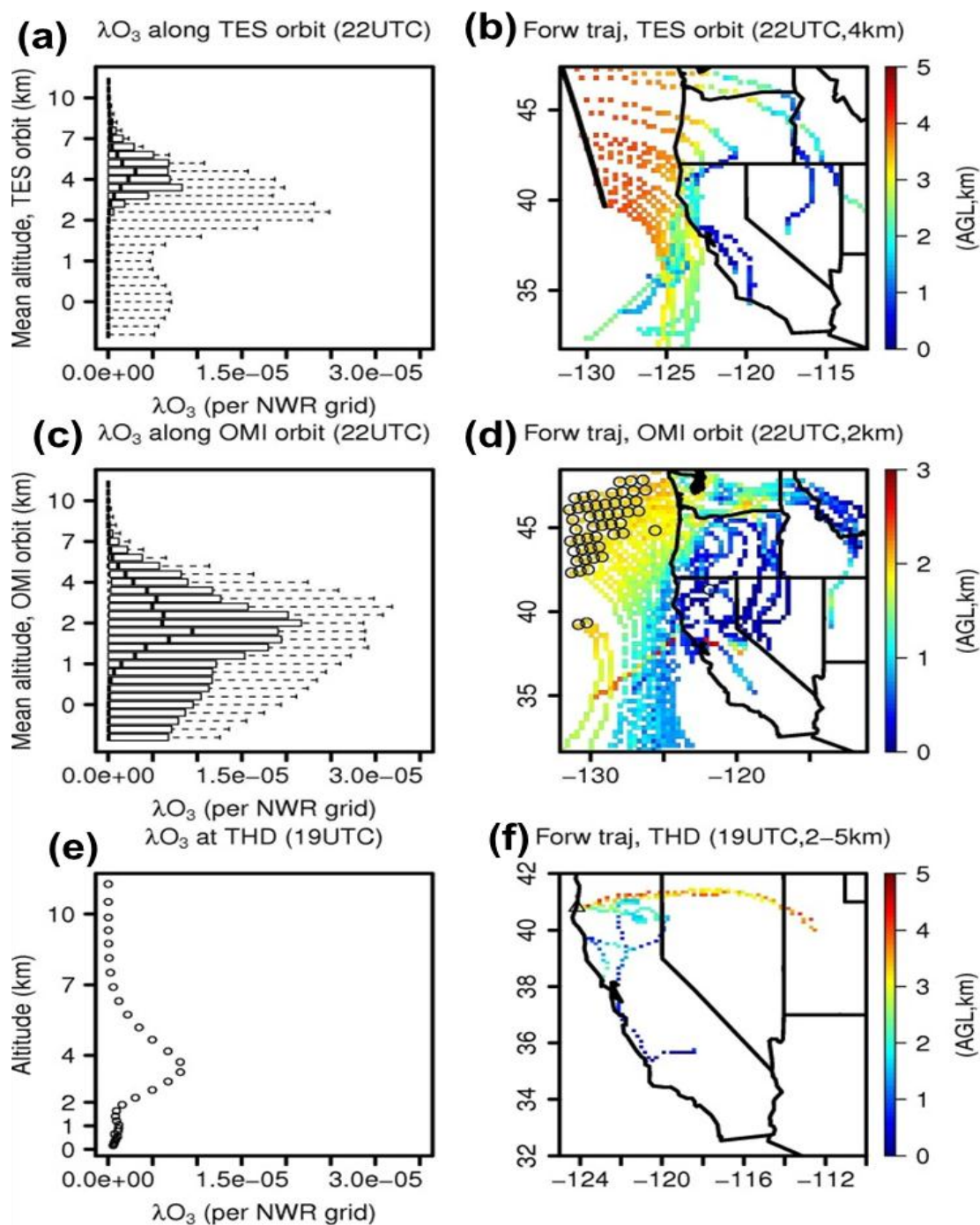


Figure 2.19 Vertical profiles of adjoint $\lambda[\text{O}_3]$ at selected (a) TES and (c) OMI sampling locations at 22 UTC on 5 July, shown as boxplots (minimum, 1st Qu., median, 3rd Qu. and extreme); and (e) at THD site at 19 UTC on July 5. Receptor/final time is NWR/00 UTC on 7 July. Forward trajectories (colored by travelling altitudes) originating at selected (b) TES (~4 km) and (d) OMI (~2 km) sampling locations at 22 UTC on 5 July; and (e) at THD site (2, 3, 4, 5 km) at 19 UTC on 5 July.

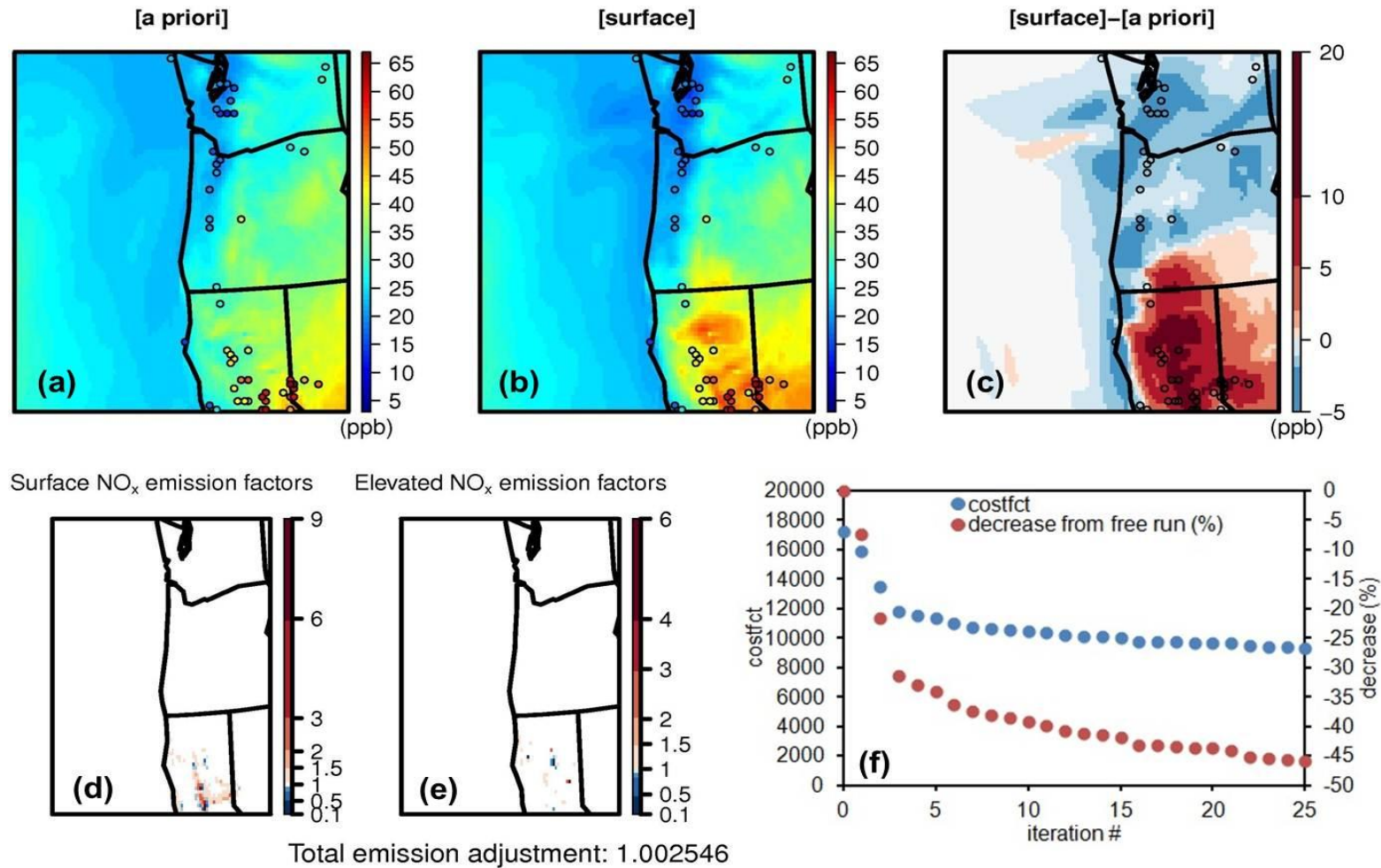


Figure 2.20 Daytime mean surface O_3 from (a) STEM *a priori*; and (b) *Case AS*. The site measurements were overlaid (only those sites that had all daytime measurements were shown in the plots); (c) Differences of (b)-(a); (d) Surface and (e) elevated NO_x emission scaling factors by controlling NO_x emissions and assimilating surface NO_2 observation in a 24-hour window; (f) Cost function and its reduction as a function of iteration number in *Case AS*.

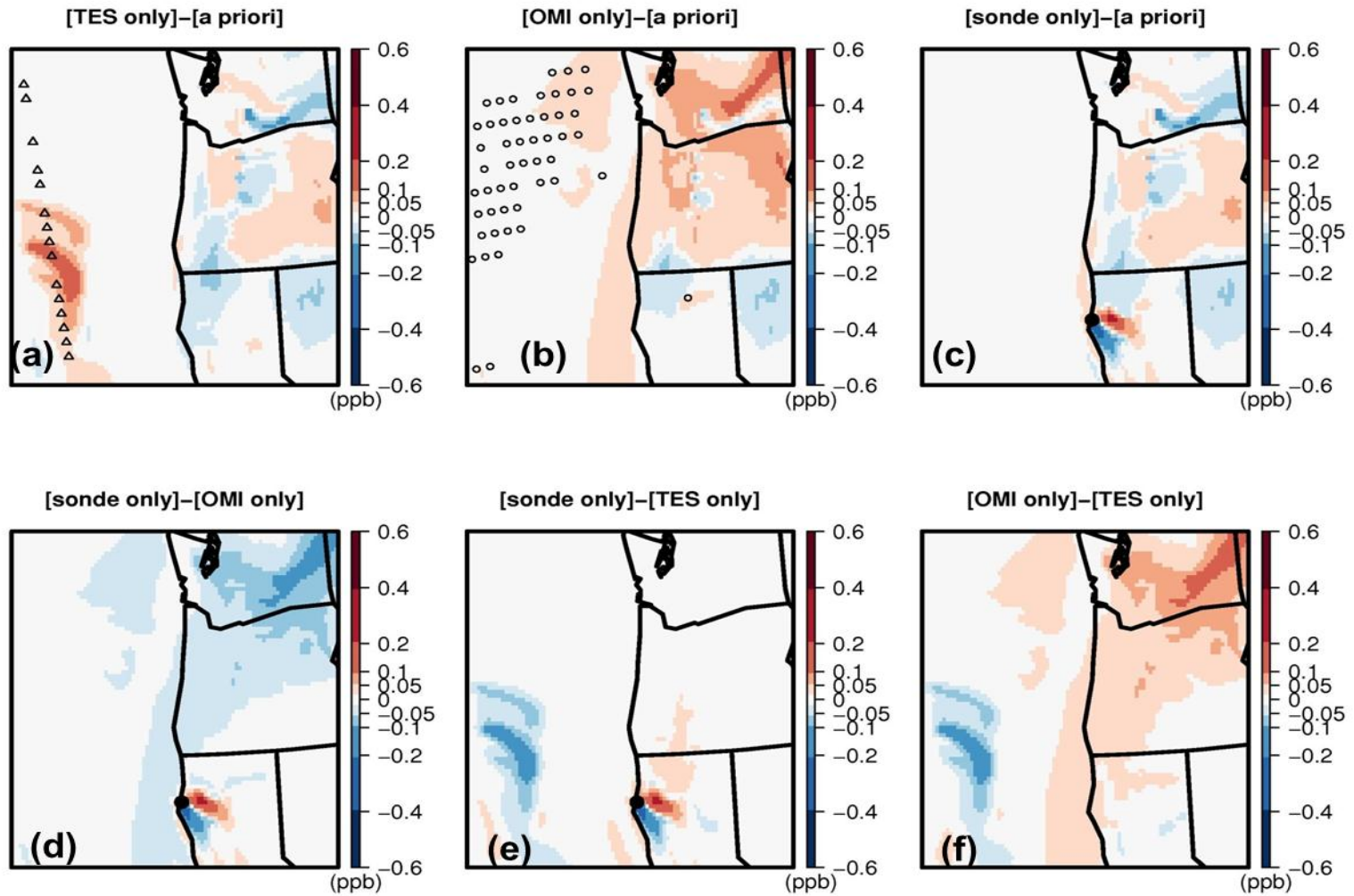


Figure 2.21 Daytime mean surface O₃ differences: (a) Case AT-STEM *a priori*; (b) Case AO-STEM *a priori*; (c) Case AD-STEM *a priori*; (d) Case AD- Case AO; (e) Case AD- Case AT; (d) Case AO- Case AT.

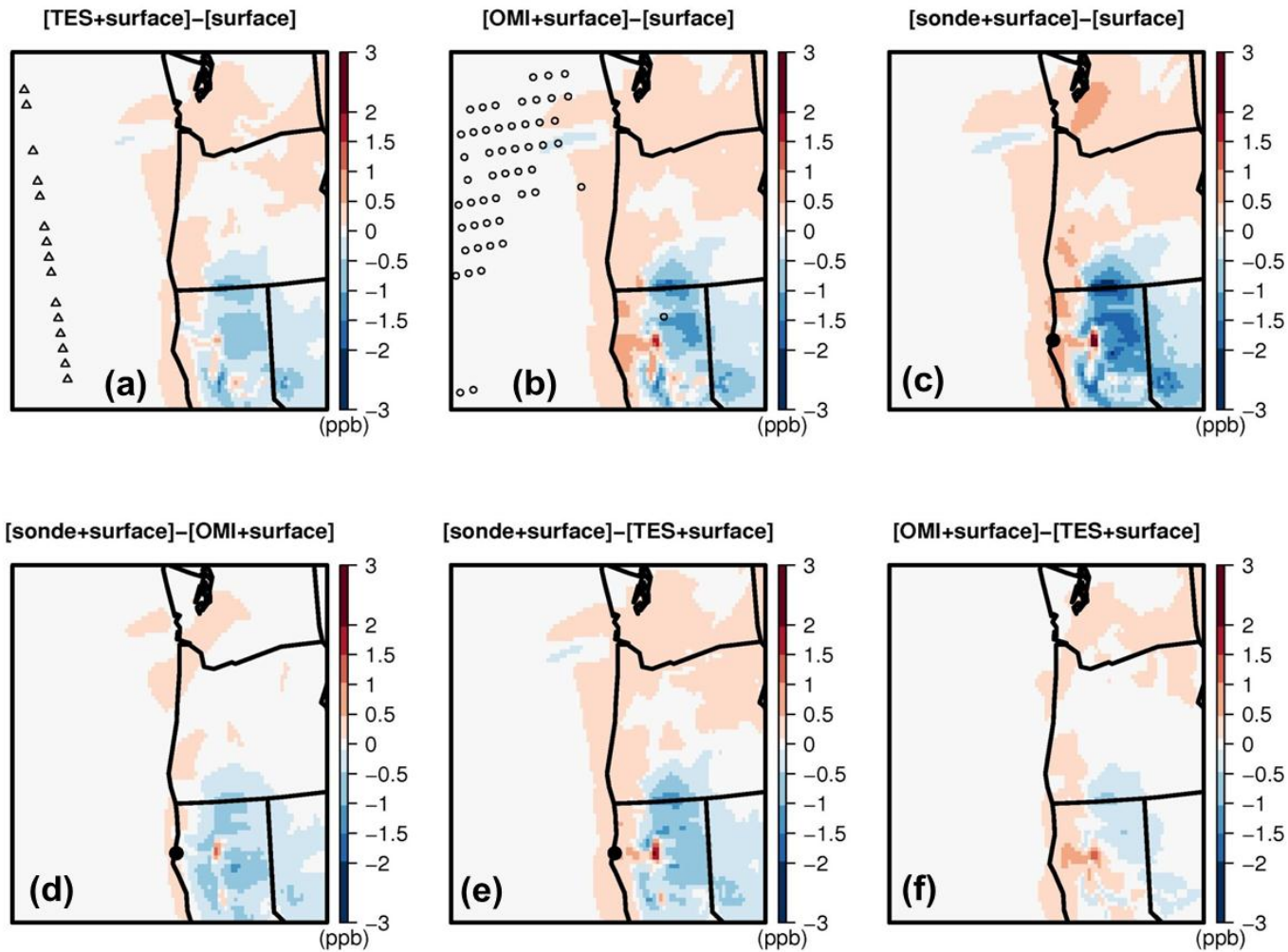


Figure 2.22 Daytime mean surface O₃ differences: (a) Case AST-Case AS; (b) Case ASO-Case AS; (c) Case ASD-Case AS; (d) Case AST-Case ASO; (e) Case ASD-Case AST; (f) Case ASO-Case AST.

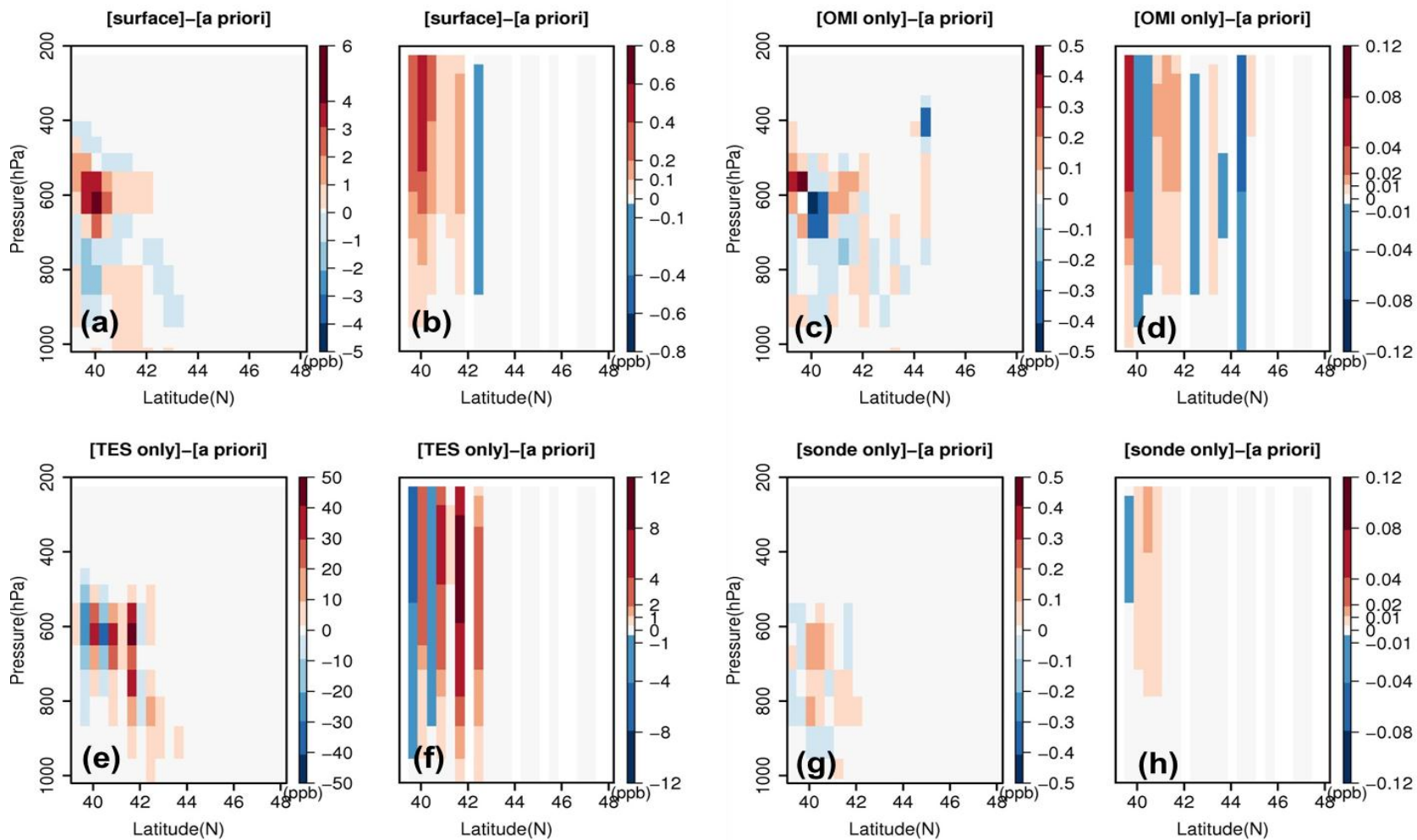


Figure 2.23 O₃ changes (assimilated fields-the *a priori*) at selected TES sampling locations for (a-b) *Case AS*; (c-d) *Case AO*; (e-f) *Case AT*; (g-h) *Case AD*. (a;c;e;g) compare the raw data in TES pressure grids and (b;d;f;h) compare the results after applying the TES observation operator.

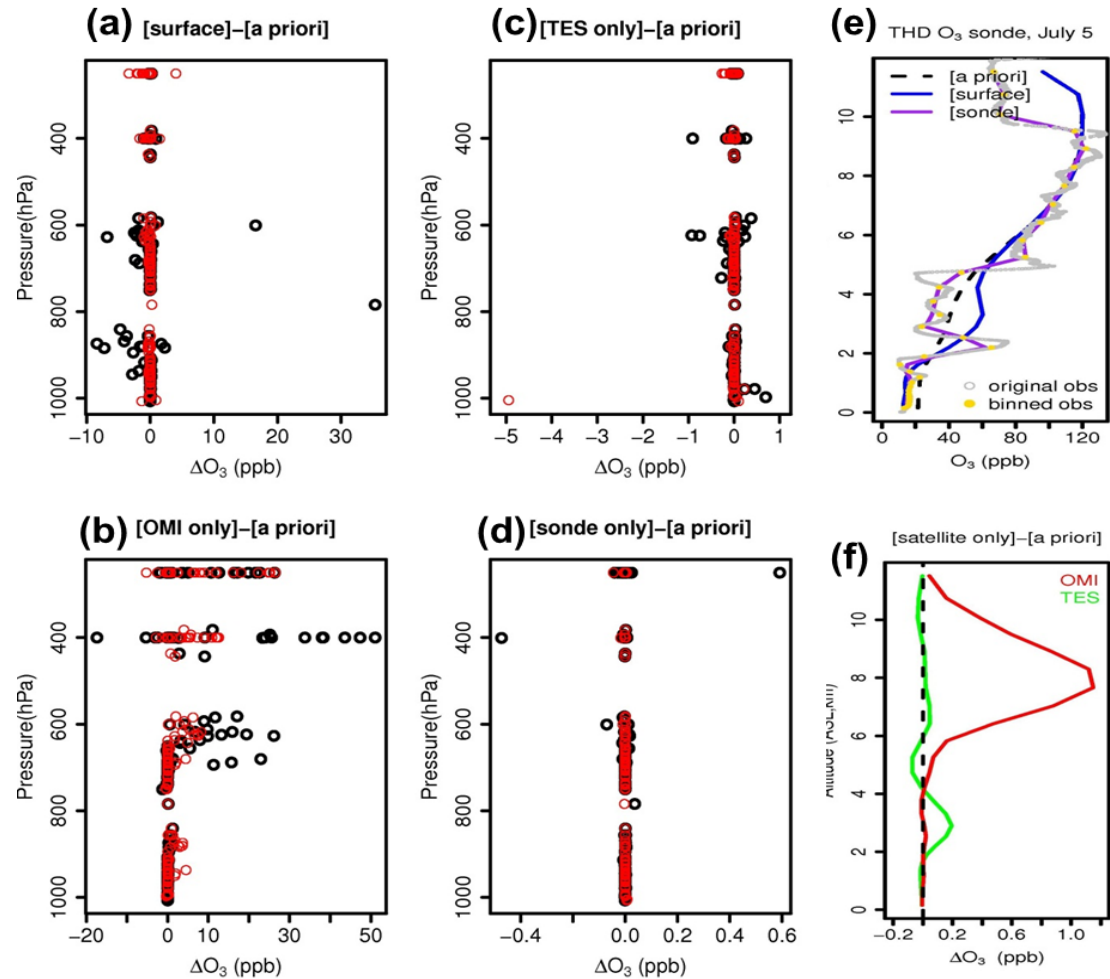


Figure 2.24 O₃ changes (assimilated fields-the *a priori*) at selected OMI sampling locations for (a) *Case AS*; (b) *Case AO*; (c) *Case AT*; (d) *Case AD*. In (a-d), black dots compare the raw data in OMI pressure grids and red dots compare the results after applying the OMI observation operator. (e) O₃ vertical profiles at THD on 5 July from sondes, STEM *a priori*, *Cases AS* and *AD*; (f) O₃ changes (assimilated fields-the *a priori*) at THD for *Cases AT* and *AO*.

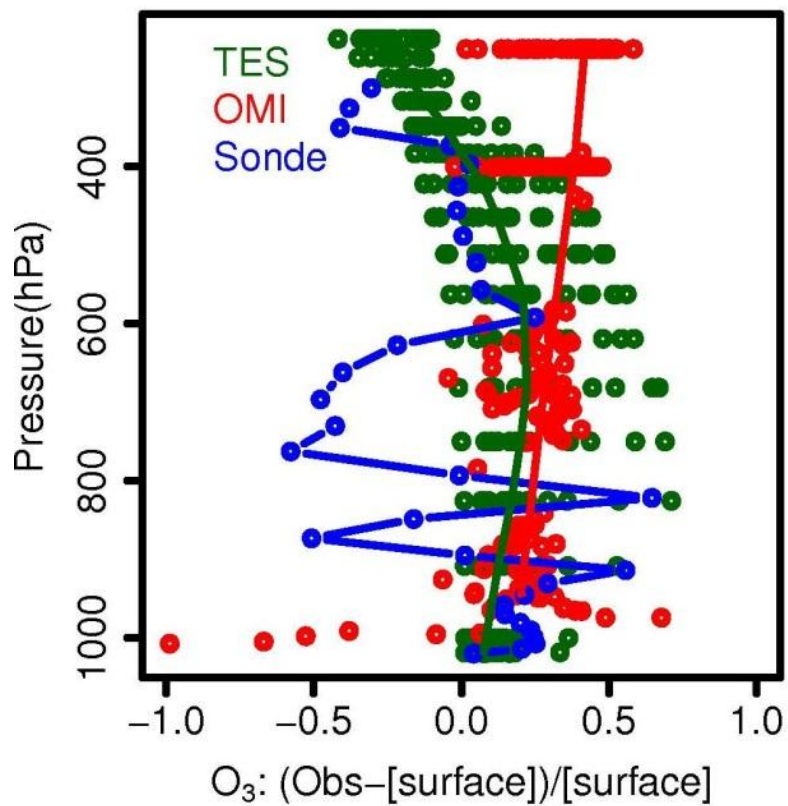


Figure 2.25 Comparison between measurements and the assimilated O₃ in the case the surface observations were assimilated.

CHAPTER 3
 SECTORAL AND GEOGRAPHICAL CONTRIBUTIONS TO SUMMERTIME
 CONTINENTAL UNITED STATES (CONUS) BLACK CARBON SPATIAL
 DISTRIBUTIONS

3.1 Introduction

Primary and secondary aerosols from local and distant sources influence climate (Intergovernmental Panel for Climate Change (IPCC), 2007) and adversely affect human health and visibility (US Environmental Protection Agency (EPA), 2011; United Nations Environment Programme (UNEP) and World Meteorological Organization (WMO), 2011). Their direct climate impact depends on the amounts of absorbing and scattering components. Black carbon (BC), generated from incomplete fossil-fuel and biomass combustion, absorbs light and has a positive direct radiative forcing (DRF). Most other aerosol components, such as sulfate (SO₄), nitrate (NO₃), and most organic carbon (OC) scatter light and have negative DRFs.

Since aerosols have short atmospheric lifetimes from hours to days (Chin et al., 2009), mitigating their emissions will result in rapid changes in their atmospheric concentrations and the associated health/climate impacts. Thus there is growing interest in developing aerosol-related policies that treat air pollution and climate change in the same framework (Ramanathan and Feng, 2008; Arneth et al., 2009). A better understanding of the sectoral contributions to the distributions of the absorbing and scattering components, and further consideration of the complication that both distant and nearby sources contribute to their health/climate impacts, will help inform these policies (Task Force on Hemispheric Transport of Air Pollution (HTAP), 2010; Heald et al., 2006; Brock et al., 2004; Fischer et al., 2010; Jaffe et al., 2005; VanCuren, 2003; NRC, 2009). Sector-based contributions to BC distributions and climate impacts have been studied using global models (*cf.* Shindell et al., 2008; Balkanski et al., 2010; Fuglestedt et al., 2007; Koch et al., 2007; Naik et al., 2007; Unger et al., 2009). However, these estimates involve

high uncertainties, due to the uncertainties in the regional and sectoral emissions, together with the uncertainties in other key model inputs, and those associated with model parameterizations and resolution (Koch et al., 2009; Textor et al., 2006). Therefore, there are needs to 1) conduct further studies over regions where observations are available to test and better constrain model estimates of BC distributions; and 2) to assess metrics that can help identify sectoral and regional contributions to climate impacts for use in screening mitigation options. For example, the ratio of BC to SO₄ over polluted Asian regions was found to be highly correlated with solar absorption efficiency (SAE=1-single scattering albedo (SSA)), with regression slopes that differed among plume types (Ramana et al., 2010). Such useful metrics provide a measure of the relative amounts of the most important absorbing aerosol component and the major scattering component (s), but need to be evaluated over other regions, as aerosol loading, composition and optical properties may vary among regions.

In this study we estimated sectoral contributions from local and distant sources to summertime BC distributions over the continental United States (CONUS), using a regional-scale chemical transport model and a recent global BC sectoral emission inventory. We used available aircraft and surface observations during this period to evaluate the model performance. Finally, the representativeness of several metrics was also evaluated that could help prioritize BC warming impacts on climate, and their sensitivities to reductions in sectoral emissions were calculated.

3.2 Data and methods

3.2.1 Study period and observational data

This study focused on a two-week period (13-26 June, 2008). A twenty-day period spanning from 1-20 April, 2008 is also included to discuss the seasonal differences between spring and summer (Section 3.3.7). Measurements from 150 IMPROVE (Interagency Monitoring of Protected Visual Environments) sites and 28 urban (Chemical Speciation Network (CSN) and

National Institute for Occupational Safety and Health (NIOSH) over CONUS on 14, 17, 20, 23, and 26 June were used to evaluate surface BC predictions (in this paper we consistently use BC instead of elemental carbon (EC) because the emission inventories were developed for BC, and we do not consider the differences caused by measurement methods). The vertical distributions of modeled BC were evaluated using the Single Particle Soot Photometer (SP2, Shiraiwa et al., 2007) BC measurements on NASA DC-8 aircraft during the California (CA) phase of the Arctic Research of the Composition of the Troposphere from Aircraft and Satellites (ARCTAS-CARB) experiment. These data were collected at daytimes of 20, 22 and 24 June, over southern CA, the CA-Mexico border, the Central Valley, and the eastern Pacific. Aircraft measurements of SO_4 , NO_3 and organic aerosol mass (OM) sampled using the Aerosol Mass Spectrometry (AMS, Dunlea et al., 2009) instrument, together with the green band (GB) aerosol SSA measured by the Langley Aerosol Research Group (LARGE, Thornhill et al., 2008) instrument suite and acetonitrile concentrations measured by the proton-transfer-reaction mass spectrometry (PTR-MS, Wisthaler et al., 2002), were also used to assess the representativeness of the BC/cooling aerosol ratios to aerosol warming potentials for different air-masses (e.g., low/high fire-impacted).

3.2.2 Model and input data

Model simulations were conducted using tracer and full-chemistry versions of the regional-scale Sulfur Transport and dEposition Model (STEM) version 2K3. The tracer domain used a 60×60 km polar stereographic grid, covering most of the northern hemisphere, and the full-chemistry domain was a subset of the tracer domain over the continental North America (NA). Further details were described in Huang et al. (2010a).

The tracer model calculated aerosol distributions of BC, SO_4 , primary OC, dust and sea salt (SS). Tagged CO tracers that focused on primary-emitted CO were also used to estimate the contributions of geographic source areas to the hemispheric-scale transport, including both anthropogenic (mainland US; Alaska; Canada; Greenland; Europe; Russia; China; and other Asia

nations) and biomass burning (NA, North Asia/Russia, and South Asia/Africa) tracers. The tracer simulations provided aerosol boundary conditions for the full-chemistry simulations and were used to correlate regional contributions with the BC sectoral contributions estimated by the forward sensitivity simulations described in Section 3.2.3.

The calculations were driven by meteorological fields generated by the Advanced Research Weather Research & Forecasting Model (WRF-ARW) (D'Allura et al., 2011), and used the anthropogenic sector (industry, power, residential, transportation, and global shipping) emissions from the recent bottom-up global $1^\circ \times 1^\circ$ gridded inventory developed by Q. Zhang and D. G. Streets (<http://www.cgrer.uiowa.edu/arctas/emission.html>) for the ARCTAS mission. The BC emissions over Asia were based largely on the NASA INTEX-B inventory (<http://mic.greenresource.cn/intexb-2006>), and over the CONUS were scaled from 1996 data to year of 2006 by Streets and Chin (Bond et al., 2004). The anthropogenic emissions of BC, SO₂ and OC by sector for NA and the rest of the northern hemisphere (non-NA) are summarized in Table 3.1 and the spatial maps Figure 3.1. For NA, BC emissions from transportation, residential and industry sectors account for ~60%, 19% and 18% of the anthropogenic emissions, respectively, while the residential sector accounts for ~50% of the non-NA emissions, with industry and transportation adding ~24-25% each. All anthropogenic sector emissions were distributed to the first two model layers (~100 m above ground level (AGL)) with a 7:3 ratio. Point and volcano SO₂ sources were injected up to 300-500 m AGL. Diurnal cycles were included when processing the emissions but no daily and seasonal variations were considered. Daily biomass burning total CO emissions were provided by the archived Real-time Air Quality Modeling System (RAQMS) (Pierce et al., 2007) with a 12-h temporal resolution, and were then unevenly distributed from surface up to ~5-6 km AGL, with nonlinear decreasing factors as the model height increased (0.12,0.12,0.11,0.101,0.101,0.096,0.083,0.082,0.082,0.074,0.018,0.013). The emission factors for hydrophobic BC and OC relative to CO were ~0.016 and 0.115, respectively. During this period, frequent fires with high emissions occurred over north Asia, eastern China, northern CA and southeastern US (Figure 3.1e-f).

The full-chemistry calculations also used the WRF meteorological fields and the same set of anthropogenic and biomass burning emissions as the tracer model. In addition, biogenic emissions of monoterpene and isoprene were taken from twelve-year-averaged values from the Orchidee model (Lathiere et al., 2006). Lateral boundary conditions (LBC) for thirty gaseous species and upper boundary conditions for ten gaseous species were downscaled from the RAQMS global real-time chemical analyses with a 6-h temporal resolution. The LBCs of BC, OC, dust, SS and SO₄ were from the STEM tracer results. The model treated emitted hydrophobic to hydrophilic BC and OC with ratios of 4:1 and 1:1, respectively, and both BC and OC were converted to hydrophilic with a fixed aging rate of $7.1 \times 10^{-6} \text{ sec}^{-1}$ (Cooke et al., 1996). Gas to particle conversion and water content of the inorganic aerosols were computed in four-bins (0.1-0.3 μm , 0.3-1.0 μm , 1.0-2.5 μm and 2.5-10.0 μm) by the Simulating Composition of Atmospheric Particles at Equilibrium (SCAPE) module (Kim and Seinfeld, 1995). The aerosol dry deposition rates were scaled to sulfate deposition dependent on meteorological fields and land cover, and wet scavenging was modeled as a loss rate that varied with precipitation rate, only applied to hydrophilic aerosols.

3.2.3 Forward sensitivity analysis

The impacts of the NA and extra-regional (interchangeable with non-NA in this paper) sector emissions on CONUS BC distributions were estimated by the base simulation and eleven forward sensitivity simulations where the sector emissions were perturbed. To estimate contributions from the NA emission sources, sector emissions of BC, OC and SO₂ from inside of the full-chemistry model domain were set to zero while the LBCs were unchanged (i.e., no changes in non-NA emissions). The contributions from extra-regional sector emissions were estimated by zeroing out sector emissions in the hemispheric tracer model and using these results as LBCs in the full-chemistry simulations where the NA emissions were not perturbed. The changes in aerosol distributions due to the perturbations in emissions had feedbacks to photolysis rates and heterogeneous chemistry, but not to the meteorological fields. In addition, we

performed simulations in which the emissions from two selected sectors were perturbed by 20%, and found that the sensitivities of BC surface concentrations and column amounts to the emission perturbations were close to linear (Figure 3.2).

3.3 Results and discussions

3.3.1 Model base case and its evaluation

3.3.1.1 Base case

Figure 3.3a-c presents the mean simulated BC surface concentrations, total columns and vertical profiles over the ten EPA regions (<http://www.epa.gov/tp/whereyoulive/regions.htm>, Figure 3.3d) in the base case. The BC surface concentrations are important for assessing health impacts, and the vertical distributions and column amounts are useful for assessing climate impacts. The modeled BC surface concentrations and columns are in the ranges of $\sim 0.05\text{--}3 \mu\text{g}/\text{m}^3$ and ~ 0.2 to $\sim 5 \text{ mg}/\text{m}^2$, with the nation-wide averages of $\sim 0.2 \mu\text{g}/\text{m}^3$ and $\sim 1.1 \text{ mg}/\text{m}^2$, respectively. The mean surface concentration is at the higher bound of the simulated NA BC in June 2001 by six global models (HTAP, 2010), and the column amounts fall within the range summarized by Schuster et al. (2005). The eastern US (especially the northeastern US and the Lake Michigan areas) shows higher modeled surface concentrations and total column amounts than over most parts of the western US, except northern CA which was heavily affected by the local wildfires during this period. The four-corner region in the southwest shows the lowest values ($< 0.4 \mu\text{g}/\text{m}^3$ and $< 0.8 \text{ mg}/\text{m}^2$). Most of the BC mass is below $\sim 4\text{--}5$ km above sea level (ASL) (i.e., showing a $\sim 4\text{--}5$ km scale height (the altitude at which the concentration is $1/e$ of that at surface, which is an important input for some radiative transport models)) (Figure 3.3c). Above 4-5 km, Region 10 shows the highest BC levels, reflecting the influences by extra-regional sources.

3.3.1.2 Evaluation at urban and remote surface sites

Comparisons between observed and modeled BC are shown in Figure 3.4a-d, at 150 IMPROVE sites and 28 urban sites that had all five days of BC measurements over the CONUS domain. Table 3.3 summarizes the statistics of model evaluation at these sites. The observed BC at urban locations is overall ~2.5 times higher than at rural/remote sites and displays larger standard deviation (SD). Both the observed and modeled BC at IMPROVE sites show higher values over the western and eastern US than the mountain regions, and overall the model captures these gradients fairly well, with slight over-prediction over the mountain regions and negative biases over the eastern US and CA. The BC concentrations at urban locations are generally under-predicted (with a mean bias (mean modeled-observed) of $-0.24 \mu\text{g}/\text{m}^3$) due to the coarse model resolution and uncertainties in the fire emissions. The spatial variability reflected by SD is under-predicted at IMPROVE and urban locations by 30% and 50%, respectively.

The model performance for BC varies by individual EPA region. At IMPROVE sites, lower correlations are shown over Regions 4, and 7-10, again reflecting the uncertainties from fire emissions and extra-regional contributions. Mean biases range from $-0.17 \mu\text{g}/\text{m}^3$ (Region 4) to $0.32 \mu\text{g}/\text{m}^3$ (Region 1), and root mean square errors (RMSE) are highest in Regions 1, 4 and 9. Mean fractional bias (MFB, equation 3.1) and mean fractional error (MFE, equation 3.2) at most EPA regions are below 70%.

$$\text{Mean fractional bias (MFB)} = \text{Mean} (2 \times (\text{modeled} - \text{observed}) / (\text{modeled} + \text{observed})) \quad (3.1)$$

$$\text{Mean fractional error (MFE)} = \text{Mean} (2 \times |(\text{modeled} - \text{observed}) / (\text{modeled} + \text{observed})|) \quad (3.2)$$

3.3.1.3 Evaluation along DC-8 flight paths

Predicted BC was compared to the NASA DC-8 flight observations on 20, 22 and 24 June. Modeled BC was extracted at identical locations as the flight samples using spatial and temporal interpolation. The modeled and observed BC concentrations from all flights were binned vertically every 500 m and the resulting vertical distributions are presented in Figure

3.4e. Observations show three major features with mean concentrations of $\sim 0.2 \mu\text{g}/\text{m}^3$ below 500 m, $\sim 0.3 \mu\text{g}/\text{m}^3$ at 1-1.5 km, and $\sim 0.2 \mu\text{g}/\text{m}^3$ at 3.5-4 km. The multiple levels and large variability in BC concentrations indicate impacts from various sources. The model captures the vertical features fairly well, with over-predictions at the surface and >4 km. Correlations between modeled and observed BC for each of the three flights are 0.2, 0.5 and 0.1, respectively. The lower correlations for the 20 and 24 June flights reflect the model's incapability of capturing the variability over LA and the Central Valley due to its coarse horizontal resolution (relative to the speed of DC-8 at ~ 14 km/minute). Correlations are highest for the 22 June flight that sampled over broad CA regions. Other statistical analyses for the three flights show mean biases of -0.04, 0.21 and $0.02 \mu\text{g}/\text{m}^3$ and the RMSE of 0.22, 0.52 and $0.34 \mu\text{g}/\text{m}^3$, respectively, and the largest positive biases occur at the northern CA fire locations.

Compared to global model performance summarized by Koch et al. (2009), the STEM performance is reasonably good (i.e., seventeen global models over-predicted BC at NA surface and along flight tracks in several field campaigns over tropical/mid-latitude regions, with the mean modeled/observed BC ratios of 1.6 and 7.9, respectively, while the mean modeled/observed BC burden over NA from these models was 0.42.)

3.3.2 Sector contributions to CONUS BC distributions

3.3.2.1 Contributions to surface/column distributions and vertical profiles

The two-week mean NA and extra-regional sector contributions to the US surface BC are presented in Figures 3.5 and 3.6, respectively. Overall, the top contributing anthropogenic sectors are transportation, residential, and industry (up to ~ 0.2 - $0.3 \mu\text{g}/\text{m}^3$), and fire emissions strongly impacted surface BC over CA ($>1 \mu\text{g}/\text{m}^3$) and southeastern US (up to ~ 0.3 - $0.4 \mu\text{g}/\text{m}^3$). The contributions from the power and shipping sectors are small ($<0.04 \mu\text{g}/\text{m}^3$), with the shipping emissions only impacting the coastal areas. The transported plumes enter the US from the northwest during the studied period, where the contributions to surface BC range from 0.1 to

$0.2 \mu\text{g}/\text{m}^3$, decreasing from the northwest to southeast US ($0.01\text{-}0.04 \mu\text{g}/\text{m}^3$). Among the extra-regional emission sectors, the largest anthropogenic contributors are residential (up to $\sim 0.04 \mu\text{g}/\text{m}^3$), transportation (up to $0.025\text{-}0.04 \mu\text{g}/\text{m}^3$), and industry (up to $0.025\text{-}0.04 \mu\text{g}/\text{m}^3$). Impacts from power emissions are much lower ($<0.002 \mu\text{g}/\text{m}^3$). Extra-regional fire emissions show higher impacts than the individual non-NA anthropogenic emission sectors (up to $\sim 0.08\text{-}0.1 \mu\text{g}/\text{m}^3$) over the eastern Pacific and the northwest.

The stacked mean contributions from eleven emission sectors to CONUS surface and column BC, averaged over the ten EPA regions are shown in Figure 3.7a and 3.7b, respectively. The numbers below each stacked bar indicate the base case results for the corresponding region. The surface concentrations range from $0.15 \mu\text{g}/\text{m}^3$ (Region 8) to $0.47 \mu\text{g}/\text{m}^3$ (Region 1) and column amounts range from $0.76 \text{mg}/\text{m}^2$ (Region 6) to $1.45 \text{mg}/\text{m}^2$ (Region 1). The sum of contributions from all sectors for each region shows a 5%-15% loss due to the averaging processes and the exchanges between regions and with Mexico and Canada (included in the full-chemistry domain but not belonging to the EPA regions). Overall, NA transportation and extra-regional residential sectors are the major anthropogenic contributors to surface and column BC. The contributions from NA emissions to column BC are lower than those to surface BC, indicating that the impacts of transported plumes increase with altitude. The sectoral contributions vary among regions. Regions 8 and 10 receive the largest contributions from extra-regions ($\sim 40\text{-}60\%$ at surface and $>60\%$ for column), while the rest of the regions are dominated by NA emissions. NA biomass burning strongly impact Regions 4 and 9 ($\sim 30\text{-}50\%$ at surface and for column), and extra-regional biomass burning BC accounts more than half of the extra-regional BC in Regions 8 and 10.

Figure 3.7c shows the sectoral contributions to the BC vertical distribution averaged over the CONUS domain. The NA sectors (mainly biomass burning and transportation) are the major contributors below ~ 5 km. The non-NA emissions dominate the BC distribution above ~ 5 km, but also contribute $\sim 25\%$ to the mean surface concentration.

To further estimate the importance of extra-regional BC, we calculated the spatial correlations between modeled surface BC concentrations (NA anthropogenic and NA anthropogenic + extra-regional total) and US anthropogenic emissions (Table 3.4), and the temporal correlation between modeled surface BC and column BC amounts (Figure 3.8a). The modeled anthropogenic NA concentrations show correlations with anthropogenic emissions >0.65 , mostly >0.8 . After we added the modeled extra-regional BC contributions into the correlation calculations, the values dropped (except Region 5) by 0.02-0.33, due to the modifications of BC distributions by the transported plumes. The largest changes (-0.33) occur at Region 8 (mountain regions), indicating that this region is most sensitive to the transported plumes, because of its complex topography and lower local emissions. Region 10 follows Region 8 and shows a decrease in correlation of 0.09. Figure 3.8a depicts the temporal correlations between modeled surface and column BC over CONUS during the period. The eastern Pacific, coastal Oregon, Washington, Utah, Colorado and urban regions in EPA Region 9 (such as LA and Phoenix) show the lowest correlations ($<\pm 0.1$), indicating that the boundary layer and free troposphere are influenced by different emissions sources/processes. There are broad regions with high correlations, which may be generally influenced dominantly by either NA or non-NA sources.

We also compared the extra-regional estimates of BC obtained through the sector-based analysis with the estimates using the regional CO tracers. Shown in Figure 3.8b are the ratios of the extra-regional tracer CO (%) to the extra-regional BC contributions (%) at surface and their spatial correlations during the study period for the ten EPA regions. The large-scale features of the estimates are similar, reflected by the high spatial correlations between the two (>0.7). The highest correlations are in Regions 5, 8-10 (>0.94), and the lowest are in Regions 2, 3 and 7 ($\sim 0.7-0.8$). The extra-regional contributions based on tracer CO are higher than those for BC (ratios >1), mainly due to the differences in their lifetimes and emission characteristics over NA and extra-regions. The ratios increase as the travel distances increase (e.g., Regions 1-4 $>$ Regions 8-10).

3.3.2.2 Evaluation of the extra-regional BC contributions

VanCuren (2003) conducted composition analysis of Asian aerosols for March-October, 1989-1999 at multiple IMPROVE sites in western US. He found that a mixture of dust and combustion products dominated the Asian aerosols with typical concentration around $5 \mu\text{g}/\text{m}^3$ and mass median diameter between 2 and $3 \mu\text{m}$. BC accounted for ~4% of the fine particles ($\sim 0.1 \mu\text{g}/\text{m}^3$). Model simulations by Park et al. (2003) reported that the contributions from non-US sources to US BC in 1998 were $0.06 \mu\text{g}/\text{m}^3$ over both western and eastern US (0.04 and $0.02 \mu\text{g}/\text{m}^3$ from natural and anthropogenic sources, respectively). Six global models estimated the non-NA source contributions to the annual mean NA surface BC concentrations in 2001 (HTAP, 2010), showing the range of 0.8-45.5% with the median value of 20.9%. Our study generated a mean non-NA contribution (biomass burning+anthropogenic) to CONUS surface BC of $\sim 0.05 \mu\text{g}/\text{m}^3$ (~20% of total), with the maximum of $\sim 0.11 \mu\text{g}/\text{m}^3$ in Region 10. These values are close to these previous studies, but with a higher spatial variability than Park et al. (2003).

Murphy et al. (2011) analyzed the observed BC at IMPROVE sites during 1990-2004 and indicated that BC concentrations decreased over most regions in summertime except the mountain regions due to the wildfires. However, our results for a low fire-impacted summer period over the mountain regions show that the trend of extra-regional emissions (Lu et al., 2011) may also play a role in this trend. This is similar as Jaffe et al.'s (2007, 2008) suggestion that the summertime western US fires together with regional emissions and global background are responsible for the increase in summertime ozone over the western US.

3.3.3 Using metrics to prioritize climate impacts of sector emissions

3.3.3.1 Evaluate metrics to prioritize climate impacts

A previous study over Asia found that BC/SO₄ ratios were highly correlated with GB SAE (i.e., 550 nm) (Ramana et al., 2010). The SAE indicates aerosols' warming potential:

Empirical values for warming and cooling aerosol plumes are >0.15 and <0.05 , respectively, and

for values between 0.05 and 0.15, the aerosols' climate impact depends on the surface and cloud properties, atmosphere vertical profile, location and season (Bond and Bergstrom, 2006). We used the 24 June DC-8 observations to evaluate the correlation between the BC and cooling aerosol ratios and the GB SAE (i.e., 532 nm) over CA. The sampling locations where aerosol, acetonitrile and SAE measurements were made are mostly below 3 km, over southern CA and the CA-Mexico border cloud-free regions (Figure 3.9a). The calculated BC source contributions at these locations are shown as boxplots every 500 m in Figure 3.9b. The sampled regions are mostly affected by NA anthropogenic (AN) and biomass burning (BB) emissions (sums of both are >80% at most altitudes), but are also influenced by extra-regional sources, with their contributions increasing with altitudes. Figure 3.9c-d show the scatterplots between the BC and cooling aerosol ratios (i.e., $BC/(OM+NO_3+SO_4)$, and BC/SO_4) and the GB SAE, colored by measured BC and acetonitrile, respectively. Measured SAE ranges from ~0 to 0.2, and the samples with $BC > 0.2 \mu g/m^3$ show $SAE > 0.05$. Fire-impacted samples (defined in this study as those with acetonitrile >0.2 ppb, as the median of the measured acetonitrile that we used is ~0.23 ppb at these locations) have SAE values in the 0.05-0.1 range, while the anthropogenic plumes indicate higher warming potential with SAE values up to ~0.2. The oceanic samples are mostly unaffected by fires and have lower BC concentrations and SAE. The ratios of $BC/(OM+SO_4+NO_3)$ are highly correlated with SAE for both terrestrial and oceanic samples (0.74 over land and 0.72 over ocean). The BC/SO_4 ratio shows negative correlation with SAE for the high fire-impacted air-masses, but positive correlation for the low fire-impacted plumes. Table 3.5 summarizes the correlations of SAE with several ratios. These results indicate that $BC/(OM+NO_3+SO_4)$ can fairly well represent their net warming potential over the LA region. It can be approximated by $BC/(OM+SO_4)$ and BC/OM (as OM accounts for >~70 % of the sum of $OM+NO_3+SO_4$ aerosols, Figure 3.9c inner panels). For the low-fire impacted plumes, the representativeness of $BC/(OM+SO_4)$ is slightly better than BC/OM . BC/SO_4 is also a good metric for plumes unaffected by fires.

3.3.3.2 BC/(SO₄+OM) and BC/SO₄ sensitivity to sector emissions

Using the ratios of BC/(SO₄+OM) and BC/SO₄ as metrics to represent the impacts of aerosol mixture on DRF for fire-impacted and non-fire-impacted scenarios, respectively, we calculated their responses to removing sector emissions for the ten EPA regions. To calculate the BC/SO₄ ratios in the base and non-anthropogenic sector emission cases, we subtracted the contributions from NA and non-NA biomass burning from each sensitivity case, and ignored any non-linear impacts on SO₄. The modeled BC and SO₄ were scaled with observed/modeled BC and SO₄ at the IMPROVE sites for each region, and modeled OC was converted to OM using 1.8× observed OC/modeled OC (1.8 came from “Key to Monitoring-Modeling-Emissions Mapping”, 2008, <http://vista.cira.colostate.edu/docs/AirData/Methods/>) (scaling factors are given in Table 3.6). This scaling approach assumes that: 1) the biases in each sector are the same as those in the base case in each region; 2) biases determined by the five-day measurements represent the two-week period; 3) biases determined by observations at sparse sites in each EPA region represented the entire corresponding region.

The ratios in the base case and their percent changes relative to the base case ratios after removing various emission sectors are summarized in Tables 3.7 and 3.8 for BC/(SO₄+OM) and BC/SO₄, respectively. Both ratios indicate that power and shipping sectors have net cooling impacts (positive changes) and transportation sectors are net warming, with the NA power and transportation sectors the largest cooling and warming sectors, respectively. As the transportation sector contributes most to the surface and column BC among the NA anthropogenic emission sectors (Section 3.3.2.1), controlling emissions from this sector can efficiently reduce BC concentrations and the aerosol warming potentials over the CONUS.

Previous studies have discussed the impacts of sector emissions on radiative forcing and climate change. They found that controlling BC+OM from fossil fuel combustion can slow warming (Jacobson, 2002), while biomass burning had short-term cooling effects (Jacobson, 2004; Naik et al., 2007). Among the anthropogenic emission sectors, transportation emissions showed positive forcing while industry and power sector emissions contributed negative forcing

(Shindell et al., 2008). Residential emissions resulted in weak cooling effects over CONUS except over northwestern US (Koch et al., 2007). The metrics we analyzed agreed well with previous findings for transportation, power, and biomass burning sectors. BC/(OM+SO₄) and BC/SO₄ showed discrepancies in representing residential and industry sectors, and they were consistent with Koch et al. (2007)'s results for residential and industry sectors, respectively.

3.3.4 Seasonal variations of extra-regional pollution and NA fires contributions

A base case and eleven forward sensitivity simulations spanning from April 1st to 20th were conducted to compare BC contributions from various NA and extra-regional sectors with the summertime simulations. As the anthropogenic emissions did not include seasonal variations, the NA BC sector contributions show similar gradients and magnitudes as the summertime. Major differences are found in extra-regional sectors and the NA biomass burning sector, due to the different synoptic conditions and biomass burning emissions between spring and summertime (Figure 3.1). During this spring study period, large biomass burning emissions occurred in EPA Regions 4-7, contributing up to 0.3-0.5 $\mu\text{g}/\text{m}^3$ of surface BC (Figure 3.10b). These values were much lower than the contributions from summertime northern CA wildfires (Figure 3.5a). Extra-regional BC contributed up to 60 % of surface BC at EPA Regions 8, 9, 10, and up to 70 % of column BC over these regions (not shown). The transported plumes heavily impacted CA, contributing $\sim 0.2 \mu\text{g}/\text{m}^3$ of surface BC. Strong impacts ($>0.1 \mu\text{g}/\text{m}^3$) extended to -105°W , and southeastern US was weakly impacted ($<0.05 \mu\text{g}/\text{m}^3$).

3.4 Conclusions and suggestions on future work

We calculated the contributions of various anthropogenic and biomass burning sector emissions to BC surface/vertical distributions and column amounts in summer 2008 over ten EPA regions. Over 80% of the surface BC concentrations were dominated by NA emissions except for Regions 8 and 10, and the non-NA emissions contributed to 30-80% of column BC depending on region. NA fires were important during this period in northern CA and

southeastern US, and NA transportation sector was the largest anthropogenic contributor in general. The mean non-NA contribution to surface BC was $\sim 0.05 \mu\text{g}/\text{m}^3$, with a maximum value of $\sim 0.11 \mu\text{g}/\text{m}^3$ in Region 10. Residential, transportation and biomass burning were the major non-NA contributors.

The representativeness of BC to cooling aerosol mass ratios to their warming potential (SAE) were evaluated using the 24 June DC-8 flight observations during the ARCTAS-CARB field campaign. BC/OM , $\text{BC}/(\text{OM}+\text{SO}_4)$ and $\text{BC}/(\text{OM}+\text{SO}_4+\text{NO}_3)$ correlated well with SAE and BC/SO_4 only correlated well with SAE for the low-fire impacted plumes. Forward sensitivity calculations suggested that reducing emissions from NA transportation sector is likely to have highest co-benefits for air quality and climate change. Further research is needed to evaluate the utility of these (and other) metrics over broad geographical regions, and to extend the analysis to include sector-based NO_x emissions perturbations.

There were still uncertainties associated with the sectoral/regional contribution estimates. Uncertainties were mainly resulted from the emission inventory ($\pm 208\%$ uncertainty over China, with much lower uncertainty for the power sector than the others (Zhang et al., 2009)), and from the uncertainty in estimating transport processes in the complex topography in Regions 8-10. Three-dimensional observations are useful to constrain BC distributions, improve emission estimates, and to improve estimates of sector-based NA and extra-regional contributions. Combining these observations with modeling studies using an appropriate resolution will help reduce these uncertainties.

Table 3.1 Anthropogenic emissions and several emission ratios by sector

Emission Sectors	24-hour average emissions						Ratios (dimensionless)					
	BC NA	BC non-NA	OC NA	OC non-NA	SO ₂ NA	SO ₂ non-NA	BC/SO ₂ mass NA	BC/SO ₂ mass non-NA	BC/OC NA	BC/OC non-NA	BC/(SO ₂ +OC) NA	BC/(SO ₂ +OC) non-NA
Anthropogenic total (molec./cm²/s)	1.83E+09	5.16E+09	2.70E+09	9.86E+09	1.56E+10	2.06E+10	2.20E-02	4.71E-02	6.79E-01	5.23E-01	2.14E-02	4.32E-02
Industry (%)	18.42	24.61	8.85	11.87	27.63	33.50	1.46E-02	3.45E-02	1.41E+00	1.08E+00	1.45E-02	3.34E-02
Power (%)	1.81	1.64	1.90	0.64	44.29	47.62	8.98E-04	1.61E-03	6.44E-01	1.34E+00	8.97E-04	1.61E-03
Residential (%)	18.80	49.22	64.44	80.12	5.90	7.28	7.01E-02	3.18E-01	1.97E-01	3.22E-01	5.17E-02	1.60E-01
Transportation (%)	59.02	24.03	20.59	6.70	10.19	6.02	1.27E-01	1.88E-01	1.94E+00	1.88E+00	1.19E-01	1.71E-01
Shipping (%)	2.27	0.48	4.15	0.67	11.92	5.39	4.20E-03	4.20E-03	3.73E-01	3.73E-01	4.15E-03	4.15E-03

Table 3.2 Total anthropogenic (terrestrial+shipping) emissions and emission ratios by regions ^a

Regions	BC (Gg)	OC (Gg)	SO ₂ (Gg)	BC/ (OC+SO ₂)	BC/OC	BC/SO ₂	Regions	BC (Gg)	OC (Gg)	SO ₂ (Gg)	BC/ (OC+SO ₂)	BC/OC	BC/SO ₂
Canada	45	62	1806	0.02	0.73	0.02	Former USSR	152	189	12646	0.01	0.80	0.01
USA	352	502	14317	0.02	0.70	0.02	Middle East	189	141	5331	0.03	1.34	0.04
Central America	140	223	2509	0.05	0.63	0.06	South Asia	525	1566	8595	0.05	0.34	0.06
South America	335	555	5991	0.05	0.60	0.06	East Asia	1886	3354	32221	0.05	0.56	0.06
Northern Africa	85	64	966	0.08	1.32	0.09	Southeast Asia	378	1537	5180	0.06	0.25	0.07
Western Africa	261	921	824	0.15	0.28	0.32	Oceania	38	30	3289	0.01	1.27	0.01
Eastern Africa	94	321	115	0.22	0.29	0.82	Japan	51	21	806	0.06	2.39	0.06
Southern Africa	149	388	3903	0.03	0.38	0.04	Greenland	0	0	0			
OECD Europe	334	289	7174	0.04	1.16	0.05	Antarctica	0	0	0			
Eastern Europe	129	253	4590	0.03	0.51	0.03	International Shipping	58	156	13854	4.15e-3	0.37	4.2e-3
Global total	5200	10572	124118	3.86e-2	0.49	4.19e-2							

^a Source: <http://www.cgrer.uiowa.edu/arctas/emission.html>

Table 3.3 Statistical evaluation of modeled summertime BC at surface sites, summarized by EPA regions ^{a,b}

	RG1	RG2	RG3	RG4	RG5	RG6	RG7	RG8	RG9	RG10	All IMPROVE sites	All urban sites
Observation, mean $\pm\sigma$	0.27 \pm 0.10	0.30	0.47 \pm 0.27	0.46 \pm 0.53	0.18 \pm 0.10	0.15 \pm 0.08	0.16 \pm 0.05	0.08 \pm 0.04	0.37 \pm 0.33	0.12 \pm 0.12	0.24 \pm 0.27	0.60 \pm 0.38
Bias, mean/ σ	0.32/0.2 0	-0.03	-0.15/ -0.19	-0.17 /-0.43	0.01/ -0.02	0.02/ -0.01	0.10/0.0 2	0.07/0.0 1	-0.12/ -0.12	0.14/ -0.03	0.02/-0.08	-0.24/ -0.19
Mean Error	0.32	0.03	0.16	0.19	0.04	0.04	0.10	0.07	0.24	0.15	0.15	0.28
Correlation r	0.88	NA	0.70	0.41	0.82	0.77	0.50	0.24	0.13	0.67	0.30	0.27
Mean Fractional Bias	0.66	-0.12	-0.30	-0.18	0.10	0.15	0.46	0.55	-0.25	0.91	0.25	-0.42
Mean Fractional Error	0.67	0.12	0.31	0.28	0.24	0.22	0.47	0.57	0.64	0.94	0.54	0.53
Root Mean Square Error	0.39	0.03	0.25	0.50	0.05	0.05	0.11	0.09	0.38	0.17	0.27	0.44
Number of sites	13	1	8	13	11	11	12	31	32	18	150	28

^a Results are in $\mu\text{g}/\text{m}^3$ except correlation r and the number of sites;

^b The statistics by EPA region refer to the IMPROVE sites; there are too few numbers of urban sites with observations in each EPA region for statistics.

Table 3.4 Correlation r between emissions and BC concentrations, summarized by EPA regions

	RG1	RG2	RG3	RG4	RG5	RG6	RG7	RG8	RG9	RG10
r (anthropogenic BC emissions vs. modeled NA anthropogenic BC)	0.95	0.92	0.93	0.82	0.67	0.80	0.85	0.83	0.88	0.88
r (anthropogenic BC emissions vs. modeled NA anthropogenic BC + non-NA BC)	0.95	0.92	0.93	0.74	0.70	0.76	0.83	0.50	0.84	0.79
Degradation in r by extra-regional plumes	~0	~0	~0	-0.08	0.03	-0.04	-0.02	-0.33	-0.04	-0.09

Table 3.5 Correlations between BC/cooling aerosols and SAE^a along the 24 June DC-8 flight

Ratios	BC/(OM+SO ₄ +NO ₃)	BC/(OM+SO ₄)	BC/OM	BC/SO ₄
High fire-impacted ^b	0.76	0.78	0.78	-0.04
Low fire-impacted ^b	0.78	0.78	0.76	0.77

^a SAE=1-single scattering albedo, green band (~532 nm)

^b High-fire: acetonitrile >0.2 ppb; Low-fire impacted: acetonitrile ≤0.2 ppb. Median of measured acetonitrile was ~0.23 ppb.

Table 3.6 Aerosol scaling factors by EPA regions ^a

	RG1	RG2	RG3	RG4	RG5	RG6	RG7	RG8	RG9	RG10
BC	0.53	1.13	1.43	1.57	0.94	0.89	0.65	0.60	1.73	0.42
SO ₄	0.54	0.69	0.67	0.69	0.65	0.87	0.57	0.68	1.38	0.46
OM	2.18	3.55	4.57	4.51	4.52	5.34	4.32	4.09	7.11	1.67

^a Scaling factors for BC and SO₄ were determined by regional mean(observed/modeled); Scaling factors for OM were determined by regional mean (observed OC×1.8/modeled OC).

Table 3.7 Base case BC/(SO₄+OM) ratios and the responses in ratios to removing emission sectors, by EPA regions.

Cases	RG1	RG2	RG3	RG4	RG5	RG6	RG7	RG8	RG9	RG10	
Base ($\times 10^{-2}$)	5.36	6.31	5.51	5.55	5.29	3.29	4.64	3.54	4.23	4.77	
Changes in %	no NA biomass burning	3.91	4.85	7.54	16.66	7.10	15.88	8.34	8.22	50.35	8.07
	no NA industry	-5.74	-4.74	-2.86	-0.15	-1.85	2.89	-1.37	-3.60	-3.95	-4.79
	no NA power	25.87	27.51	26.10	15.68	13.12	14.38	10.29	2.98	0.38	0.20
	no NA residential	16.15	12.87	4.83	0.40	4.98	-0.51	4.30	1.11	1.41	-1.07
	no NA transportation	-44.16	-42.09	-36.59	-26.61	-39.62	-32.12	-42.33	-24.34	-14.02	-16.25
	no shipping	1.68	0.65	0.44	1.98	0.42	3.28	0.83	1.46	1.17	1.75
	no non-NA biomass burning	1.48	1.61	1.62	0.97	10.91	2.53	16.81	21.52	2.24	14.48
	No non-NA industry	0.26	-0.06	-0.60	-0.67	-0.10	-0.22	0.40	0.07	-0.47	1.13
	no non-NA power	1.48	1.49	1.49	1.49	4.00	1.90	4.71	8.95	2.74	13.55
	no non-NA residential	-0.28	-0.61	-1.21	-1.36	-0.89	-0.93	-0.01	-2.23	-1.66	-4.22
	no non-NA transportation	-0.65	-1.00	-1.61	-1.65	-2.70	-1.42	-2.54	-5.04	-2.07	-6.12

Table 3.8 Base case BC/SO₄ ratios and the responses in ratios to removing emission sectors, by EPA regions. The NA biomass burning and non-NA biomass burning contributions were subtracted from each case before the calculations.

Cases	RG1	RG2	RG3	RG4	RG5	RG6	RG7	RG8	RG9	RG10	
Base	0.11	0.13	0.10	0.11	0.13	0.07	0.13	0.10	0.17	0.10	
Changes in %	no NA industry	5.83	7.70	6.53	12.83	13.53	22.61	13.58	0.36	-1.17	-6.94
	no NA power	73.68	87.59	86.32	72.43	53.71	49.98	44.35	12.80	4.53	0.80
	no NA residential	-10.26	-12.49	-12.29	-11.46	-10.59	-12.62	-9.20	-7.04	-8.99	-8.89
	no NA transportation	-47.97	-47.36	-45.34	-43.52	-47.44	-41.62	-50.50	-33.55	-31.82	-26.62
	no shipping	3.34	1.35	0.96	6.27	1.18	8.65	2.56	5.38	12.98	5.94
	No non-NA industry	1.10	0.78	-0.03	-0.01	3.98	0.94	6.03	13.25	12.51	17.69
	no non-NA power	3.13	3.33	3.45	4.79	13.17	5.12	17.13	43.46	33.77	65.79
	no non-NA residential	-0.92	-1.54	-2.86	-3.86	-4.27	-2.82	-4.04	-9.25	-5.27	-13.62
	no non-NA transportation	-0.63	-1.05	-1.96	-2.62	-2.89	-1.81	-2.59	-5.81	-3.23	-8.63

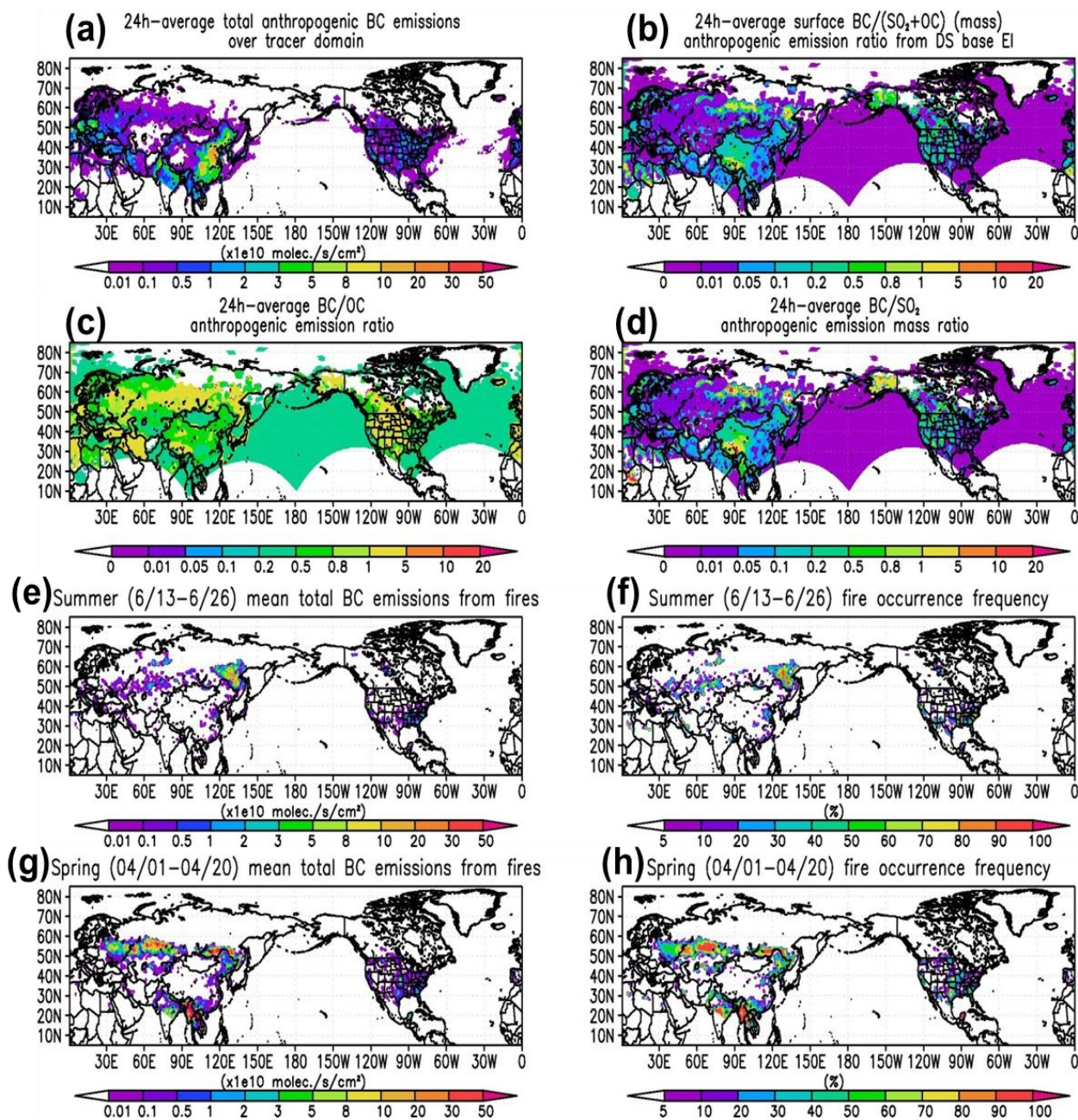


Figure 3.1 (a) 24-h average total anthropogenic emissions over tracer hemispheric domain; (b) 24-h average total anthropogenic BC/(SO₂+OC) emission mass ratios; (c) 24-h average total anthropogenic BC/OC emission mass ratios; (d) 24-h average total anthropogenic BC/SO₂ emission mass ratios; (e) Mean total BC emissions from biomass burning; (f) Fire occurrence frequency. The fire occurrence frequency is defined as the number of days that the fire emissions > 0 / total days in the study period (i.e., 14 days), reported in %.

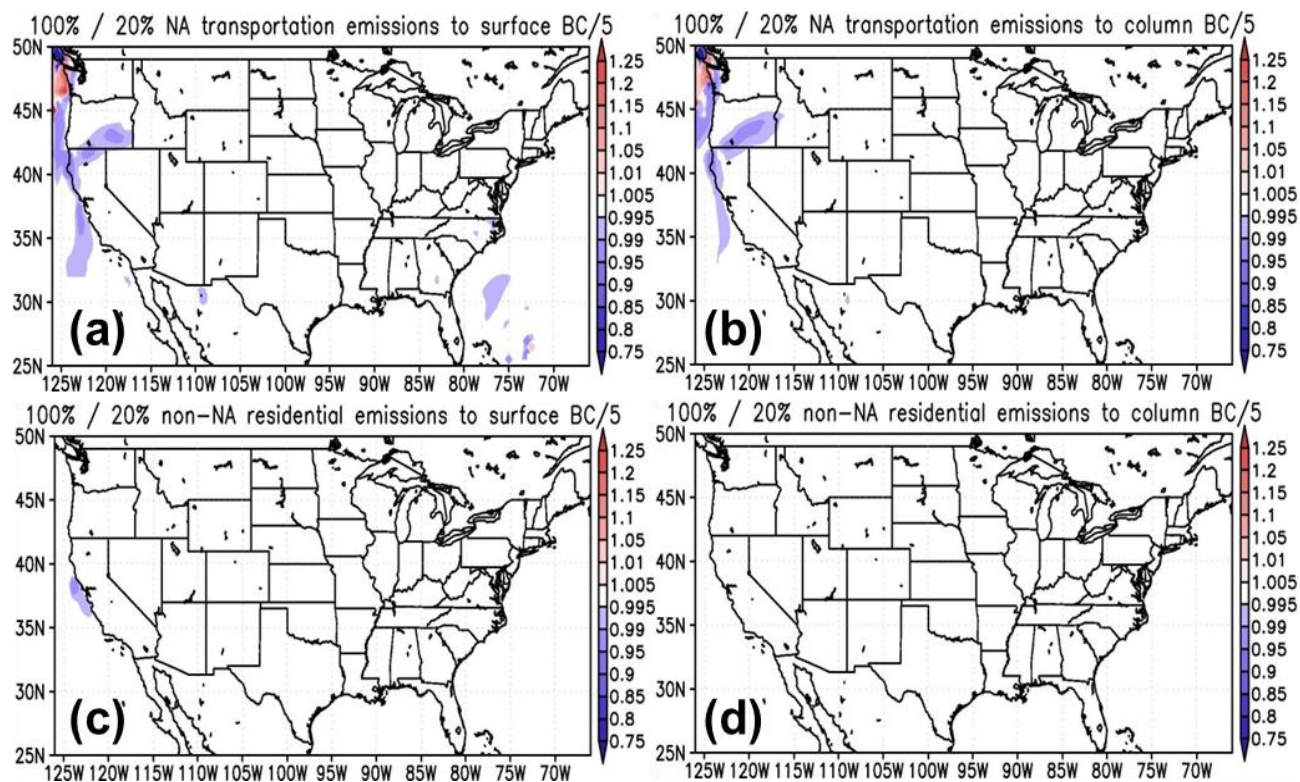


Figure 3.2 Ratios of two-week (13-26 June) mean (a;c) surface BC and (b;d) column BC responses to 100% and 20% perturbations in (a-b) NA transportation and (c-d) non-NA residential BC emissions, scaled by 5. These two sectors were found to be the major anthropogenic contributors among NA and non-NA sectors, respectively. For most US regions, the responses of BC distributions to emission perturbations are close to linear.

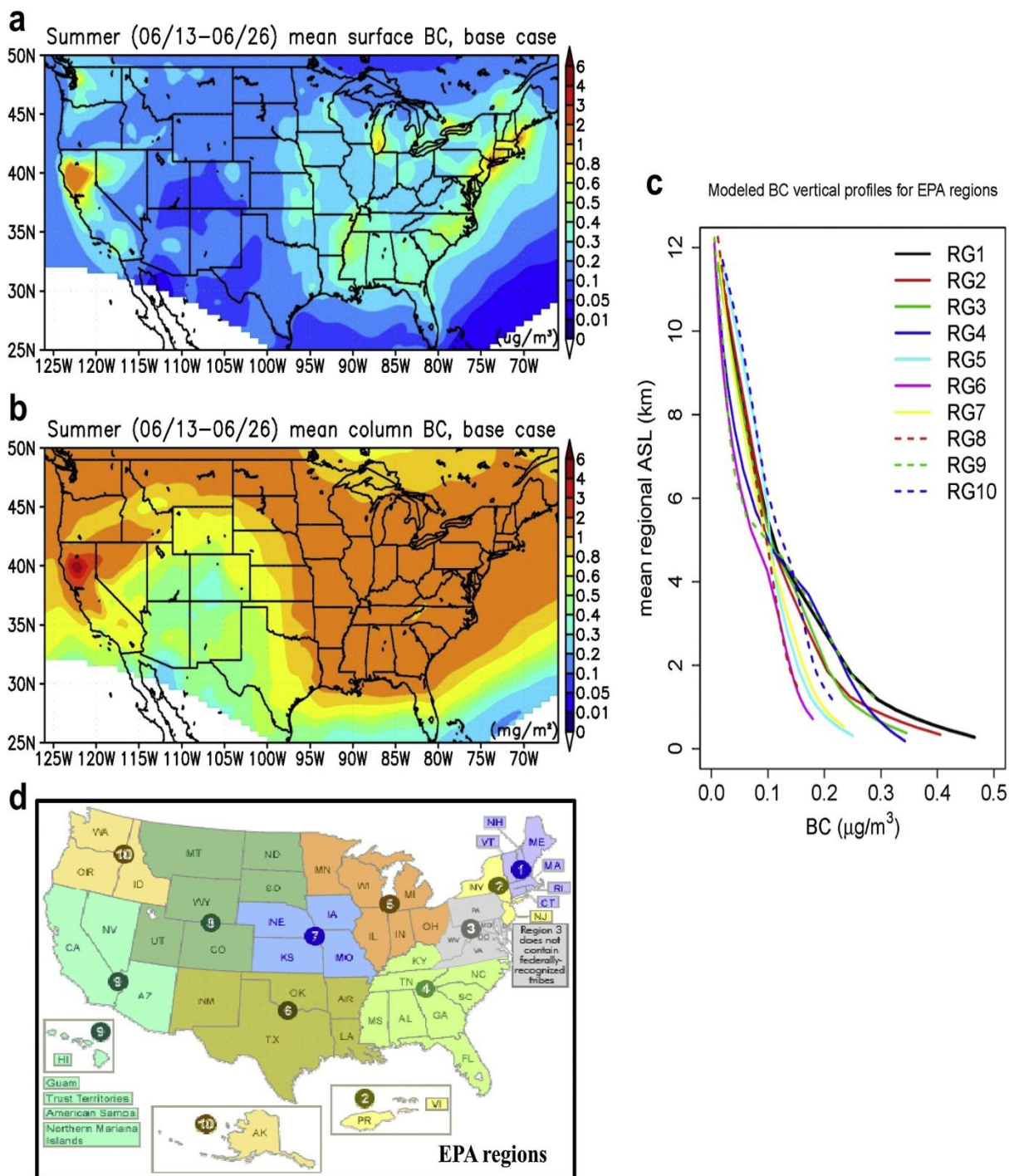


Figure 3.3 Two-week (13-26 June) mean (a) surface BC concentrations ($\mu\text{g}/\text{m}^3$); (b) BC column (mg/m^2); (c) BC vertical distributions ($\mu\text{g}/\text{m}^3$) in ten EPA regions; (d) The ten EPA regions.

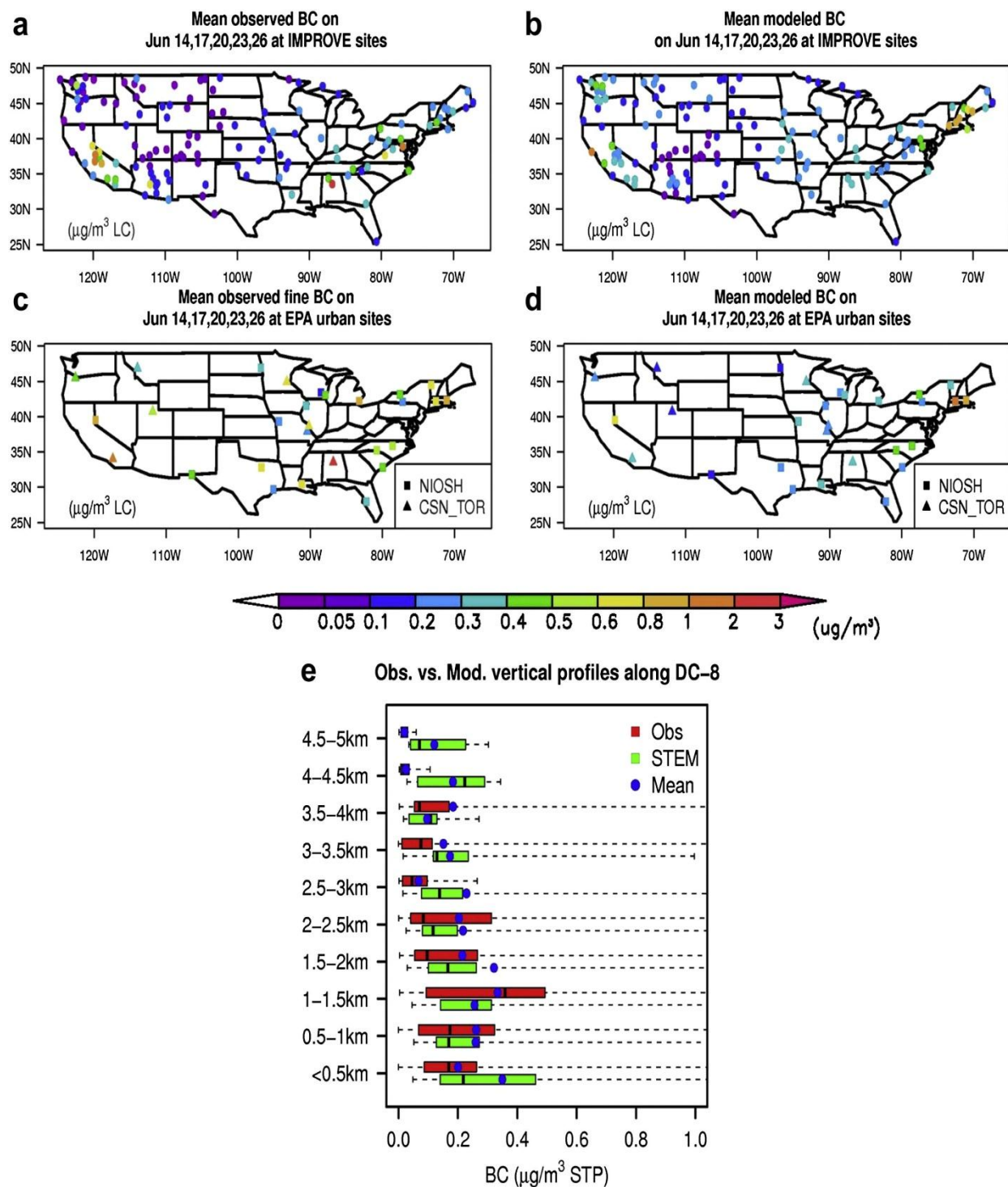


Figure 3.4 Mean (a) observed and (b) modeled BC ($\mu\text{g}/\text{m}^3$) on 14, 17, 20, 23, 26 June at the IMPROVE sites; Mean (c) observed and (d) modeled BC ($\mu\text{g}/\text{m}^3$) on 14, 17, 20, 23, 26 June at the EPA urban sites; (e) Observed and modeled BC ($\mu\text{g}/\text{m}^3$, at standard temperature and pressure) vertical profiles shown as boxplots along 20, 22, 24 June DC-8 flight tracks.

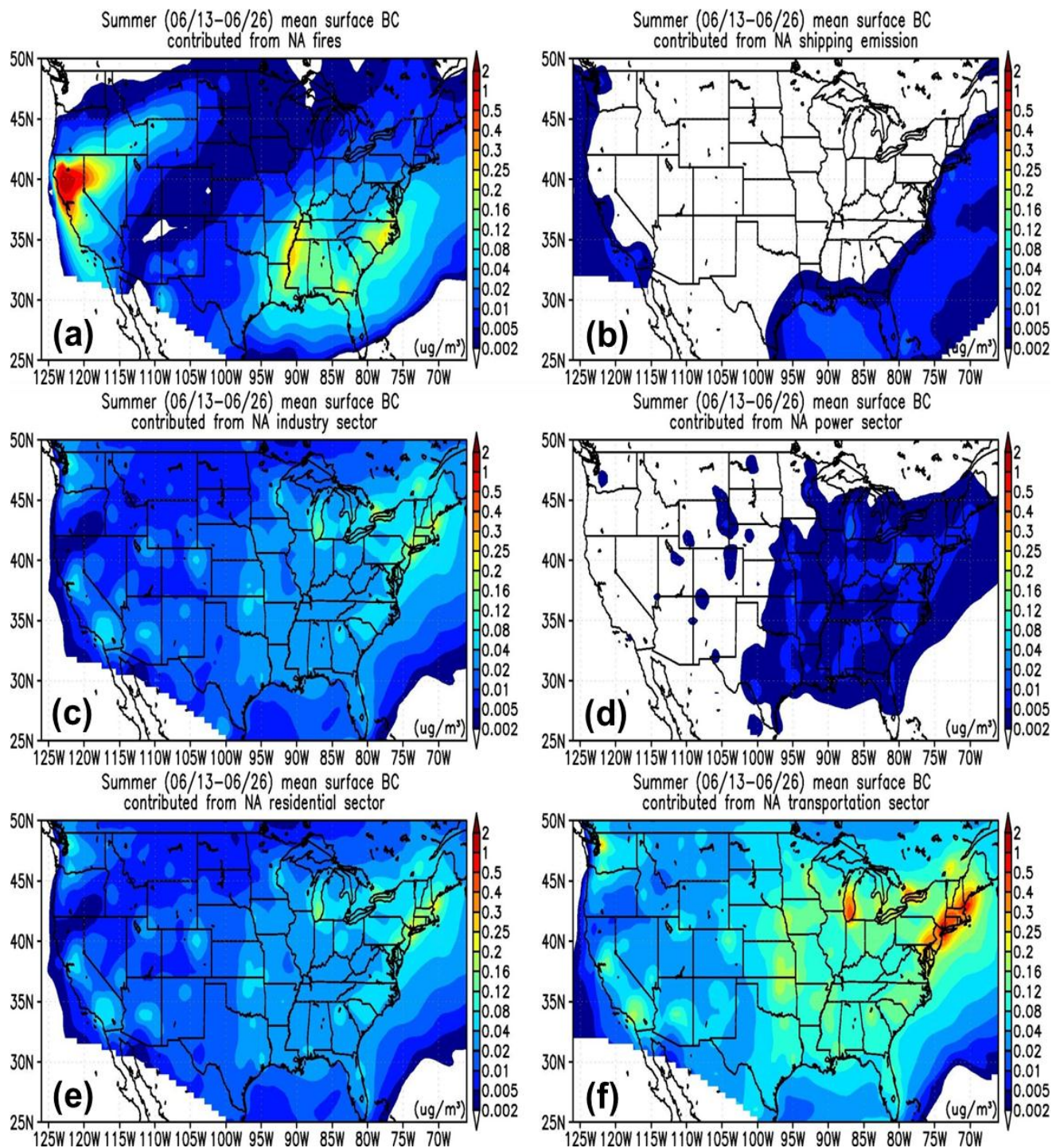


Figure 3.5 Two-week (13-26 June) mean surface BC ($\mu\text{g}/\text{m}^3$) contributed from (a) NA biomass burning; (b) shipping; (c) NA industrial; (d) NA power; (e) NA residential; (f) NA transportation emission sectors.

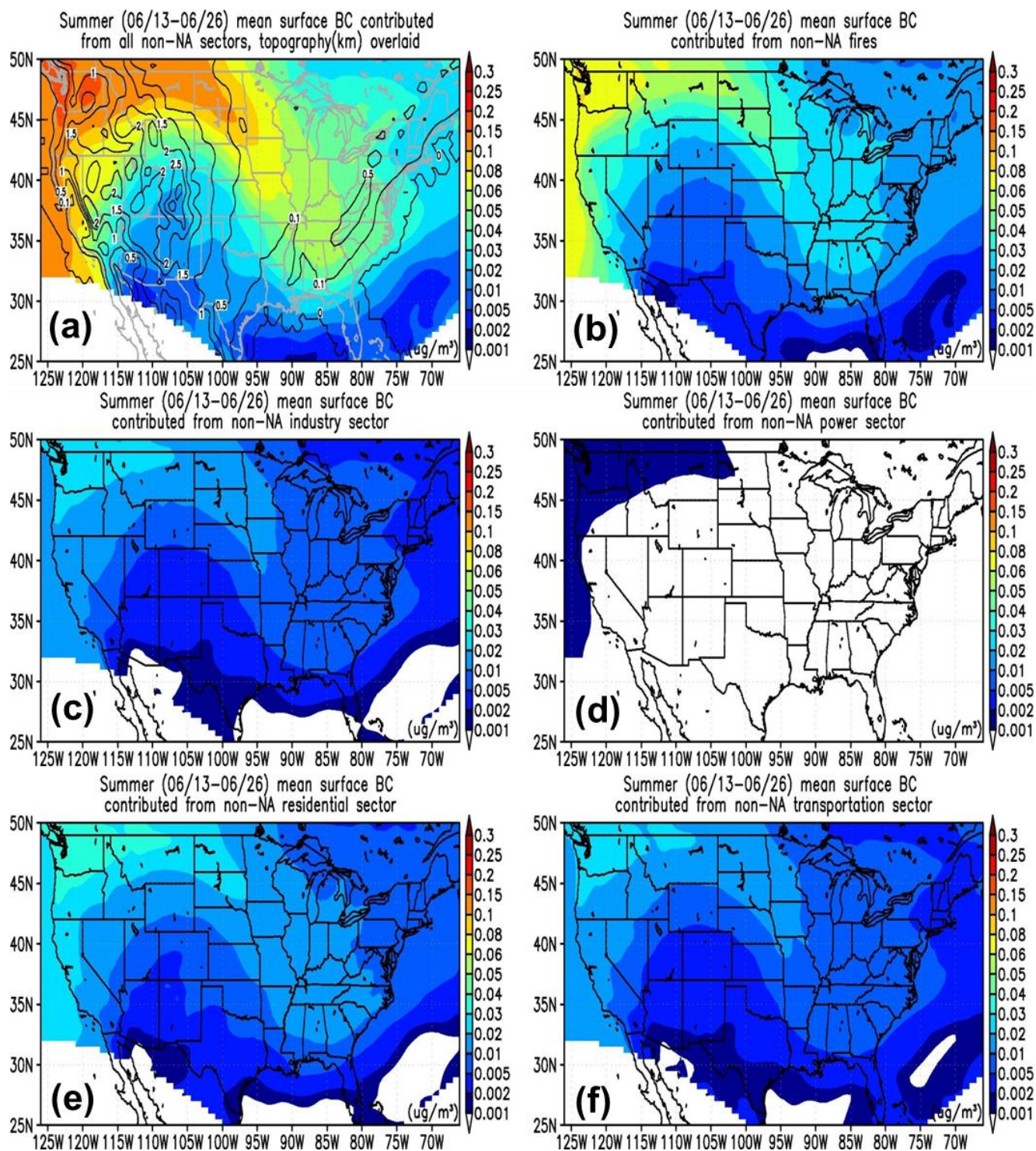


Figure 3.6 Two-week (13-26 June) mean surface BC ($\mu\text{g}/\text{m}^3$) contributed from (a) all non-NA; (b) non-NA biomass burning; (c) non-NA industrial; (d) non-NA power; (e) non-NA residential; (f) non-NA transportation emission sectors.

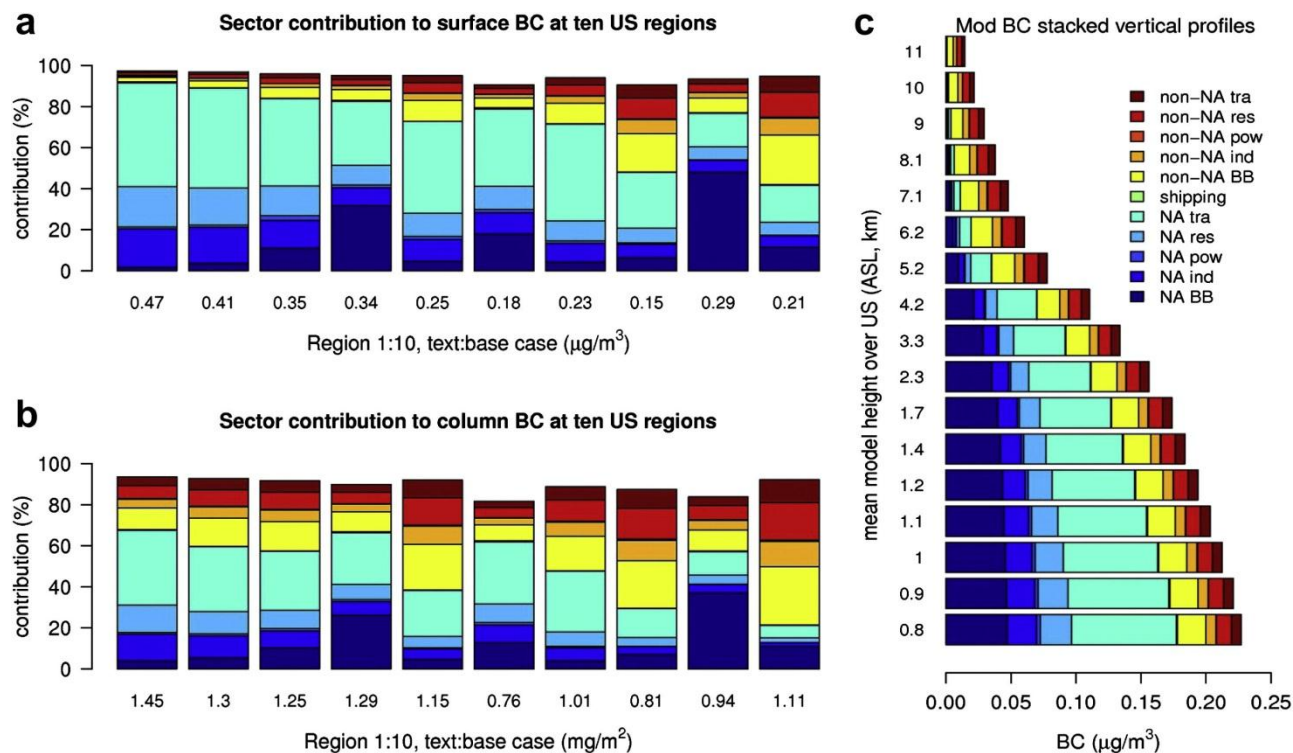


Figure 3.7 Stack plots of contributions from eleven sectors to US (a) surface BC ($\mu\text{g}/\text{m}^3$); (b) column BC (mg/m^2); (c) BC vertical profiles ($\mu\text{g}/\text{m}^3$) during 13-26 June, 2008.

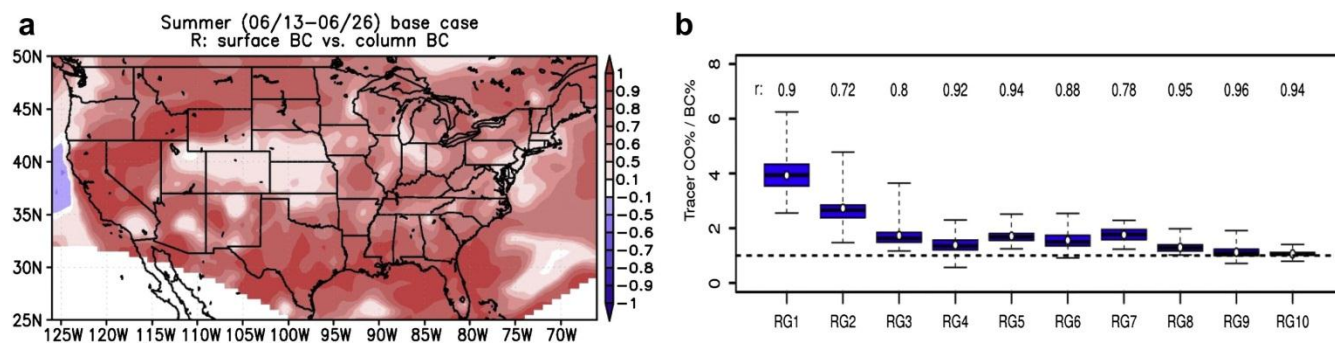


Figure 3.8 (a) Temporal correlation r between surface and column BC during 13-26 June, 2008; (b) Comparison between tracer extra-regional CO% and extra-regional BC% calculated by the forward sensitivity simulations for ten EPA regions.

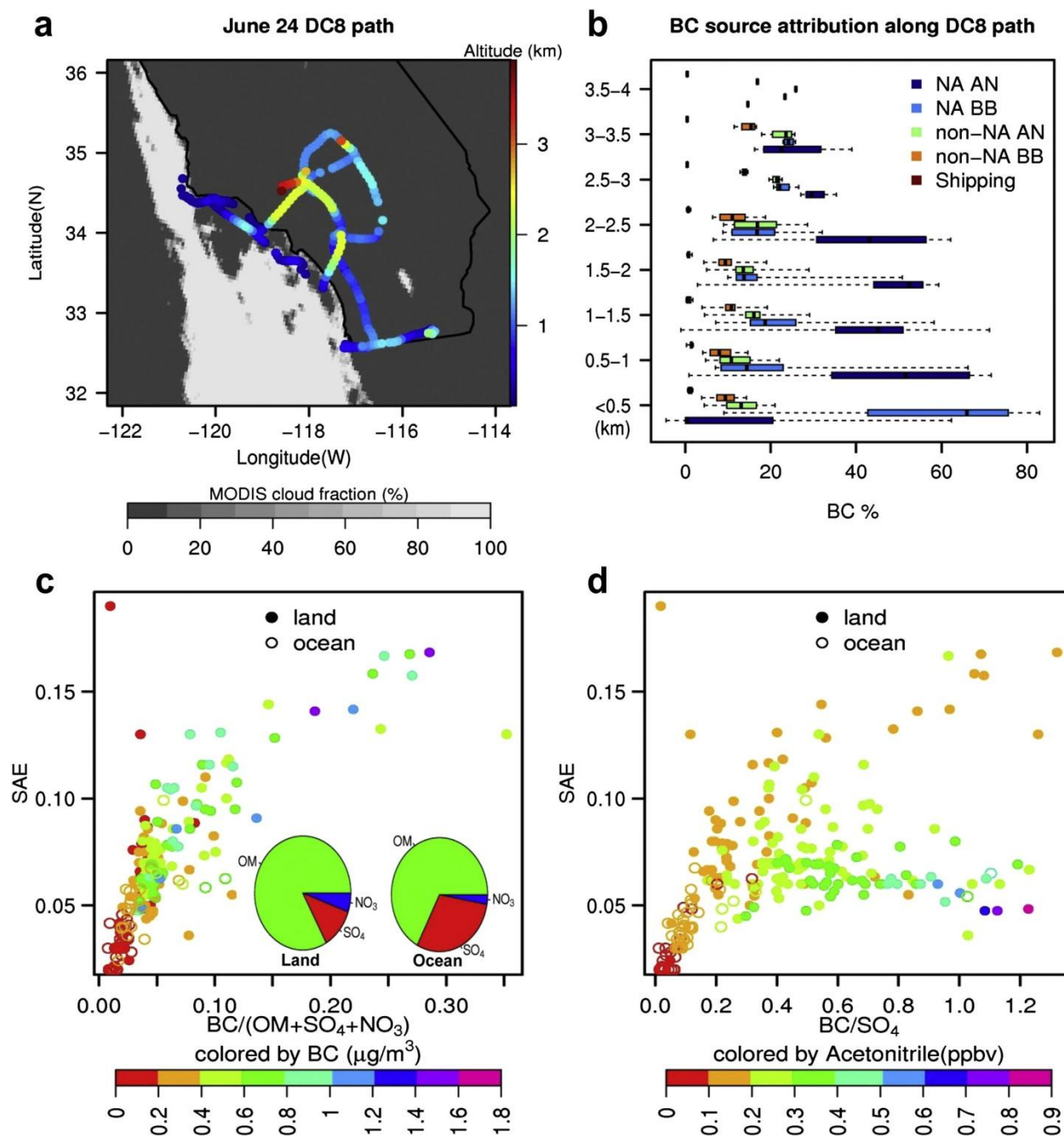


Figure 3.9 (a) The 24 June DC-8 flight path (where aerosols, acetonitrile and green band SSA measurements were made), colored by flight altitude (ASL, km), overlaid on MODIS cloud fraction at 18:45 UTC (11:45 am PDT); (b) BC source attribution along the flight, shown every 500 m in boxplots, AN and BB stand for anthropogenic and biomass burning, respectively; (c) Scatter plot of SAE against $BC/(OM + SO_4 + NO_3)$, colored by observed BC. Inner panel are pie plots of cooling aerosol compositions along the path in (a) for terrestrial and oceanic samples; (d) Scatter plot of SAE against BC/SO_4 , colored by observed acetonitrile. (MODIS: Moderate Resolution Imaging Spectroradiometer).

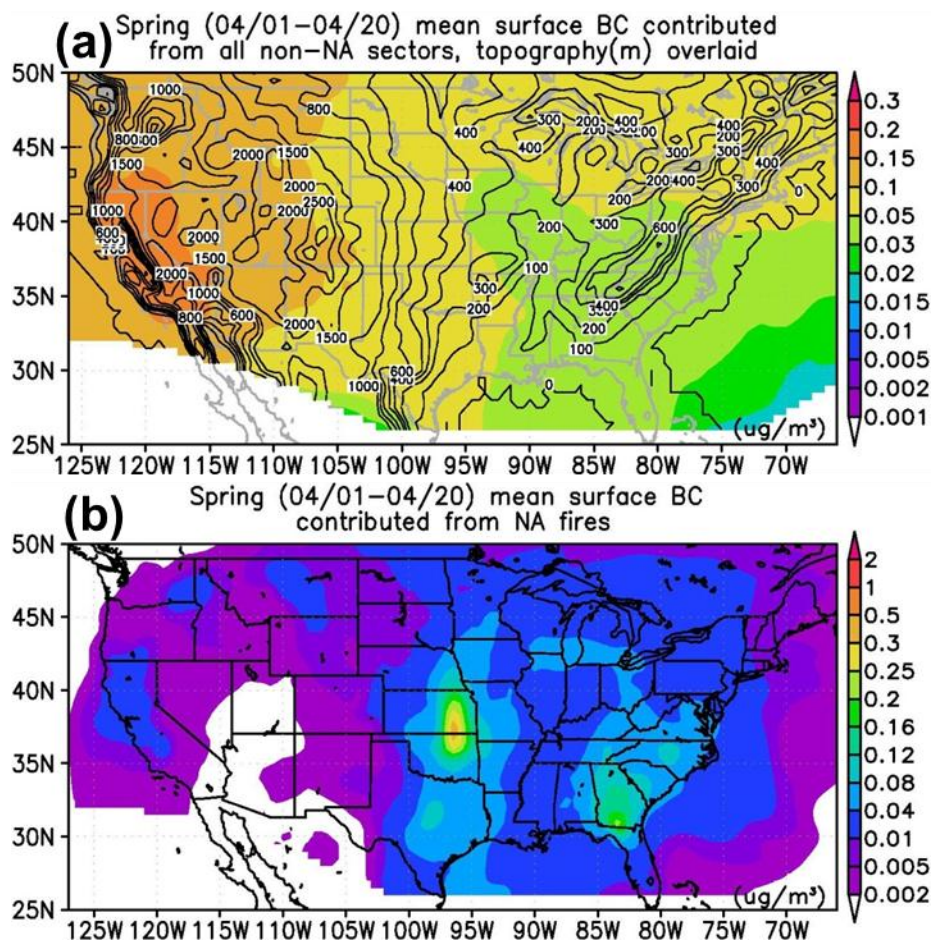


Figure 3.10 Spring (1-20 April, 2008) mean surface BC ($\mu\text{g}/\text{m}^3$) contributed from (a) all non-NA emission sectors and (b) NA biomass burning emissions.

CHAPTER 4

SUMMARY AND FUTURE WORK

4.1 Summary

The western US air quality is affected by the local emissions and processes (chemical reactions and in-state transport), and is also under the influence of the transported pollutants from out of the state (foreign nations sources, stratospheric impacts, etc). All these transport and production processes are highly dependent on the spatially and temporally varied meteorology and complicated geography. In this study, multi-scale tracer and full-chemistry simulations with the STEM atmospheric chemical transport model have been used to analyze the effects of transported and local production of pollutants on western US air quality in summer 2008, focusing on tropospheric ozone (O_3) and black carbon.

Chapter 1 briefly introduced the western US air quality and the research tool-STEM chemical transport model. Chapter 2 analyzed the impacts of transported background (TBG) pollutants on western US O_3 distributions. TBG is one of the important contributors to background O_3 , and it reflects the influences from extra-regional emission sources and stratosphere. Forward sensitivity simulations in which the model boundary conditions and emissions were perturbed show that impacts of TBG on western US surface O_3 are strong (>50% of the total O_3) and extensive, compared to other background O_3 contributors (North American (NA) biomass burning (BB) and biogenic emissions). Ozone is the largest single TBG pollutant, and peroxyacetyl nitrate is the most important TBG species among the O_3 precursors. The TBG impacts differ among various geographical regions and land types, and the W126 monthly index (a proposed secondary standard metric) shows stronger and higher non-linear responses to perturbations in TBG than monthly mean 8-hour daily maximum O_3 (MDA8, the primary standard metric). The TBG impacts are relatively weakly dependent on US anthropogenic emissions. The impacts of TBG are strongly affected by model vertical/horizontal resolution.

Three sites spanning $\sim 10^\circ$ in latitude were selected to study O_3 sources and the transport/subsidence processes. The O_3 trends at Mt. Bachelor (MBO) and Trinidad Head (THD) were mostly affected by transported background/ extra-regional pollutants under the control of similar synoptic conditions, and were both occasionally affected by US emissions; Southern California Coast (SC) O_3 was strongly affected by local emissions. The probabilities of airmasses originating from THD and MBO impacting downwind surface air quality reach daily maxima of 34% and 66% at 3 pm PDT, respectively, and the probability of airmasses originating from SC stay above 50% from 9 am to 4 pm. Receptor-based adjoint sensitivity analysis further highlights the transport/subsidence processes (e.g., transport altitude, time, strength) that link airmasses aloft with the surface.

A case study demonstrated that assimilating surface *in-situ* observations was successful in constraining modeled O_3 spatial distributions over the western US. Satellite products provided information outside of the regional model domain that can be used for to identify LRT episodes, but the inclusion of existing O_3 vertical profiles (satellite and sonde) in DA in the regional model did not efficiently improve the O_3 distributions except the locations near the sampling locations in this case. Denser/more frequent sampling and better method to incorporate these vertical profiles in DA are suggested. Assimilating surface observations and vertical profiles may also cause conflicts, which may be useful for determining the uncertainties in satellite retrievals and evaluating model configurations.

The sectoral and geographical contributions to summertime US black carbon distributions are discussed in Chapter 3. North American (NA) emissions heavily ($>70\%$ of total emissions) affect the BC levels from the surface to ~ 5 km, while non-NA plumes compose more than half of the BC above ~ 5 km. Among all sectors, NA and non-NA biomass burning, NA transportation and non-NA residential emissions are the major contributors. The sectoral contributions vary among ten regions defined by the US Environmental Protection Agency (EPA): NA anthropogenic emissions enhance northeastern US BC levels; biomass burning strongly impacts northern California and southeastern US; and the influence of extra-regional plumes is largest in

the northwestern US but extends to eastern US. The mean contribution from non-NA sources to US surface BC is $\sim 0.05 \mu\text{g}/\text{m}^3$, with a maximum value of $\sim 0.11 \mu\text{g}/\text{m}^3$ in the northwestern US. The non-NA contributions to column BC are higher than to surface BC, ranging from 30% to 80%, depending on region. EPA region 8 is most sensitive to extra-regional BC, partially explaining the observed increasing BC trend there during the past decades associated with the increasing Asian BC emissions. Measurements from the June 24 DC-8 flight during the ARCTAS-CARB field campaign show that BC/(organic matter + nitrate + sulfate) mass ratios fairly well represent BC's warming potential over southern California, which can be approximated by BC/(organic matter + sulfate) and BC/sulfate for plumes affected and unaffected by fires, respectively. The responses of BC/(organic matter + sulfate) and BC/sulfate to removing each emission sector are further discussed, indicating that mitigating NA transportation emissions has the highest potential for regional air quality and climate co-benefits. Finally, the summertime sector contributions are compared with a twenty-day period in April 2008 and the major differences are found mainly in the contributions of extra-regional sources and NA biomass burning.

Significance of these results include: 1) Long-range transport of pollution is important in summer, especially as the O_3 standard tends to be further tightened; 2) High resolution modeling is advantageous for generating simulated pollutant distribution, representing the transport/subsidence processes, and estimating the pollutant import/export budgets, especially over regions of complex topography; 3) Future observation system need to provide denser and more accurate vertical profiles, which would benefit understanding the downwind pollution level at surface and subsequent radiative transfer calculations; 4) Developing metrics to assess air quality and climate impacts in common frame work is promising but still challenging.

4.2 Future work

Two major future directions involve: 1) to advance our understanding of the sectoral and geographical contribution to atmospheric composition on extended spatial and temporal scales

using global model simulation, sensitivity analysis and data assimilation; and 2) to explore the linkages between air pollution and climate change.

Results in this study indicate the importance of combining global and regional models for source attribution studies. Global models are helpful for quantitatively estimating source contributions using both forward and adjoint sensitivity analysis for extended study periods, while coupling high resolution regional models with the global model(s) at the source/receptor sides can highly improve the estimates of pollutants import/export budgets and enable investigation in the details of individual processes, especially over the regions that have complex topography such as the western US. Global models can also evaluate the representativeness of the results in 2008 (from this study) for a longer period (e.g., 10-20 years) and select other interesting study periods. Selecting appropriate response functions in adjoint sensitivity analysis (other than the concentrations at a specific time), incorporating “full” adjoint sensitivity calculations (which involve the inverse of winds) and the comparisons among multiple models (e.g., offline versus online chemical transport model such as WRF-Chem) will help better understand the processes determining the state of atmosphere and sources of model errors. In addition, applying data assimilation in global models through longer periods to include more available observations in three dimensions, as well as through multiple methods (such as Kalman filter) will be further explored, and using data assimilation to quantify uncertainties in certain observations may be further studied in detail.

Developing policy-relevant metrics reflecting the combined climate and air quality implications will require the evaluation by radiative flux calculations. The radiative transfer calculations are normally obtained by radiative transfer models whose performance is dependent on species concentrations and meteorological conditions, and therefore are usually of higher uncertainties. Conducting model inter-comparisons and incorporating observations (such as measurements during field campaigns and satellites) will help improve these estimates.

REFERENCES

- Adhikary, B., Carmichael, G. R., Kulkarni, S., Wei, C., Tang, Y., D'Allura, A., Mena-Carrasco, M., Streets, D. G., Zhang, Q., Pierce, R. B., Al-Saadi, J. A., Emmons, L. K., Pfister, G. G., Avery, M. A., Barrick, J. D., Blake, D. R., Brune, W. H., Cohen, R. C., Dibb, J. E., Fried, A., Heikes, B. G., Huey, L. G., O'Sullivan, D. W., Sachse, G. W., Shetter, R. E., Singh, H. B., Campos, T. L., Cantrell, C. A., Flocke, F. M., Dunlea, E. J., Jimenez, J. L., Weinheimer, A. J., Crouse, J. D., Wennberg, P. O., Schauer, J. J., Stone, E. A., Jaffe, D. A., and Reidmiller, D. R.: A regional scale modeling analysis of aerosol and trace gas distributions over the eastern Pacific during the INTEX-B field campaign, *Atmospheric Chemistry and Physics*, 10, 2091-2115, doi:10.5194/acp-10-2091-2010, 2010.
- Aghedo, A. M., Bowman, K. W., Worden, H. M., Kulawik, S. S., Shindell, D. T., Lamarque, J. F., Faluvegi, G., Parrington, M., Jones, D. B. A., and S. Rast: The vertical distribution of ozone instantaneous radiative forcing from satellite and chemistry climate models, *Journal of Geophysical Research*, 116, D01305, doi:10.1029/2010JD014243, 2011.
- Alvarado, M. J., Logan, J. A., Mao, J., Apel, E., Riemer, D., Blake, D., Cohen, R. C., Min, K.-E., Perring, A. E., Browne, E. C., Wooldridge, P. J., Diskin, G. S., Sachse, G. W., Fuelberg, H., Sessions, W. R., Harrigan, D. L., Huey, G., Liao, J., Case-Hanks, A., Jimenez, J. L., Cubison, M. J., Vay, S. A., Weinheimer, A. J., Knapp, D. J., Montzka, D. D., Flocke, F. M., Pollack, I. B., Wennberg, P. O., Kurten, A., Crouse, J., Clair, J. M. St., Wisthaler, A., Mikoviny, T., Yantosca, R. M., Carouge, C. C., and Le Sager, P.: Nitrogen oxides and PAN in plumes from boreal fires during ARCTAS-B and their impact on ozone: an integrated analysis of aircraft and satellite observations, *Atmospheric Chemistry and Physics*, 10, 9739-9760, doi: 10.5194/acp-10-9739-2010, 2010.
- Ambrose, J., Reidmiller, D., and Jaffe, D.: Causes of high O₃ in the lower free troposphere over the Pacific Northwest as seen at the Mt. Bachelor Observatory, *Atmospheric Environment*, 45(30), 5302-5315, doi: 10.1016/j.atmosenv.2011.06.056, 2011.
- Arneth, A., Unger, N., Kulmala, M., and Andreae, M.: Clean Air, Heat the Planet? *Science*, 326, 672-6, doi: 10.1126/science.1181568, 2009.
- Balkanski, Y., Myhre, G., Gauss, M., Rädcl, G., Highwood, E. J., and Shine, K. P.: Direct radiative effect of aerosols emitted by transport: from road, shipping and aviation, *Atmospheric Chemistry and Physics*, 10, 4477-4489, doi: 10.5194/acp-10-4477-2010, 2010.
- Beer, R.: TES on the Aura Mission: Scientific Objectives, Measurements, and Analysis Overview, *IEEE Transaction on Geoscience and Remote Sensing*, 44 (5), 1102-1105, doi: 10.1109/TGRS.2005.863716, 2006.
- Bertschi, I.B., Jaffe, D.A., Jaegle, L., Price, H.U., and Dennison, J.B.: PHOBEA/ITCT 2002 airborne observations of trans-Pacific transport of ozone, CO, VOCs and aerosols to the northeast Pacific: Impacts of Asian anthropogenic and Siberian Boreal fire emissions, *Journal of Geophysical Research*, 109, D23S12, 10.1029/2003JD004328, 2004.

- Bond, T.C. and Bergstrom, R.W.: Light Absorption by Carbonaceous Particles: An Investigative Review, *Aerosol Science and Technology*, 40, 27-67, doi: 10.1080/02786820500421521, 2006.
- Bond, T. C., Streets, D. G., Yarber, K. F., Nelson, S. M., Woo, J.-H., and Klimont, Z.: A technology-based global inventory of black and organic carbon emissions from combustion, *Journal of Geophysical Research*, 109, D14203, doi: 10.1029/2003JD003697, 2004.
- Bouttier, F., and Courtier, P.: Data assimilation concepts and methods, http://www.ecmwf.int/newsevents/training/rcourse_notes/DATA_ASSIMILATION/ASSIM_CONCEPTS/Assim_concepts.html, 1999.
- Bowman, K. W., Rodgers, C. D., Kulawik, S. S., Worden, J., Sarkissian, E., Osterman, G., Steck, T., Ming Lou, Eldering, A., Shephard, M., Worden, H., Lampel, M., Clough, S., Brown, P., Rinsland, C., Gunson, M., and Beer, R., Tropospheric Emission Spectrometer: Retrieval method and error analysis, *IEEE Transaction on Geoscience and Remote Sensing*, 44(5), 1297–1307, doi: 10.1109/TGRS.2006.871234, 2006.
- Boxe, C.S., Worden, J.R., Bowman, K.W., Kulawik, S.S., Neu, J.L., Ford, W.C., Osterman, G.B., Herman, R. L., Eldering, A., Tarasick, D.W., Thompson, A.M., Doughty, D.C., Hoffmann, M.R., and Oltmans, S.J.: Validation of northern latitude Tropospheric Emission Spectrometer stare ozone profiles with ARC-IONS sondes during ARCTAS: sensitivity, bias and error analysis, *Atmospheric Chemistry and Physics*, 10, 9901-9914, doi:10.5194/acp-10-9901-2010, 2010.
- Brock, C.A., Hudson, P.K., Lovejoy, E.R., Sullivan, A., Nowak, J.B., Huey, L.G., Cooper, O.R., Cziczo, D.J., de Gouw, J., Fehsenfeld, F.C., Holloway, J.S., Hubler, G., Lafleur, B.G., Murphy, D.M., Neuman, J.A., Nicks, D.K., Orsini, D.A., Parrish, D.D., Ryerson, T.B., Tanner, D.J., Warneke, C., Weber, R.J., and Wilson, J.C.: Particle characteristics following cloud-modified transport from Asia to North America, *Journal of Geophysical Research*, 109, D23S26 doi: 10.1029/2003JD004198, 2004.
- Campbell, J.E., Carmichael, G. R., Tang, Y., Chai, T., Vay, S. A., Choi, Y.-H., Sachse, G. W., Singh, H. B., Schnoor, J. L., Woo, J., Vukovich, J. M., Streets, D. G., Huey, L. G. and Stanier, C. O.: Analysis of anthropogenic CO₂ signal in ICARTT using a regional chemical transport model and observed tracers, *Tellus B*, 59: 199–210, doi: 10.1111/j.1600-0889.2006.00239.x, 2007.
- Carmichael, G.R., Tang, Y., Kurata, G., Uno, I., Streets, D.G., Thongboonchoo, N., Woo, J.H., Guttikunda, S., White, A., Wang, T., Blake, D.R., Atlas, E., Fried, A., Potter, B., Avery, M.A., Sachse, G.W., Sandholm, S.T., Kondo, Y., Talbot, R.W., Bandy, A., Thornton, D., and Clarke, A.D.: Evaluating regional emission estimates using the TRACE-P observations, *Journal of Geophysical Research*, 108 (D21), 8810, doi: 10.1029/2002JD003116, 2003a.

- Carmichael, G.R., Tang, Y., Kurata, G., Uno, I., Streets, D., Woo, J.H., Huang, H., Yienger, J., Lefer, B., Shetter, R., Blake, D., Atlas, E., Fried, A., Apel, E., Eisele, F., Cantrell, C., Avery, M., Barrick, J., Sachse, G., Brune, W., Sandholm, S., Kondo, Y., Singh, H., Talbot, R., Bandy, A., Thornton, D., Clarke, A., and Heikes, B.: Regional-scale chemical transport modeling in support of the analysis of observations obtained during the TRACE-P experiment, *Journal of Geophysical Research*, 108 (D21), 8823, doi: 10.1029/2002JD003117, 2003b.
- Carmichael, G. R., Sandu, A., Chai, T., Daescu, D. N., Constantinescu, E. M., and Tang, Y.: Predicting air quality: Improvements through advanced methods to integrate models and measurements, *Journal of Computational Physics*, 227, 3540-3571, doi:10.1016/j.jcp.2007.02.024, 2008.
- Carter, W. P. L.: Documentation of the SAPRC-99 chemical mechanism for VOC Reactivity Assessment, final report to California Air Resources Board, Contract No. 92-329 and 95-308, 2000.
- Chai, T., Carmichael, G. R., Sandu, A., Tang, Y., and Daescu, D.N.: Chemical data assimilation of Transport and Chemical Evolution over the Pacific (TRACE-P) aircraft measurements, *Journal of Geophysical Research*, 111, D02301, doi: 10.1029/2005JD005883, 2006.
- Chai, T., Carmichael, G. R., Tang, Y., Sandu, A., Hardesty, M., Pilewskie, P., Whitlow, S., Browell, E. V., Avery, M. A., Nedelec, P., Merrill, J. T., Thompson, A. M., and Williams, E.: Four Dimensional Data Assimilation Experiments with ICARTT (International Consortium for Atmospheric Research on Transport and Transformation) Ozone Measurements, *Journal of Geophysical Research*, 112, D12S15, doi: 10.1029/2006JD007763, 2007.
- Chai, T., Carmichael, G. R., Tang, Y., Sandu, A., Heckel, A., Richter, A., and Burrows, J. P.: Regional NO_x emission inversion through a four-dimensional variational approach using SCIAMACHY tropospheric NO₂ column observations, *Atmospheric Environment*, 43 (32), 5046-5055, 2009.
- Chin, M., Jacob, D. J., Munger, J. W., Parrish, D. D., and Doddridge, B. G.: Relationship of ozone and carbon monoxide over North America, *Journal of Geophysical Research*, 99 (D7), doi:10.1029/94JD00907, 14565–14573, 1994.
- Chin, M.: Atmospheric Aerosol Properties and Climate Impacts, <http://downloads.climate-science.gov/sap/sap2-3/sap2-3-final-report-all.pdf>, 2009.
- Cooke, W. F. and Wilson, J. J. N.: A global black carbon aerosol model. *Journal of Geophysical Research*, 101, D14, 19395-19409, doi: 10.1029/96JD00671, 1996.

- Cooper, O. R., Trainer, M., Thompson, A.M., Oltmans, S. J., Tarasick, D.W., Witte, J.C., Stohl, A., Eckhardt, S., Lelieveld, J., Newchurch, M.J., Johnson, B. J., Portmann, R. W., Kalnajs, L., Dubey, M.K., Leblanc, T., McDermid, I.S., Forbes, G., Wolfe, D. E., Carey-Smith, T., Morris, G.A., Lefer, B., Rappenglück, B., Joseph, E., Schmidlin, F., Meagher, J. F., Fehsenfeld, F. C., Keating, T.J., Van Curen, R.A., and Minschwaner, K.: Evidence for a recurring eastern North America upper tropospheric ozone maximum during summer, *Journal of Geophysical Research*, 112, D23304, doi: 10.1029/2007JD008710, 2007.
- Cooper, O. R., Parrish, D. D., Stohl, A., Trainer, M., Nedelec, P., Thouret, V., Cammas, J. P., Oltmans, S. J., Johnson, B. J., Tarasick, D., Leblanc, T., McDermid, I. S., Jaffe, D., Gao, R., Stith, J., Ryerson, T., Aikin, K., and Campos, T., Weinheimer, A., and Avery, M. A.: Increasing springtime ozone mixing ratios in the free troposphere over western North America, *Nature*, 463, doi: 10.1038/nature08708, 2010.
- Cooper, O. R., Oltmans, S. J., Johnson, B. J., Brioude, J., Angevine, W., Trainer, M., Parrish, D. D., Ryerson, T. R., Pollack, I., Cullis, P. D., Ives, M. A., Tarasick, D. W., Al-Saadi, J., and Stajner, I.: Measurement of western U.S. baseline ozone from the surface to the tropopause and assessment of downwind impact regions, *Journal of Geophysical Research*, 116, D00V03, doi: 10.1029/2011JD016095, 2011.
- Cox, P., Delao, A., Komorniczak, A., and Weller, R.: The California almanac of emissions and air quality 2009 edition, <http://www.arb.ca.gov/aqd/almanac/almanac09/almanac2009all.pdf>, 2010.
- Davies, D. K., Ilavajhala, S., Wong, M.M., and Justice, C.O.: Fire Information for Resource Management System: Archiving and Distributing MODIS Active Fire Data, *IEEE Transactions on Geoscience and Remote Sensing*, 47 (1), 72-79, 2009.
- D'Allura, A., Kulkarni, S., Carmichael, G. R., Finardi, S., Adhikary, B., Wei, C., Streets, D. G., Zhang, Q., Pierce, R. B., Al-Saadi, J. A., Diskin, G., and Wennberg, P.: Meteorological and air quality forecasting using the WRF-STEM model during the 2008 ARCTAS field campaign, *Atmospheric Environment*, 45 (38), 6901-6910, doi:10.1016/j.atmosenv.2011.02.073, 2011.
- Dunlea, E. J., DeCarlo, P. F., Aiken, A. C., Kimmel, J. R., Peltier, R. E., Weber, R. J., Tomlinson, J., Collins, D. R., Shinozuka, Y., McNaughton, C. S., Howell, S. G., Clarke, A. D., Emmons, L. K., Apel, E. C., Pfister, G. G., van Donkelaar, A., Martin, R. V., Millet, D. B., Heald, C. L., and Jimenez, J. L.: Evolution of Asian aerosols during transpacific transport in INTEX-B, *Atmospheric Chemistry and Physics*, 9, 7257-7287, doi:10.5194/acp-9-7257-2009, 2009.

- Fast, J. D., Gustafson Jr., W. I., Berg, L. K., Shaw, W. J., Pekour, M., Shrivastava, M., Barnard, J. C., Ferrare, R. A., Hostetler, C. A., Hair, J. A., Erickson, M., Jobson, B. T., Flowers, B., Dubey, M. K., Springston, S., Pierce, R. B., Dolislager, L., Pederson, J., and Zaveri, R. A.: Transport and mixing patterns over Central California during the carbonaceous aerosol and radiative effects study (CARES), *Atmospheric Chemistry and Physics*, 12, 1759-1783, doi:10.5194/acp-12-1759-2012, 2012.
- Fischer, E. V., Jaffe, D. A., Reidmiller, D. R., and Jaegle, L.: Meteorological controls on observed peroxyacetyl nitrate at Mount Bachelor during the spring of 2008, *Journal of Geophysical Research*, 115, D03302, doi: 10.1029/2009JD012776, 2010.
- Fischer, E. V., Jaffe, D. A., Marley, M., Gaffney, J., and Marchany-Rivera, A.: Optical properties of aged Asian aerosols observed over the U.S. Pacific Northwest, *Journal of Geophysical Research*, 115, D20209, doi: 10.1029/2010JD013943, 2010.
- Fischer, E. V., Jaffe, D. A., and Weatherhead, E. C.: Free tropospheric peroxyacetyl nitrate (PAN) and ozone at Mount Bachelor: causes of variability and timescale for trend detection, *Atmospheric Chemistry and Physics*, 11, 5641-5654, doi: 10.5194/acp-11-5641-2011, 2011.
- Fiore, A. M., Dentener, F. J., Wild, O., Cuvelier, C., Schultz, M. G., Hess, P., Textor, C., Schulz, M., Doherty, R. M., Horowitz, L. W., MacKenzie, I. A., Sanderson, M. G., Shindell, D. T., Stevenson, D. S., Szopa, S., Van Dingenen, R., Zeng, G., Atherton, C., Bergmann, D., Bey, I., Carmichael, G., Collins, W. J., Duncan, B. N., Faluvegi, G., Folberth, G., Gauss, M., Gong, S., Hauglustaine, D., Holloway, T., Isaksen, I. S. A., Jacob, D. J., Jonson, J. E., Kaminski, J. W., Keating, T. J., Lupu, A., Marmer, E., Montanaro, V., Park, R. J., Pitari, G., Pringle, K. J., Pyle, J. A., Schroeder, S., Vivanco, M. G., Wind, P., Wojcik, G., Wu, S., and Zuber, A.: Multimodel estimates of intercontinental source receptor relationships for ozone pollution, *Journal of Geophysical Research*, 114, D04301, doi: 10.1029/2008JD010816, 2009.
- Freitas, S. R., Longo, K. M., Alonso, M. F., Pirre, M., Marecal, V., Grell, G., Stockler, R., Mello, R. F., and Sánchez Gácita, M.: PREP-CHEM-SRC – 1.0: a preprocessor of trace gas and aerosol emission fields for regional and global atmospheric chemistry models, *Geoscientific Model Development*, 4, 419-433, doi: 10.5194/gmd-4-419-2011, 2011.
- Fuelberg, H. E., Harrigan, D. L., and Sessions, W.: A meteorological overview of the ARCTAS 2008 mission, *Atmospheric Chemistry and Physics*, 10, 817–842, 2010.
- Fuglestedt, J., Berntsen, T., Myhre, G., Rypdal, K. and Skeie, R. B: Climate forcing from the transport sectors. *Proceedings of the National Academy of Sciences of the United States of America*, 105, 454–458, doi: 10.1073/pnas.0702958104, 2007.
- Giglio, L., Descloitres, J., Justice, C. O., and Kaufman, Y. J.: An Enhanced Contextual Fire Detection Algorithm for MODIS, *Remote Sensing of Environment*, 87, 273-282, 2003.

- Hakami, A., Henze, D. K., Seinfeld, J. H., Chai, T., Tang, Y., Carmichael, G. R., and Sandu, A.: Adjoint Inverse Modeling of Black Carbon During ACE-Asia, *Journal of Geophysical Research*, 110, D14301, doi: 10.1029/2004JD005671, 2005.
- Hakami, A., Seinfeld, J. H., Chai, T. F., Tang, Y. H., Carmichael, G. R and Sandu, A: Adjoint sensitivity analysis of ozone nonattainment over the continental United States, *Environmental Science and Technology*, 40 (12), 3855-3864, doi: 10.1021/es052135g, 2006.
- Heald, C. L., Jacob, D. J., Park, R. J., Alexander, B., Fairlie, T. D., Yantosca, R. M., and Chu, D. A.: Transpacific transport of Asian anthropogenic aerosols and its impact on surface air quality in the United States, *Journal of Geophysical Research*, 111, D14310, doi: 10.1029/2005JD006847, 2006.
- Heath, R. L., Lefohn, A. S., and Musselman, R. C.: Temporal processes that contribute to nonlinearity in vegetation responses to ozone exposure and dose, *Atmospheric Environment*. 43: 2919-2928, 2009.
- Henze, D. K., Seinfeld, J. H., and Shindell, D. T.: Inverse modeling and mapping U.S. air quality influences of inorganic PM_{2.5} precursor emissions with the adjoint of GEOS-Chem, *Atmospheric Chemistry and Physics*, 9, 5877-5903, doi: 10.5194/acp-9-5877-2009, 2009.
- Huang, M., Carmichael, G. R., Adhikary, B., Spak, S. N., Kulkarni, S., Cheng, Y. F., Wei, C., Tang, Y., Parrish, D. D., Oltmans, S. J., D'Allura, A., Kaduwela, A., Cai, C., Weinheimer, A. J., Wong, M., Pierce, R. B., Al-Saadi, J. A., Streets, D. G., and Zhang, Q.: Impacts of transported background ozone on California air quality during the ARCTAS-CARB period – a multi-scale modeling study, *Atmospheric Chemistry and Physics*, 10, 6947-6968, doi:10.5194/acp-10-6947-2010, 2010a.
- Huang, M., Carmichael, G. R., Spak, S., Adhikary, B., Kulkarni, S., Cheng, Y., Wei, C., Tang, Y., Parrish, D. D., Oltmans, S. J., D'Allura, A., Wennberg, P. O., Huey, L. G., Dibb, J. E., Jimenez, J. L., Weinheimer, A. J., Kaduwela, A., Cai, C., Wong, M., Pierce, R., Al-Saadi, J. A., Streets, D. G., and Zhang, Q.: Impacts of long-range transport and local emissions on California near-surface ozone and sulfur oxides during the ARCTAS period--A multi-scale modeling study, AGU fall meeting, San Francisco, CA, December, 2010b.
- Huang, M., Carmichael, G. R., Spak, S. N., Adhikary, B., Kulkarni, S., Cheng, Y. F., Wei, C., Tang, Y., D'Allura, A., Wennberg, P. O., Huey, G. L., Dibb, J. E., Jimenez, J. L., Cubison, M. J., Weinheimer, A. J., Kaduwela, A., Cai, C., Wong, M., Pierce, R. B., Al-Saadi, J. A., Streets, D. G., and Zhang, Q.: Multi-scale modeling study of the source contributions to near-surface ozone and sulfur oxides levels over California during the ARCTAS-CARB period, *Atmospheric Chemistry and Physics*, 11, 3173-3194, doi:10.5194/acp-11-3173-2011, 2011.

- Huang, M., Carmichael, G. R., Kulkarni, S., Streets, D. G., Lu, Z., Zhang, Q., Pierce, R. B., Kondo, Y., Jimenez, J. L., Cubison, M. J., Anderson, B., and Wisthaler, A.: Sectoral and geographical contributions to summertime continental United States (CONUS) black carbon spatial distributions, *Atmospheric Environment*, 51, 165-174, doi:10.1016/j.atmosenv.2012.01.021, 2012.
- IPCC: Contribution of Working Group I to the Fourth Assessment Report of the Intergovernmental Panel on Climate Change, *The Physical Science Basis*, Cambridge, United Kingdom and New York, NY, USA, Cambridge University Press, 2007.
- Jacob, D. J., Crawford, J. H., Maring, H., Clarke, A. D., Dibb, J. E., Emmons, L. K., Ferrare, R. A., Hostetler, C. A., Russell, P. B., Singh, H. B., Thompson, A. M., Shaw, G. E., McCauley, E., Pederson, J. R., and Fisher, J. A.: The Arctic Research of the Composition of the Troposphere from Aircraft and Satellites (ARCTAS) mission: design, execution, and first results, *Atmospheric Chemistry and Physics*, 10, 5191–5212, doi: 10.5194/acp-10-5191-2010, 2010.
- Jacobson, M. Z.: Control of fossil-fuel particulate black carbon plus organic matter, possibly the most effective method of slowing global warming, *Journal of Geophysical Research*, 107, (D19), 4410, doi: 10.1029/2001JD001376, 2002.
- Jacobson, M. Z.: The short-term cooling but long-term global warming due to biomass burning, *Journal of Climate*, 17, 2909-2926, 2004.
- Jaffe, D., Bertschi, I., Jaegle, L., Novelli, P., Reid, J. S., Tanimoto, H., Vingarzan, R., and Westphal, D. L.: Long-range transport of Siberian biomass burning emissions and impact on surface ozone in western North America, *Geophysical Research Letters*, 31, L16106, doi: 10.1029/2004GL020093, 2004.
- Jaffe, D., Tamura, S., and Harris, J.: Seasonal cycle, composition and sources of background fine particles along the west coast of the U.S., *Atmospheric Environment*, 39, 297-306, doi: 10.1016/j.atmosenv.2004.09.016, 2005.
- Jaffe, D. and Ray, J.: Increase in Surface Ozone at Rural Sites in the Western U.S., *Atmospheric Environment*, 41, 5452-5463, doi: 10.1016/j.atmosenv.2007.02.034, 2007.
- Jaffe, D.A., Hafner W., Chand D., Westerling A., and Spracklen D.: Influence of Fires on O₃ Concentrations in the Western U.S., *Environmental Science and Technology*, 42 (16), 5885-5891, doi: 10.1021/es800084k, 2008.
- Kim, Y. P. and Seinfeld, J. H.: Atmospheric Gas–Aerosol Equilibrium: III Thermodynamics of Crustal Elements Ca²⁺, K⁺, and Mg²⁺, *Aerosol Science and Technology*, 22(1), 93-110, 1995.
- Koch, D., Bond, T. C., Streets, D., Unger, N., and van der Werf, G. R.: Global impacts of aerosols from particular source regions and sectors, *Journal of Geophysical Research*, 112, D02205, doi: 10.1029/2005JD007024, 2007.

- Koch, D., Schulz, M., Kinne, S., McNaughton, C., Spackman, J. R., Balkanski, Y., Bauer, S., Bernsten, T., Bond, T. C., Boucher, O., Chin, M., Clarke, A., De Luca, N., Dentener, F., Diehl, T., Dubovik, O., Easter, R., Fahey, D. W., Feichter, J., Fillmore, D., Freitag, S., Ghan, S., Ginoux, P., Gong, S., Horowitz, L., Iversen, T., Kirkevåg, A., Klimont, Z., Kondo, Y., Krol, M., Liu, X., Miller, R., Montanaro, V., Moteki, N., Myhre, G., Penner, J. E., Perlwitz, J., Pitari, G., Reddy, S., Sahu, L., Sakamoto, H., Schuster, G., Schwarz, J. P., Seland, Ø., Stier, P., Takegawa, N., Takemura, T., Textor, C., van Aardenne, J. A., and Zhao, Y.: Evaluation of black carbon estimations in global aerosol models, *Atmospheric Chemistry and Physics*, 9, 9001-9026, doi: 10.5194/acp-9-9001-2009, 2009.
- Kopacz, M., Mauzerall, D. L., Wang, J., Leibensperger, E. M., Henze, D. K., and Singh, K.: Origin and radiative forcing of black carbon transported to the Himalayas and Tibetan Plateau, *Atmospheric Chemistry and Physics*, 11, 2837-2852, doi: 10.5194/acp-11-2837-2011, 2011.
- Koumoutsaris, S. and Bey, I.: Can a global model reproduce observed trends in summertime surface ozone levels?, *Atmospheric Chemistry and Physics Discussions*, 12, 2025-2056, doi:10.5194/acpd-12-2025-2012, 2012.
- Kroon, M., de Haan, J. F., Veefkind, J. P., Froidevaux, L., Wang, R., Kivi, R., and Hakkarainen, J. J.: Validation of operational ozone profiles from the Ozone Monitoring Instrument, *Journal of Geophysical Research*, 116, D18305, doi: 10.1029/2010JD015100, 2011.
- Langford, A. O., Brioude, J., Cooper, O.R., Senff, C.J., Alvarez II, R.J., Hardesty, R.M., Johnson, B.J., and Oltmans, S.J.: Stratospheric influence on surface ozone in the Los Angeles area during late spring and early summer of 2010, *Journal of Geophysical Research*, 117, D00V06, doi: 10.1029/2011JD016766, 2011.
- Lathièrre, J., Hauglustaine, D. A., Friend, A. D., De Noblet-Ducoudré, N., Viovy, N., and Folberth, G. A.: Impact of climate variability and land use changes on global biogenic volatile organic compound emissions, *Atmospheric Chemistry and Physics*, 6, 2129-2146, doi: 10.5194/acp-6-2129-2006, 2006.
- Levy, H., II, Schwarzkopf, M. D., Horowitz, L., Ramaswamy, V., and K. L. Findell: Strong sensitivity of late 21st century climate to projected changes in short-lived air pollutants, *Journal of Geophysical Research*, 113, D06102, doi: 10.1029/2007JD009176, 2008.
- Li, Q. B., Jacob, D. J., Bey, I., Palmer, P. I., Duncan, B. N., Field, B. D., Martin, R. V., Fiore, A. M., Yantosca, R. M., Parrish, D. D., Simmonds, P. G., and Oltmans, S. J.: Transatlantic transport of pollution and its effects on surface ozone in Europe and North America, *Journal of Geophysical Research*, 107(D13), 4166, doi: 10.1029/2001JD001422, 2002.

- Lin, M., Holloway, T., Carmichael, G. R., and Fiore, A. M.: Quantifying pollution inflow and outflow over East Asia in spring with regional and global models, *Atmospheric Chemistry and Physics*, 10, 4221-4239, doi: 10.5194/acp-10-4221-2010, 2010.
- Lin, M., A. M. Fiore, L. W. Horowitz, O. R. Cooper, V. Naik, J. Holloway, B. J. Johnson, A. Middlebrook, S. J. Oltmans, I. B. Pollack, T. B. Ryerson, J. X. Warner, C. Wiedinmyer, J. Wilson, B. Wyman: Transport of Asian ozone pollution into surface air over the western United States in spring, *Journal of Geophysical Research*, 117, D00V07, doi: 10.1029/2011JD016961, 2012.
- Liu, G., Tarasick, D. W., Fioletov, V. E., Sioris, C. E., and Rochon, Y. J.: Ozone correlation lengths and measurement uncertainties from analysis of historical ozonesonde data in North America and Europe, *Journal of Geophysical Research*, 114, D04112, doi: 10.1029/2008JD010576, 2009.
- Lu, Z., Zhang, Q., and Streets, D. G.: Sulfur dioxide and primary carbonaceous aerosol emissions in China and India, 1996–2010, *Atmospheric Chemistry and Physics*, 11, 9839-9864, doi: 10.5194/acp-11-9839-2011, 2011.
- Madronich, S., Flocke, S., Zeng, J., Petropavlovskikh, I., and Lee-Taylor, J.: The Tropospheric Ultra-violet Visible (TUV) model Manual, <http://www.acd.ucar.edu/>, 2002.
- Mauzerall, D. L. and Wang, X.: Protecting Agricultural Crops from the Effects of Tropospheric Ozone Exposure: Reconciling Science and Standard Setting in the United States, Europe and Asia, *Annual Review of Energy and the Environment*, 26, 237-268, 2001.
- McCarthy, J. E.: Ozone Air Quality Standards: EPA's Proposed January 2010 Revision, <http://www.fas.org/sgp/crs/misc/R41062.pdf>, 2010.
- McKeen, S., Grell, G., Peckham, S., Wilczak, J., Djalalova, I., Hsie, E.-Y., Frost, G., Peischl, J., Schwarz, J., Spackman, R., Holloway, J., de Gouw, J., Warneke, C., Gong, W., Bouchet, V., Gaudreault, S., Racine, J., McHenry, J., McQueen, J., Lee, P., Tang, Y., Carmichael, G. R., and Mathur, R.: An evaluation of real-time air quality forecasts and their urban emissions over eastern Texas during the summer of 2006 Second Texas Air Quality Study field study, *Journal of Geophysical Research*, 114, D00F11, doi: 10.1029/2008JD011697, 2009.
- Mena-Carrasco, M., Tang, Y., Carmichael, G.R., Chai, T., Thongbongchoo, N., Campbell, J.E., Kulkarni, S., Horowitz, L., Vukovich, J., Avery, M., Brune, W., Dibb, J.E., Emmons, L., Flocke, F., Sachse, G.W., Tan, D., Shetter, R., Talbot, R.W., Streets, D.G., Frost, G. J., and Blake, D.: Improving regional ozone modeling through systematic evaluation of errors using the aircraft observations during the International Consortium for Atmospheric Research on Transport and Transformation, *Journal of Geophysical Research*, 112, D12S19, doi: 10.1029/2006JD007762, 2007.

- Mesinger, F., DiMego, G., Kalnay, E., Mitchell, K., Shafran, P. C., Ebisuzaki, W., Jovic, D., Woollen, J., Rogers, E., Berbery, E. H., Ek, M. B., Fan, Y., Grumbine, R., Higgins, W., Li, H., Lin, Y., Manikin, G., Parrish, D. and Shi, W.: North American Regional Reanalysis, *Bulletin of the American Meteorological Society*, 87(3), 343–360, doi: 10.1175/BAMS-87-3-343, 2006.
- MODIS cloud fraction data (MOD06L2): <http://ladsweb.nascom.nasa.gov/data/search.html>, accessed in December, 2011.
- Moody, J. L., Felker, S. R., Wimmers, A. J., Osterman, G., Bowman, K., Thompson, A. M., and Tarasick, D. W.: A Multi-sensor Upper Tropospheric Ozone Product (MUTOP) based on TES ozone and GOES water vapor: validation with ozonesondes, *Atmospheric Chemistry and Physics Discussion*, 11, 30487-30526, doi: 10.5194/acpd-11-30487-2011, 2011.
- Murphy, D. M., Chow, J. C., Leibensperger, E. M., Malm, W. C., Pitchford, M., Schichtel, B. A., Watson, J. G., and White, W. H.: Decreases in elemental carbon and fine particle mass in the United States, *Atmospheric Chemistry and Physics*, 11, 4679-4686, doi: 10.5194/acp-11-4679-2011, 2011.
- Naik, V., Mauzerall, D. L., Horowitz, L. W., Schwarzkopf, M. D., Ramaswamy, V., and Oppenheimer, M.: On the sensitivity of radiative forcing from biomass burning aerosols and ozone to emission location, *Geophysical Research Letter*, 34, L03818, doi: 10.1029/2006GL028149, 2007.
- National Research Council (NRC), global sources of local pollution-An Assessment of Long-Range Transport of Key Air Pollutants to and from the United States, 35 - 66, http://books.nap.edu/openbook.php?record_id=12743&page=35, 2009.
- Nassar, R., Logan, J. A., Worden, H. M., Megretskaia, I. A., Bowman, K. W., Osterman, G. B., Thompson, A. M., Tarasick, D. W., Austin, S., Claude, H., Dubey, M. K., Hocking, W. K., Johnson, B. J., Joseph, E., Merrill, J., Morris, G., Newchurch, M., Oltmans, S.J., Posny, F., Schmidlin, F. J., Vömel, H., Whiteman, D.N., Witte, J. C.: Validation of Tropospheric Emission Spectrometer (TES) Nadir Ozone Profiles Using Ozonesonde Measurements, *Journal of Geophysical Research*, 113, D15S17, doi: 10.1029/2007JD008819, 2008.
- Newman, S., Jeong, S., Fischer, M. L., Xu, X., Haman, C. L., Lefer, B., Alvarez, S., Rappenglueck, B., Kort, E. A., Andrews, A. E., Peischl, J., Gurney, K. R., Miller, C. E., and Yung, Y. L.: Diurnal tracking of anthropogenic CO₂ emissions in the Los Angeles basin megacity during spring, 2010, *Atmospheric Chemistry and Physics Discussion*, 12, 5771-5801, doi:10.5194/acpd-12-5771-2012, 2012.
- Oltmans, S. J., Lefohn, A. S., Harris, J. M., and Shadwick, D. S.: Background ozone levels of air entering the west coast of the U.S. and assessment of longer-term changes, *Atmospheric Environment*, 42, 6020-6038, doi: 10.1016/j.atmosenv.2008.03.034, 2008.

- Pan, L., Chai, T., Carmichael, G., Tang, Y., Streets, D., Woo, J., Friedli, H.R., and Radke, L.F.: Top-down estimate of mercury emissions in china using four-dimensional variational data assimilation, *Atmospheric Environment*, 41 (13), 2804–2819, doi: 10.1016/j.atmosenv.2006.11.048, 2007.
- Park, R. J., Jacob, D. J., Chin, M., and Martin, R. V.: Sources of carbonaceous aerosols over the United States and implications for natural visibility, *Journal of Geophysical Research*, 108 (D12), 4355, doi: 10.1029/2002JD003190, 2003.
- Parrington, M., Jones, D. B. A., Bowman, K. W., Thompson, A. M., Tarasick, D. W., Merrill, J., Oltmans, S. J., Leblanc, T., Witte, J. C., and Millet, D. B.: Impact of the assimilation of ozone from the Tropospheric Emission Spectrometer on surface ozone across North America, *Geophysical Research Letters*, 36, L04802, doi:10.1029/2008GL036935, 2009.
- Parrish, D. D., Holloway, J. S., Trainer, M., Murphy, P. C., Forbes, G. L., and Fehsenfeld, F. C.: Export of North American Ozone Pollution to the North Atlantic Ocean, *Science*, 259, 1436–1439, doi: 10.1126/science.259.5100.1436, 1993.
- Parrish, D. D., Trainer, M., Holloway, J. S., Yee, J. E., Warshawsky, M. S., and Fehsenfeld, F. C.: Relationships between ozone and carbon monoxide at surface sites in the North Atlantic region, *Journal of Geophysical Research*, 103(D11), 13357–13376, doi:10.1029/98JD00376, 1998.
- Parrish, D. D., Millet, D. B., and Goldstein, A. H.: Increasing ozone in marine boundary layer inflow at the west coasts of North America and Europe, *Atmospheric Chemistry and Physics*, 9, 1303-1323, doi: 10.5194/acp-9-1303-2009, 2009.
- Parrish, D. D., Aikin, K. C., Oltmans, S. J., Johnson, B. J., Ives, M., and Sweeny, C.: Impact of transported background ozone inflow on summertime air quality in a California ozone exceedance area, *Atmospheric Chemistry and Physics*, 10, 10093-10109, doi: 10.5194/acp-10-10093-2010, 2010.
- Pfister, G., Thompson, A.M., Emmons, L.K., Hess, P.G., Lamarque, J.-F., and Yorks, Y.E.: Analysis of the Summer 2004 Ozone Budget over the U.S. using IONS observations and MOZART-4 simulations, *Journal of Geophysical Research*, 113, D23306, doi: 10.1029/2008JD010190, 2008.
- Pfister, G. G., Parrish, D. D., Worden, H., Emmons, L. K., Edwards, D. P., Wiedinmyer, C., Diskin, G. S., Huey, G., Oltmans, S. J., Thouret, V., Weinheimer, A., and Wisthaler, A.: Characterizing summertime chemical boundary conditions for airmasses entering the US West Coast, *Atmospheric Chemistry and Physics*, 11, 1769-1790, doi:10.5194/acp-11-1769-2011, 2011a.
- Pfister, G. G., Avise, J., Wiedinmyer, C., Edwards, D. P., Emmons, L. K., Diskin, G. D., Podolske, J., and Wisthaler, A.: CO source contribution analysis for California during ARCTAS-CARB, *Atmospheric Chemistry and Physics*, 11, 7515-7532, doi:10.5194/acp-11-7515-2011, 2011b.

- Pierce, R. B., Schaack, T., Al-Saadi, J. A., Fairlie, T. D., Kittaka, C., Lingenfelter, G., Natarajan, M., Olson, J., Soja, A., Zapotocny, T., Lenzen, A., Stobie, J., Johnson, D., Avery, M. A., Sachse, G. W., Thompson, A., Cohen, R., Dibb, J. E., Crawford, J., Rault, D., Martin, R., Szykman, J., and Fishman, J.: Chemical data assimilation estimates of continental U.S. ozone and nitrogen budgets during the Intercontinental Chemical Transport Experiment–North America, *Journal of Geophysical Research*, 112, D12S21, doi: 10.1029/2006JD007722, 2007.
- Platnick, S., King, M.D., Ackerman, S.A., Menzel, W.P., Baum, B.A., Riedi, J.C., Frey, R.A.: The MODIS cloud products: algorithms and examples from Terra, *IEEE Transactions on Geoscience and Remote Sensing*, 41(2), 459- 473, doi: 10.1109/TGRS.2002.808301, 2003.
- Pommier, M., Clerbaux, C., Law, K. S., Ancellet, G., Bernath, P., Coheur, P.-F., Hadji-Lazaro, J., Hurtmans, D., Nédélec, P., Paris, J.-D., Ravetta, F., Ryerson, T. B., Schlager, H., and Weinheimer, A. J.: Analysis of IASI tropospheric O₃ data over Arctic during POLARCAT campaigns in 2008, *Atmospheric Chemistry and Physics Discussion*, 11, 33127-33171, doi: 10.5194/acpd-11-33127-2011, 2011.
- Ramana, M., Ramanathan, V., Feng, Y., Yoon, S.-C., Kim, S.-W., Carmichael, G. R., and Schauer, J. J.: Warming influenced by black carbon to sulfate ratio and black carbon source, *Nature Geoscience*, 3(8), 542-545, doi: 10.1038/ngeo918, 2010.
- Ramanathan, V. and Feng, Y.: On avoiding dangerous anthropogenic interference with the climate system: formidable challenges, *Proceedings of the National Academy of Sciences*, 105, 14245–14250, doi: 10.1073/pnas.0803838105, 2008.
- Richards, N. A. D., Osterman, G. B., Browell, E. V., Hair, J. W., Avery, M., and Li, Q.: Validation of Tropospheric Emission Spectrometer ozone profiles with aircraft observations during the Intercontinental Chemical Transport Experiment–B, *Journal of Geophysical Research*, 113, D16S29, doi: 10.1029/2007JD008815, 2008.
- Rodgers, C. D., *Inverse Methods for Atmospheric Sounding: Theory and Practise*, World Scientific, 2000.
- Russell, A. R., Perring, A. E., Valin, L. C., Bucsela, E. J., Browne, E. C., Wooldridge, P. J., and Cohen, R. C.: A high spatial resolution retrieval of NO₂ column densities from OMI: method and evaluation, *Atmospheric Chemistry and Physics*, 11, 8543-8554, doi:10.5194/acp-11-8543-2011, 2011.
- Saide, P. E., Carmichael, G. R., Spak, S. N., Gallardo, L., Osses, A. E., Mena-Carrasco, M. A., and Pagowski, M.: Forecasting urban PM₁₀ and PM_{2.5} pollution episodes in very stable nocturnal conditions and complex terrain using WRF-Chem CO tracer model, *Atmospheric Environment*, 45(16), 2769-2780, doi:10.1016/j.atmosenv.2011.02.001, 2011.

- Sandu, A., Daescu, D. N., Carmichael, G. R., and Chai, T.: Adjoint sensitivity analysis of regional air quality models, *Journal of Computational Physics*, 204(1):222-252, 2005.
- Sandu, A., and Chai, T.F.: Chemical Data Assimilation an Overview, *Atmosphere*, 2(3), 426-463, doi: 10.3390/atmos2030426, 2011.
- Schuster, G. L., Dubovik, O., Holben, B. N., and Clothiaux, E. E.: Inferring black carbon content and specific absorption from Aerosol Robotic Network (AERONET) aerosol retrievals, *Journal of Geophysical Research*, 110, D10S17, doi: 10.1029/2004JD004548, 2005.
- Shiraiwa, M., Kondo, Y., Moteki, N., Takegawa, N., Miyazaki, Y., and Blake, D. R.: Evolution of mixing state of black carbon in polluted air from Tokyo, *Geophysical Research Letters*, 34, L16803, doi:10.1029/2007GL029819, 2007.
- Shindell, D. T., Faluvegi, G., Stevenson, D. S., Krol, M. C., Emmons, L. K., Lamarque, J.-F., Petron, G., Dentener, F. J., Ellingsen, K., Schultz, M. G., Wild, O., Amann, M., Atherton, C. S., Bergmann, D. J., Bey, I., Butler, T., Cofala, J., Collins, W. J., Derwent, R. G., Doherty, R. M., Drevet, J., Eskes, H. J., Fiore, A. M., Gauss, M., Hauglustaine, D. A., Horowitz, L. W., Isaksen, I. S. A., Lawrence, M. G., Montanaro, V., Mueller, J.-F., Pitari, G., Prather, M. J., Pyle, J. A., Rast, S., Rodriguez, J. M., Sanderson, M. G., Savage, N. H., Strahan, S. E., Sudo, K., Szopa, S., Unger, N., van Noije, T. P. C., Zeng, G.: Multimodel simulations of carbon monoxide: Comparison with observations and projected near-future changes, *Journal of Geophysical Research*, 111, D19306, doi: 10.1029/2006JD007100, 2006.
- Shindell, D., Lamarque, J.-F., Unger, N., Koch, D., Faluvegi, G., Bauer, S., Ammann, M., Cofala, J., and Teich, H.: Climate forcing and air quality change due to regional emissions reductions by economic sector, *Atmospheric Chemistry and Physics*, 8, 7101-7113, doi: 10.5194/acp-8-7101-2008, 2008.
- Singh, K., Sandu, A., Bowman, K. W., Parrington, M., Jones, D. B. A., and Lee, M.: Ozone data assimilation with GEOS-Chem: a comparison between 3-D-Var, 4-D-Var, and suboptimal Kalman filter approaches, *Atmospheric Chemistry and Physics Discussion*, 11, 22247-22300, doi: 10.5194/acpd-11-22247-2011, 2011.
- Singh, H.B., Cai, C., Kaduwela, A., Weinheimer, A., and Wisthaler, A.: Interactions of fire emissions and urban pollution over California: Ozone formation and air quality simulations, *Atmospheric Environment*, doi: 10.1016/j.atmosenv.2012.03.046, 2012.
- Skamarock, W. C., Klemp, J. B., Dudhia, J., Gill, D., Barker, D., M., Wang, W., and Powers, J. G.: A Description of the Advanced Research WRF Version 2, available online at: www.mmm.ucar.edu/wrf/users/docs/arw_v2.pdf, 2007.
- Skamarock, W. C., Klemp, J. B., Dudhia, J., Gill, D., Barker, D., M., Wang, W., and Powers, J. G.: A Description of the Advanced Research WRF Version 3, available online at: www.mmm.ucar.edu/wrf/users/docs/arw_v3.pdf, 2008.

- Smith, K. R., Jerrett, M., and Anderson, H. R. *et al.*: Public health benefits of strategies to reduce greenhouse-gas emissions: health implications of short-lived greenhouse pollutants, *Lancet*, doi: 10.1016/S0140-6736(09)61716-5, 2009.
- Stevenson, D. S., Dentener, F. J., Schultz, M. G., Ellingsen, K., Van Noije, T. P. C., Wild, O., Zeng, G., Amann, M., Atherton, C. S., Bell, N., Bergmann, D. J., Bey, I., Butler, T., Cofala, J., Collins, W. J., Derwent, R. G., Doherty, R. M., Drevet, J., Eskes, H. J., Fiore, A., Gauss, M. A., Hauglustaine, D. A., Horowitz, L. W., Isaksen, I. S. A., Krol, M. C., Lamarque, J. F., Lawrence, M. G., Montanero, V., Müller, J. F., Pitari, G., Prather, M. J., Pyle, J. A., Rast, S., Rodriguez, J. M., Sanderson, M. G., Savage, N. H., Shindell, D. T., Strahan, S. E., Sudo, K., and Szopa, S., Multi-model ensemble simulations of present-day and near-future tropospheric ozone, *Journal of Geophysical Research*, 111, D08301, doi: 10.1029/2005JD006338, 2006.
- Stith, J.L., Ramanathan, V., Cooper, W.A., Roberts, G.C., DeMott, P.J., Carmichael, G.R., Hatch, C.D., Adhikary, B., Twohy, C.H., Rogers, D.C., Baumgardner, D., Prenni, A.J., Campos, T., Gao, R., Anderson, J., and Feng, Y.: An overview of aircraft observations from the Pacific dust experiment campaign, *Journal of Geophysical Research*, 114, D05207, doi: 10.1029/2008JD010924, 2009.
- Tang, Y.H., Carmichael, G.R., Woo, J.H., Thongboonchoo, N., Kurata, G., Uno, I., Streets, D.G., Blake, D.R., Weber, R.J., Talbot, R.W., Kondo, Y., Singh, H.B., and Wang, T.: Influences of biomass burning during the Transport and Chemical Evolution Over the Pacific (TRACE-P) experiment identified by the regional chemical transport model, *Journal of Geophysical Research*, 108 (D21), 8824, doi: 10.1029/2002JD003110, 2003.
- Tang, Y., Carmichael, G., Horowitz, L., Uno, I., Woo, J.-H., Streets, D., Dabdub, D., Kurata, G., Sandu, A., Allan, J., Atlas, E., Flocke, F., Huey, L., Jakoubek, R., Millet, D., Quinn, P., Roberts, J., Worsnop, D., Goldstein, A., Donnelly, S., Schauffler, S., Stroud, V., Johnson, K., Avery, M., Singh, H., Apel, E.: Multiscale simulations of tropospheric chemistry in the eastern Pacific and on the U.S. West Coast during spring 2002, *Journal of Geophysical Research*, 109, D23S11, doi: 10.1029/2004JD004513, 2004.
- Tang, Y.H. , Carmichael, G.R., Thongboonchoo, N., Chai, T.F., Horowitz, L.W., Pierce, R.B., Al-Saadi, J.A., Pfister, G., Vukovich, J.M., Avery, M.A., Sachse, G.W., Ryerson, T.B., Holloway, J.S., Atlas, E.L., Flocke, F.M., Weber, R.J., Huey, L.G., Dibb, J.E., Streets, D.G. and Brune, W. H.: Influence of lateral and top boundary conditions on regional air quality prediction: a multiscale study coupling regional and global chemical transport models, *Journal of Geophysical Research*, 112 (D10), D10S18, doi: 10.1029/2006JD007515, 2007.
- Task Force on Hemispheric Transport of Air Pollution (TF HTAP), 2010 Final Assessment report, Part A: Ozone and particulate matter, http://www.htap.org/activities/2010_Final_Report/HTAP%202010%20Part%20A%20110407.pdf, 2010.

TES L2 data user's guide, Version 5.0:

http://eosweb.larc.nasa.gov/PRODOCS/tes/UsersGuide/TES_L2_Data_Users_Guide.pdf, 2011.

Textor, C., Schulz, M., Guibert, S., Kinne, S., Balkanski, Y., Bauer, S., Bernsten, T., Berglen, T., Boucher, O., Chin, M., Dentener, F., Diehl, T., Easter, R., Feichter, H., Fillmore, D., Ghan, S., Ginoux, P., Gong, S., Grini, A., Hendricks, J., Horowitz, L., Huang, P., Isaksen, I., Iversen, I., Kloster, S., Koch, D., Kirkevåg, A., Kristjansson, J. E., Krol, M., Lauer, A., Lamarque, J. F., Liu, X., Montanaro, V., Myhre, G., Penner, J., Pitari, G., Reddy, S., Seland, Ø., Stier, P., Takemura, T., and Tie, X.: Analysis and quantification of the diversities of aerosol life cycles within AeroCom, *Atmospheric Chemistry and Physics*, 6, 1777-1813, doi: 10.5194/acp-6-1777-2006, 2006.

The White House Office of the Press Secretary: Statement by the President on the Ozone 1190 National Ambient Air Quality Standards, <http://www.whitehouse.gov/the-press-office/2011/09/02/statement-president-ozone-national-ambient-air-quality-standards>, Sep. 2, 2011.

Thompson, A. M., Oltmans, S. J., Tarasick, D. W., von der Gathen, P., Smit, H. G., and Witte, J. C.: Strategic ozone sounding networks: Review of design and accomplishments, *Atmospheric Environment*, 45(13), 2145–2163, doi: 10.1016/j.atmosenv.2010.05.002, 2011.

Thornhill, K. L., Chen, G., Dibb, J., Jordan, C. E., Omar, A., Winstead, E. L., Schuster, G., Clarke, A., McNaughton, C., Scheuer, E., Blake, D., Sachse, G., Huey, L. G., Singh, H. B., and Anderson, B. E.: The impact of local sources and long-range transport on aerosol properties over the northeast US region during INTEX-NA, *Journal of Geophysical Research*, 113, D08201, doi:10.1029/2007JD008666, 2008.

VanCuren, R. A.: Asian aerosols in North America: Extracting the chemical composition and mass concentration of the Asian continental aerosol plume from long-term aerosol records in the western United States, *Journal of Geophysical Research*, 108 (D20), 4623, doi: 10.1029/2003JD003459, 2003.

Veefkind, J.P., Validation Status of the OMI Ozone Profile Product OMO3PR, Issue 1.5, June 2009.

VIEWS 2.0 data wizard (for downloading aerosol at IMPROVE and urban sites):

<http://views.cira.colostate.edu/web/DataWizard/>, accessed in March 2011.

Voulgarakis, A., Telford, P. J., Aghedo, A. M., Braesicke, P., Faluvegi, G., Abraham, N. L., Bowman, K. W., Pyle, J. A., and Shindell, D. T.: Global multi-year O₃-CO correlation patterns from models and TES satellite observations, *Atmospheric Chemistry and Physics*, 11, 5819-5838, doi: 10.5194/acp-11-5819-2011, 2011.

UNEP and WMO: Integrated Assessment of Black Carbon and Tropospheric Ozone: Summary for Decision Makers, http://www.unep.org/dewa/Portals/67/pdf/Black_Carbon.pdf, 2011.

- Unger, N., Bond, T. C., Wang, J. S., Koch, D. M., Menon, S., Shindell, D. T., and Bauer, S.: Attribution of climate forcing to economic sectors, *Proceedings of the National Academy of Sciences*, 107, 3382–3387, doi: 10.1073/pnas.0906548107, 2009.
- US Environmental Protection Agency (US EPA): Fact Sheet: Proposal to revise the national ambient air quality standards for ozone, <http://www.epa.gov/air/ozonepollution/pdfs/fs20100106std.pdf>, 2010
- US EPA: Report to congress on black carbon, [http://yosemite.epa.gov/sab/sabproduct.nsf/fedrgstr_activites/05011472499C2FB28525774A0074DADE/\\$File/BC+RTC+External+Peer+Review+Draft-opt.pdf](http://yosemite.epa.gov/sab/sabproduct.nsf/fedrgstr_activites/05011472499C2FB28525774A0074DADE/$File/BC+RTC+External+Peer+Review+Draft-opt.pdf), 2011.
- Walker, T. W., Martin, R. V., van Donkelaar, A., Leaitch, W. R., MacDonald, A. M., Anlauf, K. G., Cohen, R. C., Bertram, T. H., Huey, L. G., Avery, M. A., Weinheimer, A. J., Flocke, F. M., Tarasick, D. W., Thompson, A. M., Streets, D. G., and Liu, X.: Trans-Pacific transport of reactive nitrogen and ozone to Canada during spring, *Atmospheric Chemistry and Physics*, 10, 8353-8372, doi:10.5194/acp-10-8353-2010, 2010.
- Wang, L., Newchurch, M.J., Biazar, A., Liu, X., Kuang, S., Khan, M., Chance, K.: Evaluating AURA/OMI ozone profiles using ozonesonde data and EPA surface measurements for August 2006, *Atmospheric Environment*, 45(2011), 5523-5530, doi: 10.1016/j.atmosenv.2011.06.012, 2011.
- Weiss-Penzias, P., Jaffe, D. A., Swartzendruber, P., Hafner, W., Chand, D., and Prestbo, E.: Quantifying Asian biomass burning sources of mercury using the Hg/CO ratio in pollution plumes observed at the Mount Bachelor Observatory, *Atmospheric Environment*, 41(21), 4366-4379, doi: 10.1016/j.atmosenv.2007.01.058, 2007.
- Wigder, N. L., and Jaffe, D. A.: Influence of Daily Variations in Baseline Ozone on Urban Air Quality in the United States Pacific Northwest, submitted to *Journal of Geophysical Research*, 2012.
- Wild, O., and Prather, M.J.: Global tropospheric ozone modelling: Quantifying errors due to grid resolution, *Journal of Geophysical Research*, 111 (D11), D11305, doi: 10.1029/2005JD006605, 2006.
- Wild, O., Fiore, A. M., Shindell, D. T., Doherty, R. M., Collins, W. J., Dentener, F. J., Schultz, M. G., Gong, S., MacKenzie, I. A., Zeng, G., Hess, P., Duncan, B. N., Bergmann, D. J., Szopa, S., Jonson, J. E., Keating, T. J., and Zuber, A.: Modelling future changes in surface ozone: a parameterized approach, *Atmospheric Chemistry and Physics*, 12, 2037-2054, doi:10.5194/acp-12-2037-2012, 2012.
- Wisthaler, A., Hansel, A., Dickerson, R. R., and Crutzen, P. J.: Organic trace gas measurements by PTR-MS during INDOEX 1999, *Journal of Geophysical Research*, 107(D19), 8024, doi: 10.1029/2001JD000576, 2002.

- Worden, J., Liu, X., Bowman, K., Chance, K., Beer, R., Eldering, A., Gunson, M., and Worden, H.: Improved tropospheric ozone profile retrievals using OMI and TES radiances, *Geophysical Research Letters*, 34, L01809, doi: 10.1029/2006GL027806, 2007.
- Wu, L., Mallet, V., Bocquet, M., and Sportisse, B.: A comparison study of data assimilation algorithms for ozone forecasts, *Journal of Geophysical Research*, 113, D20310, doi: 10.1029/2008JD009991, 2008.
- Zhang, L., Jacob, D. J., Bowman, K. W., Logan, J. A., Turquety, S., Hudman, R. C., Li, Q., Beer, R., Worden, H. M., Rinsland, C. P., Kulawik, S. S., Lampel, M. C., Shephard, M. W., Fisher, B. M., Eldering, A., and Avery, M. A.: Ozone-CO correlations determined by the TES satellite instrument in continental outflow regions, *Geophysical Research Letters*, 33, L18804, doi: 10.1029/2006GL026399, 2006.
- Zhang, L., Jacob, D. J., Boersma, K. F., Jaffe, D. A., Olson, J. R., Bowman, K. W., Worden, J. R., Thompson, A. M., Avery, M. A., Cohen, R. C., Dibb, J. E., Flock, F. M., Fuelberg, H. E., Huey, L. G., McMillan, W. W., Singh, H. B., and Weinheimer, A. J.: Transpacific transport of ozone pollution and the effect of recent Asian emission increases on air quality in North America: an integrated analysis using satellite, aircraft, ozonesonde, and surface observations, *Atmospheric Chemistry and Physics*, 8, 6117-6136, doi:10.5194/acp-8-6117-2008, 2008.
- Zhang, L., Jacob, D. J., Kopacz, M., Henze, D. K., Singh, K., and Jaffe, D. A.: Intercontinental source attribution of ozone pollution at western U.S. sites using an adjoint method, *Geophysical Research Letters*, 36, L11810, doi: 10.1029/2009GL037950, 2009.
- Zhang, L., Jacob, D. J., Liu, X., Logan, J. A., Chance, K., Eldering, A., and Bojkov, B. R.: Intercomparison methods for satellite measurements of atmospheric composition: application to tropospheric ozone from TES and OMI, *Atmospheric Chemistry and Physics*, 10, 4725-4739, doi: 10.5194/acp-10-4725-2010, 2010.
- Zhang, L., Jacob, D. J., Downey, N. V., Wood, D. A., D. Blewitt, Carouge, C. C., van Donkelaar, A., Jones, D.B.A., Murray, L. T., Wang, Y.: Improved estimate of the policy-relevant background ozone in the United States using the GEOS-Chem global model with $1/2^{\circ} \times 2/3^{\circ}$ horizontal resolution over North America, *Atmospheric Environment*, 45, 6769-6776, doi: 10.1016/j.atmosenv.2011.07.054, 2011.
- Zhang, Q., Streets, D.G., Carmichael, G.R., He, K.B., Huo, H., Kannari, A., Klimont, Z., Park, I.S., Reddy, S., Fu, J.S., Chen, D., Duan, L., Lei, Y., Wang, L.T., and Yao, Z. L.: Asian Emissions in 2006 for the NASA INTEX-B Mission, *Atmospheric Chemistry and Physics*, 9, 5131-5153, doi: 10.5194/acp-9-5131-2009, 2009.
- Zhu, C., Byrd, R. H., Lu, P., and Nocedal, J.: L-BFGS-B--fortran routines for large scale bound constrained optimization, *ACM Transactions on Mathematical Software*, 23(4), 550-560, doi: 10.1145/279232.279236, 1997.

Zoogman, P., Jacob, D.J., Chance, K., Zhang, L., Le Sager, P., Fiore, A.M., Eldering, A., Liu, X., Natraj, V., and Kulawik, S.S.: Ozone Air Quality Measurement Requirements for a Geostationary Satellite Mission, *Atmospheric Environment*, 45, 7143-7150, doi: 10.1016/j.atmosenv.2011.05.058, 2011.